PIERRE-LUC DALLAIRE-DEMERS

QUANTUM SIMULATION OF SUPERCONDUCTORS ON QUANTUM COMPUTERS

QUANTUM SIMULATION OF SUPERCONDUCTORS ON QUANTUM COMPUTERS

Toward the first applications of quantum processors

Dissertation
zur Erlangung des Grades
des Doktors der Naturwissenschaften
der Naturwissenschaftlich-Technischen Fakultät
der Universität des Saarlandes

von

PIERRE-LUC DALLAIRE-DEMERS

Saarbrücken
2016

M.D.W.D.G.B. DEKAN:
Prof. Dr. Christoph Becher

MITGLIEDER DES PRÜFUNGSAUSSCHUSSES:
Prof. Dr. Frank Wilhelm-Mauch
Univ.-Prof. Dr. Peter G. J. van Dongen (Uni. Mainz)
Prof. Dr. Giovanna Morigi
Dr. Adam Wysocki

TAG DES VERTEIDIGUNG:
7.10.2016

Pierre-Luc Dallaire-Demers: *Quantum simulation of superconductors on quantum computers,* Toward the first applications of quantum processors, © 2016

Computers are physical objects,
and computations are physical processes.
What computers can or cannot compute
is determined by the laws of physics alone [. . .]

— David Deutsch [1]

À Louise-Anne

ABSTRACT

Quantum computers are the ideal platform for quantum simulations. Given enough coherent operations and qubits, such machines can be leveraged to simulate strongly correlated materials, where intricate quantum effects give rise to counter-intuitive macroscopic phenomena such as high-temperature superconductivity. Many phenomena of strongly correlated materials are encapsulated in the Fermi-Hubbard model. In general, no closed-form solution is known for lattices of more than one spatial dimension, but they can be numerically approximated using cluster methods. To model long-range effects such as order parameters, a powerful method to compute the cluster's Green's function consists in finding its self-energy through a variational principle. As is shown in this thesis, this allows the possibility of studying various phase transitions at finite temperature in the Fermi-Hubbard model. However, a classical cluster solver quickly hits an exponential wall in the memory (or computation time) required to store the computation variables. We show theoretically that the cluster solver can be mapped to a subroutine on a quantum computer whose quantum memory usage scales linearly with the number of orbitals in the simulated cluster and the number of measurements scales quadratically. We also provide a gate decomposition of the cluster Hamiltonian and a simple planar architecture for a quantum simulator that can also be used to simulate more general fermionic systems. We briefly analyze the Trotter-Suzuki errors and estimate the scaling properties of the algorithm for more complex applications. A quantum computer with a few tens of qubits could therefore simulate the thermodynamic properties of complex fermionic lattices inaccessible to classical supercomputers.

ZUSAMMENFASSUNG

Quantencomputer bieten die ideale Plattform für Quantensimulationen. Eine ausreichende Anzahl an zur Verfügung stehenden kohärenten Manipulationen und Qubits vorausgesetzt, können solche Maschinen stark korrelierte Materialien simulieren, bei denen komplizierte Quanteneffekte zu unerwarteten makroskopischen Phänomenen wie beispielsweise der Hochtemperatursupraleitung führen. Viele Phänomene aus dem Bereich der stark korrelierten Systeme sind in dem Fermi-Hubbard-Modell enthalten. Zwar sind im Allgemeinen für Gitter mit mehr als einer räumlichen Dimension keine Lösungen in geschlossener Form bekannt, jedoch können diese mithilfe von Clustermethoden numerischen approximiert werden. Bei der Modellierung von langreichweitigen Effekten, wie beispielsweise der Ordnungsparameter, besteht eine sehr leistungsfähige Methode zur Berechnung der Greensfunktion des Clusters darin, die Selbstenergie mittels eines Variationsprinzips zu finden. Wie in dieser Arbeit gezeigt wird, ermöglicht dies die Untersuchung zahlreicher Phasenübergänge im Fermi-Hubbard-Modell bei endlichen Temperaturen. Klassische Lösungsverfahren kommen jedoch aufgrund des mit der Clustergröße exponentiell steigenden Bedarfs an Speicher (bzw. der zunehmenden Laufzeit) schnell an ihre Grenzen. Wir zeigen theoretisch, dass das Lösungsverfahren des Clusters auf eine Subroutine eines Quantencomputers abgebildet werden kann, sodass der gebrauchte Speicher linear und die Anzahl an Messungen quadratisch mit der Zahl der Orbitalen im simulierten Cluster skalieren. Zudem geben wir eine Zerlegung des Cluster-Hamiltonoperators in Gatters und eine zugehörige simple, planare Architektur für einen Quantensimulator an, was Anwendung bei der Simulation von gar allgemeineren fermionischen Systemen finden könnte. Für diesen Algorithmus werden die Trotter-Suzuki-Fehler und das Skalierungsverhalten bei komplexeren Anwendungen untersucht. Demnach könnte ein Quantencomputer, ausgestattet mit nur weniger als einem Dutzend Qubits, die thermodynamischen Eigenschaften eines komplexen fermionischen Gitters simulieren, was jedoch für klassische Supercomputer unerreichbar ist.

PUBLICATIONS

Some ideas and figures have appeared previously in the following publications:

[1] Pierre-Luc Dallaire-Demers and Frank K. Wilhelm. "Method to efficiently simulate the thermodynamic properties of the Fermi-Hubbard model on a quantum computer." In: *Phys. Rev. A* 93.3 (Mar. 2016), p. 032303. DOI: `10.1103/physreva.93.032303`.

[2] Pierre-Luc Dallaire-Demers and Frank K. Wilhelm. *Quantum gates and architecture for the quantum simulation of the Fermi-Hubbard model*. 2016. URL: `https://arxiv.org/abs/1606.00208`.

La mer s'avance insensiblement et sans bruit,
rien ne semble se casser rien ne bouge
l'eau est si loin on l'entend à peine…
Pourtant elle finit par entourer la substance rétive,
celle-ci peu à peu devient une presqu'île, puis une île, puis un îlot,
qui finit par être submergé à son tour,
comme s'il s'était finalement dissous dans l'océan
s'étendant à perte de vue…
— Alexandre Grothendieck [2]

ACKNOWLEDGMENTS

I am proud to present this thesis which represents the culmination of my Ph.D in physics at Saarland University. This work would not have been possible without the boundless patience, kindness and mental superpowers of my supervisor Frank Wilhelm-Mauch. I believe his group is the only place gathering all the intellectual resources that were required for the initiation and good pursuit of this research project. I would also like to thank Monika Francois for patiently and efficiently maneuvering me through the university administrative system.

I acknowledge the early support and encouragement of Bruno Taketani, Michael Kaicher and Felix Motzoi from the time in Benasque where simulating infinite lattices on a quantum computer was still a crazy idea and the developments that followed. The thoughtful technical and professional advices of David Sénéchal and David Poulin from Sherbrooke helped validate the first construction of the method and steered the direction of this thesis. I offer a special thanks to Raphael Schmit who swiftly translated the abstract.

My fellow Ph.D companions Daniel Egger, Luke Govia and Per Liebermann inspired me to give my best effort and were the main contributors to making my time in Europe the most memorable.

I thank my parents Marc and Céline and my sisters Claudia and Gabrielle for their lifelong support and love as this is the basis for any accomplishment. I thank my friends at home as well as those I met here and made my time in Saarbrücken so enjoyable.

Louise-Anne, cette thèse t'est dédiée, ton amour et tes encouragements quotidiens furent ma muse pendant ces longs mois d'écriture.

CONTENTS

Preface 1

I THE PHENOMENON OF HIGH TEMPERATURE SUPERCONDUCTIVITY 3

1 SUPERCONDUCTIVITY 5
  1.1 Macroscopic quantum coherence and Cooper pairing . 5
    1.1.1 What is superconductivity? 5
    1.1.2 The Josephson effect 8
    1.1.3 Cooper pairing and macroscopic coherence . . . 9
  1.2 Indistinguishable interacting fermions 12
    1.2.1 Linear response theory and single-particle Green's functions 13
    1.2.2 The microscopic theory of superconductivity . . 17
  1.3 Cuprates and high-temperature superconductivity . . 19

2 THE FERMI-HUBBARD MODEL 25
  2.1 Overview 25
  2.2 The Fermi-Hubbard model 26
    2.2.1 Some known properties 27
  2.3 Solving the Fermi-Hubbard model with the variational cluster approach 31
    2.3.1 The grand canonical potential as a functional of the self-energy 32
    2.3.2 The variational cluster approach 36
  2.4 Example on a square lattice with superconductivity . 38
    2.4.1 Hamiltonian of a cluster 38
    2.4.2 The superlattice of clusters 39
    2.4.3 Calculation of observables 44
    2.4.4 Ozaki summation 46
    2.4.5 Cluster perturbation theory 47
    2.4.6 Potthoff functional at finite temperature 48
  2.5 The method on a classical computer 51

II THE QUANTUM VARIATIONAL CLUSTER APPROACH ON QUANTUM SIMULATORS 55

3 SIMULATING THE FERMI-HUBBARD MODEL ON A QUANTUM COMPUTER 57
  3.1 Overview 57
  3.2 Quantum computing 58
    3.2.1 Fundamentals of quantum computing 58
    3.2.2 Elementary quantum gates 59
    3.2.3 The quantum Fourier transformation 61
    3.2.4 Phase estimation 62

3.2.5 The Jordan-Wigner transformation 63
3.3 Solving the eigenvalue problem on a quantum computer 64
3.3.1 The method on a quantum computer 64
3.3.2 Measuring the correlation function 67
3.4 Conclusion 71
4 QUANTUM GATES AND ARCHITECTURE FOR A QUANTUM SIMULATOR 73
4.1 Overview 73
4.2 A quantum simulator for the Fermi-Hubbard model . 74
4.2.1 The layout of qubits 74
4.3 Time evolution of the cluster Hamiltonian 78
4.3.1 Hamiltonian of a cluster 79
4.3.2 Gate decomposition 81
4.3.3 The Trotter-Suzuki approximation 89
4.4 Scaling to larger clusters 90
4.5 Conclusion 93
Outlook 95

Appendix 97
A NUMERICAL EXAMPLE ON THE 1D CHAIN 99
A.1 Finding the saddle-point of the self-energy functional . 99
A.2 Measuring and calculating the retarded Green's function of the cluster 100
A.3 Simple tight-binding model 102
A.4 Preparation of a Gibbs state 107

BIBLIOGRAPHY 113

LIST OF FIGURES

Figure 1.1 Resistivity of normal metals and superconductors as a function of temperature. 6
Figure 1.2 The Meissner effect corresponds to perfect diamagnetism below the critical temperature. . . 7
Figure 1.3 In the Josephson effect, Cooper pairs tunnel across a junction to form a dissipationless current. 9
Figure 1.4 Contour representing the time ordering of field operators. 14
Figure 1.5 Diagrammatic representation of the Dyson equation. 16
Figure 1.6 Critical temperature of superconducting materials by their year of discovery. 20
Figure 1.7 Atomic structure of cuprates. 21
Figure 1.8 The phase diagram of cuprates. 22
Figure 2.1 The landscape of numerical methods in the study of strongly correlated electrons. 28
Figure 2.2 The anti-ferromagnetic state on a CuO_2 plane. 30
Figure 2.3 The diagrammatic representation of the Luttinger-Ward functional. 33
Figure 2.4 The variational space of self-energy functional theory. 35
Figure 2.5 Cluster decomposition of the lattice. 36
Figure 2.6 The reduced Brillouin zone of the reciprocal lattice. 40
Figure 2.7 Orbital filling factor as a function of the chemical potential in cluster perturbation theory. . . 47
Figure 2.8 Ground state energy of the Fermi-Hubbard model from cluster perturbation theory. 48
Figure 2.9 Spectral density of the Fermi-Hubbard model calculated from cluster perturbation theory. . . 49
Figure 2.10 Simulation of anti-ferromagnetism in the Hubbard model. 50
Figure 2.11 Simulation of d-wave superconductivity in the Hubbard model. 51
Figure 3.1 Decomposition of the quantum Fourier transform. 62
Figure 3.2 Decomposition of the phase estimation protocol. 63
Figure 3.3 Complete quantum algorithm to simulate the correlation functions of a Gibbs state. 65
Figure 3.4 Details of the correlation functions protocol. . 67

Figure 4.1 Practical quantum circuit to measure correlation functions. 76
Figure 4.2 Layout of qubits for a practical quantum simulator. 77
Figure 4.3 Example of the mapping of the orbitals of a cluster to a quantum register. 80
Figure 4.4 Gate decomposition of local terms of the cluster Hamiltonian. 83
Figure 4.5 Gate decomposition of interaction terms of the cluster Hamiltonian. 84
Figure 4.6 Gate decomposition of nearest-neighbor hopping terms of the cluster Hamiltonian. 85
Figure 4.7 Gate decomposition of s-wave pairing terms of the cluster Hamiltonian. 87
Figure 4.8 Gate decomposition of d-wave pairing terms of the cluster Hamiltonian. 88
Figure 4.9 Worst case error from the Trotter-Suzuki decomposition. 91
Figure A.1 Simulation of measured probabilities of the fermion operators for the 2-site 1D chain. 103
Figure A.2 Simulation of the measured correlation function of the fermion operators for the 2-site 1D chain. 103
Figure A.3 Simulated spectral functions for the 2-site 1D chain. 104
Figure A.4 Simulated Potthoff functional for the 2-site 1D chain. 105
Figure A.5 Simulated electronic momentum-frequency distribution for the non-interacting 2-site 1D chain. 106
Figure A.6 Simulated electron momentum distribution for the 2-site 1D chain. 106
Figure A.7 Simulated electronic momentum-frequency distribution for the interacting 2-site 1D chain. . . 107
Figure A.8 Detailed quantum circuit used to approximate a Gibbs state. 108

LIST OF TABLES

Table 2.1 Memory scaling of cluster methods on a classical computer. 52
Table 3.1 Single-qubit gates. 60
Table 3.2 Two-qubit gates. 61

Table 4.1 Commutation relations of different blocks of the cluster Hamiltonian. 90
Table 4.2 Scaling of quantum resources for the simulation of the Fermi-Hubbard model on a quantum computer. 92

ACRONYMS

ARPES	angular-resolved photoemission spectroscopy
BCS	Bardeen-Cooper-Schrieffer
CPT	cluster perturbation theory
CDMFT	cellular dynamical mean-field theory
DCA	dynamical cluster approximation
DIA	dynamical impurity approximation
DMFT	dynamical mean-field theory
FHM	Fermi-Hubbard model
JWT	Jordan-Wigner transformation
QFT	quantum Fourier transform
QMC	quantum Monte Carlo
SFT	self-energy functional theory
VCA	variational cluster approach

PREFACE

This thesis is a report on my research in the field of quantum simulation of materials. Its aim is to lay the foundations for scalable and practical simulations of strongly correlated materials on quantum processors. The principal theme running through all ideas of this research project is macroscopic quantum coherence. Everyday objects can, in principle, exhibit the strange behavior of microscopic quantum particles where state superposition is possible [3] and coincidences are physical [4–6]. For example, at low temperature some materials become superconducting and their body of conducting electrons appears to behave as a single quantum particle. The theory produced in Prof. Frank Wilhelm's group is notably centered around building, understanding and controlling quantum computers and devices made of superconducting materials. In some sense, quantum computers would be the most macroscopically coherent objects as these devices can in principle reproduce all the effects of quantum mechanics. This work is at the intersection of quantum simulations and the study of the phenomenon of superconductivity. This is where the Fermi-Hubbard model appears as a natural object of interest.

The main investigation around the Fermi-Hubbard model was somewhat accidental as I was interested in looking at the physics of mesoscopic superconducting circuits in the limit where the size of the constituent atoms becomes commensurate with the size of the circuit elements. This problem remains completely unsolved, but it lead me to consider the only numerical tools I could possibly use to tackle the problem: the self-energy functional theory of Potthoff and more specifically the variational cluster approach. It quickly became clear that those methods were scaling very similarly to the most general simulations of quantum computers. I had the main ideas of the thesis at the 2015 workshop on quantum simulations in Benasque:

1. *The practical quantity of interest in the simulation of materials is the self-energy of clusters of electrons, not the many-body wave function.*

2. *Self-energy can be evaluated by measuring correlation functions on a quantum computer.*

The results of this thesis derive from these statements. Self-energy functional theory appears as the most natural framework to understand the simulation of correlated materials on a quantum computer. It is, to my knowledge, the first complete and scalable specification for a quantum algorithm to simulate many classes of materials beyond the theoretical capacities of classical computers.

The thesis is divided in two parts with two chapters each. The first part focuses on the classical treatment of superconductivity and the classical simulation of quantum materials. Chapter 1 is an introduction to the phenomenon of superconductivity and the microscopic theory in the context of macroscopic quantum coherence. The microscopic formalism used to describe long-range coherent order is highlighted and the problem of strong correlations is introduced with the example of high-temperature cuprate superconductors. Chapter 2 introduces the details of the Fermi-Hubbard model, the prototypical system studied in the context of strongly correlated materials. Self-energy functional theory and the variational cluster approach are introduced and some numerical results used to benchmark the quantum implementation of the methods are shown. The quantum algorithm is detailed in the second part. Chapter 3 reviews some fundamental concepts of quantum computation. The main heuristic of the hybrid quantum-classical algorithm and the quantum circuit used for the method are explained. Chapter 4 proposes an implementation-independent architecture for a quantum simulators that can run the algorithm. Finally the gate decomposition is used to show the favorable scaling of the quantum method.

Bridging the fields of condensed matter simulations and quantum computing poses some difficulties when one tries to unify the notation and the symbols used across both subjects. I tried to keep the notation consistent with the literature through the thesis but some symbols inevitably appear twice in different contexts. Since the action of electrons is measured in quanta of $\hbar$, they are often taken as being a dimensionless unit 1 without much distinction. Moreover, the Boltzmann constant k_B is also often defined as a dimensionless unit such that energies E, frequencies ω and temperature T are all in units of inverse time τ^{-1}. Long mathematical derivations are avoided as what really matters in this work is the operational relationship between the various physical quantities and concepts involved in the quantum algorithm.

Part I

THE PHENOMENON OF HIGH TEMPERATURE SUPERCONDUCTIVITY

The bottom line for mathematicians is that the architecture has to be right. In all the mathematics that I did, the essential point was to find the right architecture. It's like building a bridge. Once the main lines of the structure are right, then the details miraculously fit. The problem is the overall design.

— Freeman Dyson [7]

1

SUPERCONDUCTIVITY

A central concept unifying the work of this thesis is macroscopic quantum coherence. Namely, the idea that the behavior of some objects large enough to be perceptible by normal human senses could only be described accurately with the rules of quantum theory, a property usually reserved to microscopic objects. The phenomenon of macroscopic quantum coherence is most often manifest in cold systems, where thermal fluctuations are sufficiently suppressed that the microscopic constituents condense into a macroscopic object which behaves like a single quantum particle. The phenomena of Bose-Einstein condensation, superfluidity and superconductivity are examples where a large many-body state has its energy reduced by having all its constituents acting as a single coherent object. A brief introduction to the nature of the superconducting state as a macroscopic quantum coherent phenomenon is given in section 1.1. A short review of essential concepts and results of the microscopic theory of superconductivity follows in section 1.2 as chapters 2 and 3 build on these methods. For practical applications, high-temperature superconductors can be defined as those whose transition temperature is above the boiling point of nitrogen. A technologically important class is the cuprates whose properties are listed in section 1.3.

The development of quantum computers implicitly assumes that macroscopic devices can be built and operated coherently such that the outcome of an algorithm can only be predicted by quantum mechanics. Since superconductors can be layered in microcircuits using standard methods of microfabrication, they can notably be used to build quantum information processing devices. Quantum simulators that can be used to study coherent phenomena in materials are the central theme of the second part of this thesis.

1.1 MACROSCOPIC QUANTUM COHERENCE AND COOPER PAIRING

1.1.1 *What is superconductivity?*

Following the liquefaction of helium in 1908, K. Onnes discovered superconductivity in 1911 [8], 14 years before E. Schrödinger wrote down the wave equation of quantum mechanics. He observed that the resistivity of mercury completely vanishes when a sample is cooled below 4.2°K. Over the years, many metals and alloys were also found to be superconductors at temperatures $< 20°\text{K}$ [9]. This

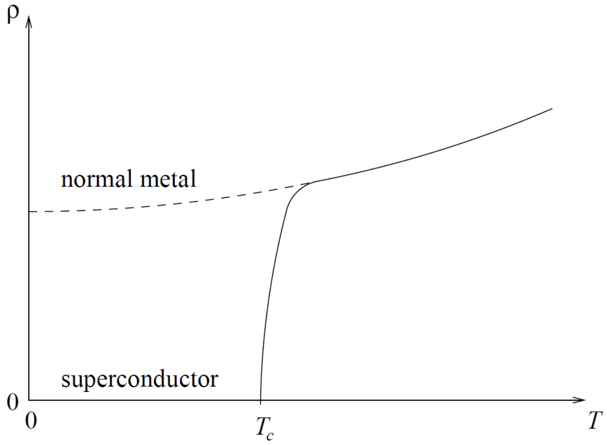

Figure 1.1: Below a critical temperature T_c, the resistivity ρ of superconductors drops to zero. The resistivity of normal metals remains at a finite value at zero temperature because charge carriers scatter inelastically with phonons and crystal defects. The figure has been reproduced from the lectures notes of [10].

is surprising as, even at zero temperature, the electrons in a metal are expected to scatter off impurities, defects and vibrations in the atomic lattice. As can be seen in figure 1.1, energy is dissipated in the collisions and the semiclassical theory of metals predicts a finite resistance proportional to the mean free path of the electrons at low temperature. However in superconducting tin rings, the resistance is zero as far as one can measure since currents have been observed to persist for years.

There is no detectable reconfiguration of the defects and impurities in the crystal structure when measuring x-ray diffraction at the superconducting transition. Neutron scattering also indicates that superconducting metal and alloys have no magnetic moment at the atomic scale. When measuring the specific heat, there is a jump at the critical temperature T_c, which indicates a new thermodynamical state. On average, the energy saved per electron in the superconducting state over the normal state is on the order of $\frac{(k_B T_c)^2}{E_F} \sim 1\text{meV}$, which is small compared to the typical Fermi energy $E_F \sim 1\text{eV}$. This implies that only a fraction of the conducting electrons have their energy changed significantly by the process.

1.1.1.1 *The Meissner effect*

The argument that there are dissipationless currents at thermodynamic equilibrium in superconductors is supported by the presence of a perfect diamagnetic effect for weak magnetic fields (strong fields eventually disfavor superconductivity). In the normal state, metals are typically weak para- or dia- magnets in the presence of an external magnetic field. As shown in figure 1.2, a metal sample cooled

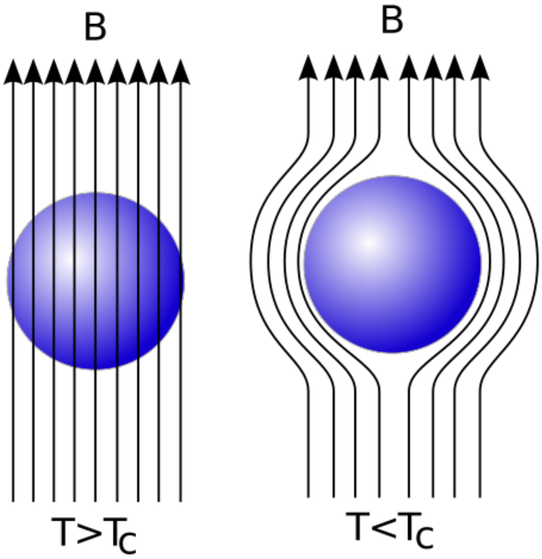

Figure 1.2: When cooled below the transition temperature T_c, supercurrents form on the surface of superconducting samples and completely shield the bulk from and external magnetic field B. This perfect diamagnetism is the Meissner effect. This diagram is reproduced from [13].

below its superconducting transition temperature will completely expel an external magnetic field. This is the Meissner effect [11, 12] which can be explained by the formation of permanent currents on the surface of the superconductor which shields the bulk from the field. The superconducting equilibrium state minimizes the sum of the kinetic and magnetic energies as long as it does not exceed the condensation energy of the electrons [9].

1.1.1.2 *Absence of low-energy excitations*

In normal metals, transport of charge is explained microscopically by the creation of electron-hole pairs with energies close to the Fermi energy E_F. These electron-hole pairs can be described as quasi-particles that can be created with a continuous spectrum of energy from the Fermi sea. This implies that the electronic specific heat of metals is typically linear in temperature and of order $\frac{k_B^2 T}{E_F}$ per electron. Inelastic scattering with crystal defects, impurities and crystal vibrations (phonons) induces energy dissipation and explains the resistive phenomenon in metals. In superconductors, there are no low-energy electron-hole excitations. The existence of an energy gap Δ to create electron-hole pairs is supported by many experimental facts. First, the electronic specific heat is an exponential function of the temperature $\sim e^{-\frac{\Delta}{k_B T}}$, which indicates that the ground state is separated from the first excited states by a gap. In tunnel junctions where a normal metal lead is put in contact with a superconducting material coated with a small layer of insulator, a current will flow across the junction only if the applied voltage $eV \geq \Delta$. Furthermore, electromagnetic radiation in the far infrared and phonons cannot create electron-hole pairs unless $\hbar\omega \geq 2\Delta$ (twice the energy of a single excitation). Finally, the quantity Δ as measured in experiments appears to be related to the transition temperature T_c by the relation

$$2\Delta = 3.5 k_B T_c. \tag{1.1}$$

1.1.1.3 *Overview of the microscopic theory*

In 1957, an effective microscopic theory of superconductivity was formulated by J. Bardeen, L. Cooper and J. Schrieffer [14, 15], the so-called Bardeen-Cooper-Schrieffer (BCS) theory. It explains the superconducting ground state as a condensate of long range "molecules of electrons", or Cooper pairs, that are bound by some attractive interaction. In fact, any gas of electrons with a small attractive interaction forms a condensate of Cooper pairs at low enough temperature. The theory interprets the gap Δ from equation (1.1) as the energy per electron required to break a Cooper pair.

In typical "BCS superconductors"[16], the crystal structure is usually simple. The attractive interaction between electrons near the Fermi level is a consequence of the interaction of the electrons with the crystal lattice through the exchange of virtual phonons. This is known experimentally as the critical temperature, therefore the interaction between the electrons is reduced when a superconductor is made from heavier isotopes. The phonon explanation appears sufficient as there is no other phase transition close to the superconducting transition and the normal state is well described by the Landau Fermi liquid theory of interacting electrons. Under normal conditions of pressure, this interaction mechanism also appears to limit the maximum transition temperature of BCS superconductors to $T_c < 25°\text{K}$. Adding structure to the crystal lattice of BCS superconductors by varying the stoichiometry of the compounds does not have a strong effect on the effective structure of the interaction. In fact, the resulting density of paired electrons N_0 is usually uniform enough that it is used in the description of the state of a superconductor as an isotropic s-wave order parameter. In some sense, this ordering of electrons makes them behave like a macroscopic quantum particle, this description is made more formal in section 1.1.3.

1.1.2 *The Josephson effect*

Long-range "coherent ordering" in superconductors means that the many-body state behaves as a single-particle wave function with an

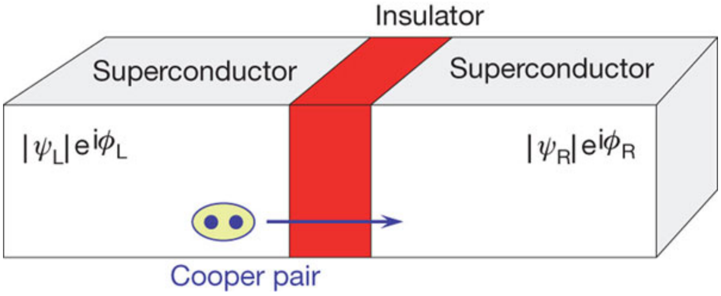

Figure 1.3: A Josephson junction is composed of two superconducting layers separated by a thin insulating layer. If the phase difference of the superconducting order parameters $\phi_L - \phi_R$ is not zero, Cooper pairs can tunnel through the insulating layer and a supercurrent forms across the junction. This diagram has been reproduced from [19].

amplitude $|\Psi|$ (the magnitude of the order parameter) and a phase ϕ. This phase has experimental consequences which are mostly manifest in an effect predicted in 1962 by B. Josephson [17]. As shown in figure 1.3, the Josephson effect corresponds to the formation of a permanent current in a junction composed of two superconducting leads and a thin insulating layer through which Cooper pairs can tunnel. The current $I(\tau)$ across the tunnel junction is given by

$$I(\tau) = I_c \sin(\phi(\tau)), \tag{1.2}$$

where I_c is the critical current of the junction which depends on fabrication and operation parameters and $\phi(\tau) = \phi_L(\tau) - \phi_R(\tau)$ is the phase difference of the macroscopic wave function across the two leads. A voltage difference $V(\tau)$ across the junction induces a time dependent change in the phase difference such that

$$V(\tau) = \frac{\Phi_0}{2\pi}\frac{\partial}{\partial\tau}\phi(\tau). \tag{1.3}$$

Here $\Phi_0 = \frac{h}{2e}$ is called the magnetic flux quantum. Josephson junctions can be used in applications requiring non-linear inductances in superconducting circuits, in superconducting quantum interferometers to detect small magnetic fields and as control elements to modulate the macroscopic wave function of superconducting quantum information devices [18].

1.1.3 *Cooper pairing and macroscopic coherence*

In Bose-Einstein condensation, the ground state of a gas of interacting bosons can be described as a single macroscopic quantum particle [16]. In the second quantized picture, this is described as a single state occupied by a macroscopic number of bosons. For electrons the situation is subtler as they are indistinguishable spin-$\frac{1}{2}$ particles that must obey fermion statistics. A pure eigenstate s at time τ with N electrons can be described by a wave function of the form

$$\Psi_N^s = \Psi_s\left(\mathbf{r}_1\sigma_1, \mathbf{r}_2\sigma_2, \ldots \mathbf{r}_N\sigma_N\right), \tag{1.4}$$

which is antisymmetric under the exchange of particle coordinates $\mathrm{r}_i\sigma_i \rightleftarrows \mathrm{r}_j\sigma_j$. The most general description of a many-electron state is given by a normalized classical mixture of orthogonal pure states (1.4) with probability weights p_s. The hermitian single-particle density matrix has the form

$$\begin{aligned}
&\rho^{(1)}\left(\mathbf{r}\sigma, \mathbf{r}'\sigma'\right) \\
\equiv\ & \left\langle \psi_\sigma^\dagger\left(\mathbf{r}\right)\psi_{\sigma'}\left(\mathbf{r}'\right)\right\rangle \\
=\ & N\textstyle\sum_s p_s \sum_{\sigma_2\ldots\sigma_N}\int d\mathbf{r}_2\ldots d\mathbf{r}_N \Psi_s^*\left(\mathbf{r}\sigma, \mathbf{r}_2\sigma_2, \ldots \mathbf{r}_N\sigma_N\right) \\
& \times\Psi_s\left(\mathbf{r}'\sigma', \mathbf{r}_2\sigma_2, \ldots \mathbf{r}_N\sigma_N\right) \\
=\ & \textstyle\sum_i n_i^{(1)}\chi_i^*\left(\mathbf{r}\sigma\right)\chi_i\left(\mathbf{r}'\sigma'\right).
\end{aligned} \tag{1.5}$$

This quantity encodes the process of removing a particle with spin σ' at position $\mathbf{r}'$ and finding the probability that the original system is recovered if a particle with spin σ is added at position $\mathbf{r}$. This corresponds to the local density of electrons if $\sigma = \sigma'$ and $\mathbf{r} = \mathbf{r}'$. As a consequence of the Pauli exclusion principle, the eigenvalues $n_i^{(1)}$ of the single-particle density matrix cannot exceed unity (the eigenfunctions are noted $\chi_i\left(\mathbf{r}\sigma\right)$). However, if the electrons can interact and form "virtual molecules" (or Cooper pairs) that themselves interact and condense in a few-body state, there can exist eigenvalues in the two-particle density matrix that are of order N. In other words, all the pairs of fermions can be in the same macroscopic state. This is seen in the two-particle density matrix which is defined as

$$\begin{aligned}
&\rho^{(2)}\left(\mathbf{r}_1\sigma_1, \mathbf{r}_2\sigma_2; \mathbf{r}'_1\sigma'_1, \mathbf{r}'_2\sigma'_2\right) \\
\equiv\ & \left\langle \psi_{\sigma_1}^\dagger\left(\mathbf{r}_1\right)\psi_{\sigma_2}^\dagger\left(\mathbf{r}_2\right)\psi_{\sigma'_2}\left(\mathbf{r}'_2\right)\psi_{\sigma'_1}\left(\mathbf{r}'_1\right)\right\rangle \\
=\ & N\left(N-1\right)\textstyle\sum_s p_s \sum_{\sigma_3\ldots\sigma_N}\int d\mathbf{r}_3\ldots d\mathbf{r}_N \Psi_s^*\left(\mathbf{r}_1\sigma_1, \mathbf{r}_2\sigma_2, \ldots \mathbf{r}_N\sigma_N\right) \\
& \times\Psi_s\left(\mathbf{r}'_1\sigma'_1, \mathbf{r}'_2\sigma'_2, \ldots \mathbf{r}_N\sigma_N\right) \\
=\ & \textstyle\sum_i n_i^{(2)}\chi_i^*\left(\mathbf{r}_1\sigma_1, \mathbf{r}_2\sigma_2\right)\chi_i\left(\mathbf{r}'_1\sigma'_1, \mathbf{r}'_2\sigma'_2\right),
\end{aligned} \tag{1.6}$$

where the eigenvalues have to satisfy the condition $\sum_i n_i^{(2)} = N\left(N+1\right)$. In a qualitative discussion of macroscopic quantum coherence, three cases can be distinguished:

1. If there is no eigenvalue $n_i^{(2)}$ of order N, then the system is in the "normal" uncondensed electron gas;

2. If one eigenvalue $n_i^{(2)}$ is of order N (macroscopic occupation), then this is the case of simple Cooper pairing;

3. If more than one eigenvalue is macroscopically occupied, one can speak of fragmented Cooper pairing.

For example, an electron gas with the weak attractive contact potential

$$U(\mathbf{r}) = -U_0 \delta(\mathbf{r}) \tag{1.7}$$

leads to simple Cooper pairing. In general, the expectation value of the pairing energy is

$$\langle U \rangle = -U_0 \sum_{\sigma_1 \sigma_2} \sum_i n_i^{(2)} \int d\mathbf{r} \left| \chi_i (\mathbf{r}\sigma_1, \mathbf{r}\sigma_2) \right|^2 . \tag{1.8}$$

If a two-particle eigenfunction χ_0 is bounded in the relative coordinates and independent of the center of mass and its eigenvalue N_0 is of order N, then $\langle U \rangle \sim -N_0 U_0$ and the state may lower the energy of the "normal" phase if the condensate formation does not cost too much kinetic energy. A macroscopic "off-diagonal" order parameter can be defined from χ_0 as

$$\begin{aligned} F(\mathbf{r}\sigma, \mathbf{r}'\sigma') &\equiv \sqrt{N_0} \chi_0 (\mathbf{r}\sigma, \mathbf{r}'\sigma') \\ &\equiv \langle \psi_\sigma(\mathbf{r}) \psi_{\sigma'}(\mathbf{r}') \rangle \end{aligned} \tag{1.9}$$

which corresponds to a so-called anomalous pair correlation function whose value vanishes in uncondensed systems but stays finite in the superconducting state. The normalization is the macroscopic occupation number given by

$$N_0 = \sum_{\sigma\sigma'} \iint d\mathbf{r} d\mathbf{r}' \left| F(\mathbf{r}\sigma, \mathbf{r}'\sigma') \right|^2 . \tag{1.10}$$

In typical superconductors, the fraction $\frac{N_0}{N} \sim 10^{-4} - 10^{-2}$ at zero temperature.

To study translation-invariant bulk materials it is useful to introduce the center-of-mass coordinate $\mathbf{R} \equiv \frac{1}{2}(\mathbf{r} + \mathbf{r}')$ and the relative coordinate $\boldsymbol{\rho} \equiv \mathbf{r} - \mathbf{r}'$. The form of $F(\mathbf{R}, \boldsymbol{\rho}, \sigma\sigma')$ at the center of mass $\mathbf{R} = 0$ is fixed by the pairing process and is unique up to a global phase. For example, for s-wave pairing,

$$F(\boldsymbol{\rho}, \sigma\sigma') = f(|\boldsymbol{\rho}|) \times \frac{1}{\sqrt{2}} \left(\delta_{\sigma\uparrow}\delta_{\sigma'\downarrow} - \delta_{\sigma\downarrow}\delta_{\sigma'\uparrow} \right) \tag{1.11}$$

where $f(|\boldsymbol{\rho}|)$ is a function determined by density and temperature and $\delta_{\sigma\sigma'}$ are Kronecker deltas for the spin indices. Such a function also exist for more complicated point group symmetries like $d_{x^2-y^2}$ pairing. Cooper pairing can be understood as "off-diagonal long-range ordering" in the two-particle density matrix (1.6). This means that over long distances $\left|\frac{\mathbf{r}_1+\mathbf{r}_2}{2}-\frac{\mathbf{r}'_1+\mathbf{r}'_2}{2}\right|\to\infty$, the short-range structure ($|\mathbf{r}_1-\mathbf{r}_2|$ and $|\mathbf{r}'_1-\mathbf{r}'_2|$remain finite) of $\rho^{(2)}$ has the form

$$\rho^{(2)}\left(\mathbf{r}_1\sigma_1,\mathbf{r}_2\sigma_2;\mathbf{r}'_1\sigma'_1,\mathbf{r}'_2\sigma'_2\right)\to F^*\left(\mathbf{r}_1\sigma_1,\mathbf{r}_2\sigma_2\right)F\left(\mathbf{r}'_1\sigma'_1,\mathbf{r}'_2\sigma'_2\right)\tag{1.12}$$

which does not involve terms proportional to the "diagonal" electronic density. The macroscopic Ginzburg-Landau order parameter usually derived from phenomenological arguments can be defined from the previous microscopic quantities as

$$\begin{aligned}\Psi\left(\mathbf{R}\right) &\equiv F\left(\mathbf{R},\boldsymbol{\rho}=0,\sigma=\uparrow,\sigma'=\downarrow\right)\\ &\equiv \left|\Psi\left(\mathbf{R}\right)\right|e^{i\varphi(\mathbf{R})}\\ &\equiv \left\langle\psi_\uparrow\left(\mathbf{R}\right)\psi_\downarrow\left(\mathbf{R}\right)\right\rangle.\end{aligned}\tag{1.13}$$

This "anomalous average" is a consequence of the spontaneous breaking of the $U\left(1\right)$ gauge symmetry, it is the same quantity used in the explanation of the Josephson effect in subsection 1.1.2. It can be used to define a coherence length $\xi\sim\frac{E_F}{\pi\Delta}$ representing the characteristic spatial extent of Cooper pairs. The next section covers the precise Green's function formalism used to explicitly derive and compute the quantitative properties of the BCS model.

1.2 INDISTINGUISHABLE INTERACTING FERMIONS

When studyng many-body quantum physics, the effects of quantum statistics must be considered. The many-body wave function of indistinguishable particles has to be invariant to the exchange of any two particles up to a global phase. If the particles are bosons, this global phase factor is $+1$ and the wave function is symmetric under the permutation of particle indices. If this global phase factor is -1 the particles are fermions and their many-body wave function is antisymmetric under the permutation of two particle indices. In order to calculate many useful experimental observables, the complete information of the many-body wave function is not necessary. In most cases the function that describes the propagation of a single electron as it interacts with the system of many electrons is sufficient to compute the desired properties. These are called Green's functions (or correlation functions). By introducing a pseudo spinor notation (Nambu notation), it is possible to describe the microscopic theory of superconductivity from a single-particle picture and quantitatively predict off-diagonal long-range ordering effect.

This section first presents the structure of calculations involving the Green's function formalism, from linear response theory to the Green's function of non-interacting electrons, self-energy and the spectral function for the interacting single-particle Green's function. In the second part, the main elements of BCS theory are expressed in terms of that formalism and the Nambu notation. This section is organized analogous to from [20] and covers the theoretical concepts of condensed matter used in the following chapters.

1.2.1 *Linear response theory and single-particle Green's functions*

1.2.1.1 *The response of a system under a linear perturbation*

At a given time τ, the complete specification of the state of a macroscopic system is described statistically by its many-body density matrix $\rho\left(\tau\right)$. The unperturbed evolution of the system is described by the Hamiltonian H. At equilibrium the total number of particles N is allowed to fluctuate and is fixed by the chemical potential μ. In the grand canonical ensemble, the equilibrium density matrix at inverse temperature $\beta \equiv \frac{1}{k_B T}$ is

$$\rho_0 = \frac{e^{-\beta\left(H-\mu N\right)}}{\mathrm{Tr}\left(e^{-\beta\left(H-\mu N\right)}\right)}. \tag{1.14}$$

If the system is weakly perturbed by some Hamiltonian $H'\left(\tau\right) = A\left(\tau\right)B$ such as an external static field or incoming radiation, its time evolution is governed by Schrödinger's equation such that

$$i\frac{\partial}{\partial\tau}\rho = \left[H + H'\left(\tau\right), \rho\right]. \tag{1.15}$$

If one defines the unitary propagator $U\left(\tau\right) \equiv e^{+iH\tau}$, the average of some macroscopic observable M as a first-order response to the external field $H'\left(\tau\right)$ is given by

$$\begin{aligned} &\left\langle M\right\rangle\left(\tau\right) \\ =\ &\mathrm{Tr}\left(\rho_0 e^{i\left(H\tau + H'\left(\tau\right)\right)} M e^{-i\left(H\tau + H'\left(\tau\right)\right)}\right) \\ \approx\ &\underbrace{\mathrm{Tr}\left(\rho_0 M\right)}_{\bar{M}} - \underbrace{i\mathrm{Tr}\left(MU^{\dagger}\left(\tau\right)\int_0^{\tau} d\tau'\left[U\left(\tau'\right)H'\left(\tau'\right)U^{\dagger}\left(\tau'\right), \rho_0\right]U\left(\tau\right)\right)}_{\delta M\left(\tau\right)}, \end{aligned} \tag{1.16}$$

where $\bar{M}$ is the average equilibrium value and $\delta M\left(\tau\right)$ are the time dependent fluctuations that can be expressed in the following form:

$$\delta M\left(\tau\right) = \int_0^{\infty} d\tau' G_R\left(\tau, \tau'\right) A\left(\tau'\right). \tag{1.17}$$

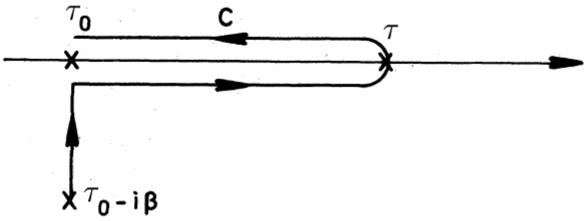

Figure 1.4: Contour representing the time ordering of field operators.

The retarded Green's function carries the effect of the cause of the fluctuations and has the form

$$G_R(\tau,\tau') = -iTr\left(\rho_0\left[U(\tau)\,MU^\dagger(\tau), U(\tau')\,BU^\dagger(\tau')\right]\right)\theta(\tau-\tau')\,. \tag{1.18}$$

For example, in the case where $M(\mathbf{r}) = B(\mathbf{r}) = \psi^\dagger(\mathbf{r})\,\psi(\mathbf{r})$, the corresponding $G_R(\tau,\tau')$ tracks how a fluctuation of density at point $\mathbf{r}'$ and time τ' affects the density at a later time τ at position $\mathbf{r}$.

1.2.1.2 *Green's function formalism in many-body quantum physics*

The single-particle causal Green's function $G(\tau,\tau')$ is a formal object defined with time-ordered field operators in the Heisenberg picture useful in the calculation of many observables. For fermions, it has the form

$$\begin{aligned} & G(\tau,\tau') \\ = \; & -i\left\langle \mathcal{T}\left\{\psi(\tau)\,\psi^\dagger(\tau')\right\}\right\rangle \\ = \; & -i\left\langle\psi(\tau)\,\psi^\dagger(\tau')\right\rangle\theta(\tau-\tau') + i\left\langle\psi^\dagger(\tau')\,\psi(\tau)\right\rangle\theta(\tau'-\tau)\,. \end{aligned} \tag{1.19}$$

The time-ordering operator $\mathcal{T}$ orders field along the contour shown in figure 1.4. The time-dependent retarded (advanced) Green's function for a system at equilibrium can be related to its spectral representation by a Fourier transformation

$$G_{R(A)}(\tau) = \frac{1}{2\pi}\int_{-\infty}^{\infty} d\omega e^{\mp i\omega\tau} G_{R(A)}(\omega)\,. \tag{1.20}$$

The retarded and advanced Green's function are related to the causal Green's function by the analytical continuation

$$G_{R(A)}(\omega) = \lim_{\eta\to 0} G(\omega \pm i\eta) \tag{1.21}$$

which is used in numerical calculation. In a translationally invariant system, momentum is conserved and representing the Green's function using a spatial Fourier transformation yields

$$G(\mathbf{r},\omega) = \frac{1}{\mathcal{V}}\sum_{\mathbf{k}} e^{i\mathbf{k}\cdot\mathbf{r}} G(\mathbf{k},\omega)\,, \tag{1.22}$$

where the corresponding field operators can be transformed according to

$$\psi(\mathbf{r}) = \frac{1}{\sqrt{\mathcal{V}}} \sum_{\mathbf{k}} e^{i\mathbf{k}\cdot\mathbf{r}} c(\mathbf{k}). \tag{1.23}$$

The spectral function which encodes the energy and weights of the poles of the Green's function can be computed from

$$A(\mathbf{k},\omega) = \mp \frac{1}{\pi} \mathrm{Im} G_{R(A)}(\mathbf{k},\omega). \tag{1.24}$$

1.2.1.3 *Interacting electrons*

For concreteness, let's define a general model of electrons moving in an external potential $V(\mathbf{r})$ and interacting through an instantaneous two-body Coulomb potential $U(1,2) = U(\mathbf{r}_1 - \mathbf{r}_2)\,\delta(\tau_1 - \tau_2)$

$$\begin{aligned}
H &= H_0 + H' \\
H_0 &= \textstyle\sum_\sigma \int d^3r \psi_\sigma^\dagger(\mathbf{r}) \left(-\frac{1}{2m}\nabla^2 - \mu - V(\mathbf{r})\right) \psi_\sigma(\mathbf{r}) \\
H' &= \textstyle\frac{1}{2}\sum_{\sigma,\sigma'} \int d^3r d^3r' \psi_\sigma^\dagger(\mathbf{r})\, \psi_{\sigma'}^\dagger(\mathbf{r}')\, U(\mathbf{r}-\mathbf{r}')\, \psi_{\sigma'}(\mathbf{r}')\, \psi_\sigma(\mathbf{r}),
\end{aligned} \tag{1.25}$$

such that H_0 contains the kinetic and static contributions to the energy and H' is the interaction term. The commutation relations of the fermionic fields are given by

$$\begin{aligned}
\left\{\psi_\sigma(\mathbf{r}), \psi_{\sigma'}^\dagger(\mathbf{r}')\right\} &= \psi_\sigma(\mathbf{r})\, \psi_{\sigma'}^\dagger(\mathbf{r}') + \psi_{\sigma'}^\dagger(\mathbf{r}')\, \psi_\sigma(\mathbf{r}) = \delta_{\sigma\sigma'}\delta(\mathbf{r}-\mathbf{r}') \\
\left\{\psi_\sigma(\mathbf{r}), \psi_{\sigma'}(\mathbf{r}')\right\} &= 0.
\end{aligned} \tag{1.26}$$

To compute the single-particle spectral function (1.24) for the interacting problem H, one usually starts by solving the non-interacting H_0 where particles behave independently. The non-interacting single-particle Green's function $G_0(1;1')$ is obtained. To keep the notation short, numeral indices like "1" refer to position and time $(\mathbf{r}_1, \tau_1)$ of the fields. For indistinguishable non-interacting fermions, the two-particle correlation function has to be antisymmetric under particle exchange and it can be written as

$$G_{02}(1,2;1',2') = G_0(1,1')\, G_0(2,2') - G_0(1,2')\, G_0(2,1'). \tag{1.27}$$

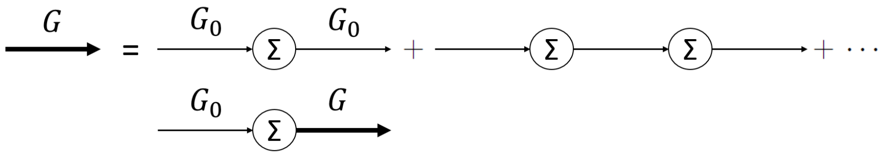

Figure 1.5: Diagrammatic representation of the relation between the single-particle Green's function G, the bare Green's function of the non-interacting system G_0 and the self-energy Σ.

This generalizes to the n-particle Green's function for non-interacting fermions by computing the determinant

$$\begin{aligned}
&G_{0n}\left(1,2,\ldots,n;1',2',\ldots,n'\right)\\
&=\begin{vmatrix} G_0\left(1,1'\right) & G_0\left(1,2'\right) & \cdots & G_0\left(1,n'\right)\\ G_0\left(2,1'\right) & G_0\left(2,2'\right) & \cdots & G_0\left(2,n'\right)\\ \vdots & \vdots & \ddots & \vdots\\ G_0\left(n,1'\right) & G_0\left(n,2'\right) & \cdots & G_0\left(n,n'\right)\end{vmatrix}.
\end{aligned} \tag{1.28}$$

With the partition function $Z \equiv \mathrm{Tr}\left(e^{-\beta H}\right)$, the interacting single-particle Green's function is defined as

$$\begin{aligned}
G\left(1;2\right) \;=\; & -\tfrac{i}{Z}\mathrm{Tr}\left(e^{-\beta H}e^{iH\tau_1}\psi\left(\mathbf{r}_1\right)e^{-iH(\tau_1-\tau_2)}\psi^{\dagger}\left(\mathbf{r}_2\right)e^{-iH\tau_2}\right)\theta\left(\tau_1-\tau_2\right)\\
& +\tfrac{i}{Z}\mathrm{Tr}\left(e^{-\beta H}e^{iH\tau_2}\psi^{\dagger}\left(\mathbf{r}_2\right)e^{-iH(\tau_2-\tau_1)}\psi\left(\mathbf{r}_1\right)e^{-iH\tau_1}\right)\theta\left(\tau_2-\tau_1\right).
\end{aligned} \tag{1.29}$$

As shown in figure 1.5, the self-energy Σ is a quantity defined by the Dyson equation, a recursive diagrammatic equation to sum all orders of perturbation theory of the interacting problem H:

$$G\left(1,2\right)=G_0\left(1,2\right)+\int d1'd2'G_0\left(1,1'\right)\Sigma\left(1',2'\right)G\left(2',2\right). \tag{1.30}$$

For a time-independent Hamiltonian, the Green's function takes the form

$$G\left(\omega\right)=\int_{-\infty}^{\infty}dz\frac{A\left(z\right)}{\omega-z} \tag{1.31}$$

where the spectral function in the Lehmann representation has the form

$$A\left(\omega\right)=\frac{1}{Z}\sum_{m,n}\left(e^{-\beta E_m}+e^{-\beta E_n}\right)A_{mn}B_{nm}\delta\left(\omega-E_n+E_m\right) \tag{1.32}$$

and can be computed numerically with diagram methods. Everything required to formulate BCS theory has now been defined.

1.2.2 *The microscopic theory of superconductivity*

The phenomenon of superconductivity can be explained from a microscopic model of interacting fermions such as (1.25). Following the discussion of section 1.1.3, the superconducting order parameter can be described by a function $F(\mathbf{r}\sigma, \mathbf{r}'\sigma')$ averaging combination of field operators that do not converse the total number of particles. In the case where there is a small attractive interaction between the electrons near the Fermi level, the ground state becomes unstable and $F(\mathbf{r}\sigma, \mathbf{r}'\sigma')$ acquires a finite value. It is therefore useful to work in the grand canonical ensemble where the Heisenberg representation of the field operators (1.23) are given by

$$\begin{aligned} \tilde{\psi}_\sigma(\mathbf{r},\tau) &\equiv e^{i\tau(H-\mu N)}\psi_\sigma(\mathbf{r})\,e^{-i\tau(H-\mu N)} \\ \tilde{\psi}^\dagger_\sigma(\mathbf{r},\tau) &\equiv e^{i\tau(H-\mu N)}\psi^\dagger_\sigma(\mathbf{r})\,e^{-i\tau(H-\mu N)}. \end{aligned} \tag{1.33}$$

Assuming that the pairing interaction has an even parity in the orbital space (such as isotropic s-wave or $d_{x^2-y^2}$ symmetric interaction), then it is useful to define the correlation functions of the spin-singlet Cooper pairs (1.9) averaged on the contour of figure 1.4 as matrices over the spin indices

$$\begin{aligned} F_{\sigma\sigma'}(\mathbf{r},\tau;\mathbf{r}',\tau') &\equiv -i\left\langle \mathcal{T}\left\{\tilde{\psi}_\sigma(\mathbf{r},\tau)\,\tilde{\psi}_{\sigma'}(\mathbf{r}',\tau')\right\}\right\rangle \\ &= \begin{pmatrix} 0 & F(\mathbf{r},\tau;\mathbf{r}',\tau') \\ -F(\mathbf{r},\tau;\mathbf{r}',\tau') & 0 \end{pmatrix} \\ F^\dagger_{\sigma\sigma'}(\mathbf{r},\tau;\mathbf{r}',\tau') &\equiv i\left\langle \mathcal{T}\left\{\tilde{\psi}^\dagger_\sigma(\mathbf{r},\tau)\,\tilde{\psi}^\dagger_{\sigma'}(\mathbf{r}',\tau')\right\}\right\rangle \\ &= \begin{pmatrix} 0 & F^*(\mathbf{r},\tau;\mathbf{r}',\tau') \\ -F^*(\mathbf{r},\tau;\mathbf{r}',\tau') & 0 \end{pmatrix}. \end{aligned} \tag{1.34}$$

These functions are often referred to as the "anomalous" or Gor'kov functions. As seen in section 1.1.3, in the presence of long-range quantum coherence these functions can receive the contribution of a macroscopic number of particles and have a finite value. Assuming the weak contact interaction (1.7), it is also useful to introduce the pairing potentials

$$\begin{aligned} \Delta_{\sigma\sigma'}(\mathbf{r},\tau) &\equiv |U_0|\,F_{\sigma\sigma'}(\mathbf{r},\tau;\mathbf{r},\tau) \\ &= \begin{pmatrix} 0 & \Delta(\mathbf{r},\tau) \\ -\Delta(\mathbf{r},\tau) & 0 \end{pmatrix}. \end{aligned} \tag{1.35}$$

The BCS gap is then defined as $\Delta(\mathbf{r},\tau) \equiv |U_0|\, F(\mathbf{r},\tau;\mathbf{r},\tau)$. At this point, it is helpful to introduce the Nambu pseudo spinor notation

$$\hat{\psi} \equiv \begin{pmatrix} \psi_{\uparrow} \\ \psi_{\downarrow}^{\dagger} \end{pmatrix} \tag{1.36}$$

such that the Nambu representation of the Green's function can be defined in the compact form

$$\begin{aligned} \hat{G}(\mathbf{r},\tau;\mathbf{r}',\tau') &\equiv -i\left\langle \mathcal{T}\left\{\hat{\psi}(\mathbf{r},\tau)\,\hat{\psi}(\mathbf{r}',\tau')\right\}\right\rangle \\ &= \begin{pmatrix} G(\mathbf{r},\tau;\mathbf{r}',\tau') & F(\mathbf{r},\tau;\mathbf{r}',\tau') \\ -F^{*}(\mathbf{r},\tau;\mathbf{r}',\tau') & G(\mathbf{r}',\tau';\mathbf{r},\tau) \end{pmatrix}. \end{aligned} \tag{1.37}$$

The equation governing the Green's function can be embodied in a dynamic operator

$$\hat{K}\left(\mathbf{r},\tau;\mathbf{r}',\tau'\right) \equiv \begin{pmatrix} -i\frac{\partial}{\partial\tau} - \frac{\nabla^2}{2m} - \mu & -\Delta(\mathbf{r},\tau) \\ \Delta^{*}(\mathbf{r},\tau) & i\frac{\partial}{\partial\tau} - \frac{\nabla^2}{2m} - \mu \end{pmatrix} \tag{1.38}$$

such that the essence of BCS theory can be summarized by Gor'kov's equation [21]

$$\hat{G}^{-1}\left(\mathbf{r},\tau;\mathbf{r}',\tau'\right) = \hat{K}\left(\mathbf{r},\tau;\mathbf{r}',\tau'\right) \tag{1.39}$$

from which the order parameter $\Delta(\mathbf{r},\tau)$ can be determined self-consistently. If an electron with a given wave vector $\mathbf{k}$ has energy $\epsilon_{\mathbf{k}}$ then the Fourier transformed Nambu Green's function has the form

$$\hat{G}(\mathbf{k},\omega) = \frac{1}{\omega^2 - \epsilon_{\mathbf{k}}^2 - |\Delta_{\mathbf{k}}|^2} \begin{pmatrix} \omega + \epsilon_{\mathbf{k}} & \omega - \Delta_{\mathbf{k}} \\ \omega - \Delta_{\mathbf{k}}^{*} & \omega + \epsilon_{\mathbf{k}} \end{pmatrix} \tag{1.40}$$

where the poles

$$\omega = \pm E_{\mathbf{k}} \equiv \pm\sqrt{\epsilon_{\mathbf{k}}^2 + |\Delta_{\mathbf{k}}|^2} \tag{1.41}$$

are the gapped energies of the quasi-particles in the superconductor.

For an isotropic superconductor where the attractive interaction is mediated by phonons characterized by a Debye frequency ω_D, BCS theory predicts an s-wave gap whose self-consistent equation is

$$\Delta = U_0 \Delta \sum_{\mathbf{k}} \frac{1 - 2f(E_{\mathbf{k}})}{2E_{\mathbf{k}}}, \tag{1.42}$$

where $f(\omega)$ is the Fermi distribution. If the density of state at the Fermi energy is denoted $N(E_F)$, then at zero temperature the BCS gap is given by the function

$$\Delta(T=0) = 2\omega_D e^{-\frac{1}{N(E_F)U_0}}, \tag{1.43}$$

which cannot be expanded as a power series in small U_0, which explains the failure of a direct perturbation theoretic treatment of the superconducting problem. The simple electron-phonon mediated interaction of BCS theory yields a transition temperature of the form

$$T_c = 1.13\frac{\omega_D}{k_B}e^{-\frac{1}{N(E_F)U_0}}. \tag{1.44}$$

A spectacular prediction of BCS theory is the universal dimensionless ratio

$$\frac{2\Delta\left(T=0\right)}{k_B T_c} = 3.53. \tag{1.45}$$

The temperature dependence of the gap is found to follow a universal transcendental relation

$$\Delta\left(T\right) = 1.77 k_B T_c e^{F\left[\frac{\Delta(T)}{T}\right]} \tag{1.46}$$

for some function F. BCS theory is now a well established and tested theory, but the discovery of new superconducting materials from the 1980's challenged the notion that it is the complete picture of superconducting phenomena in general.

1.3 CUPRATES AND HIGH-TEMPERATURE SUPERCONDUCTIVITY

In 1986, cuprate ceramics with transition temperature above 35°K were discovered by J. Bednorz and K. Müller [22]. As shown in figure 1.6, new cuprate materials were quickly discovered with superconducting transition temperature above the boiling point of nitrogen [23]. These material have found important technological applications as power transmission cables and coils for powerful magnets. However, as their crystal structure is more complex, the microscopic pairing mechanism at the origin of cuprate superconductivity is not completely understood and there is no systematic procedure to design materials which could superconduct at room temperature. Josephson tunneling experiments indicate that superconductivity caused by the formation of Cooper pairs, but as there is almost no isotope effect, it is known that phonons do not play a central role in the pairing mechanism. The crystal structure is highly anisotropic, as is the order parameter, which is known to be a spin singlet and to have $d_{x^2-y^2}$ orbital symmetry. The electron-electron interaction is strongly dependent on the stoichiometry of the compounds, as adding charge donors or acceptors may change the superconducting phase to an anti-ferromagnetic state.

What is known exactly about the cuprates [16]? As shown in figure 1.7, the chemical formula of cuprates is of the form

$$\left(\mathrm{CuO_2}\right)_n \mathrm{A}_{n-1}\mathrm{X}, \tag{1.47}$$

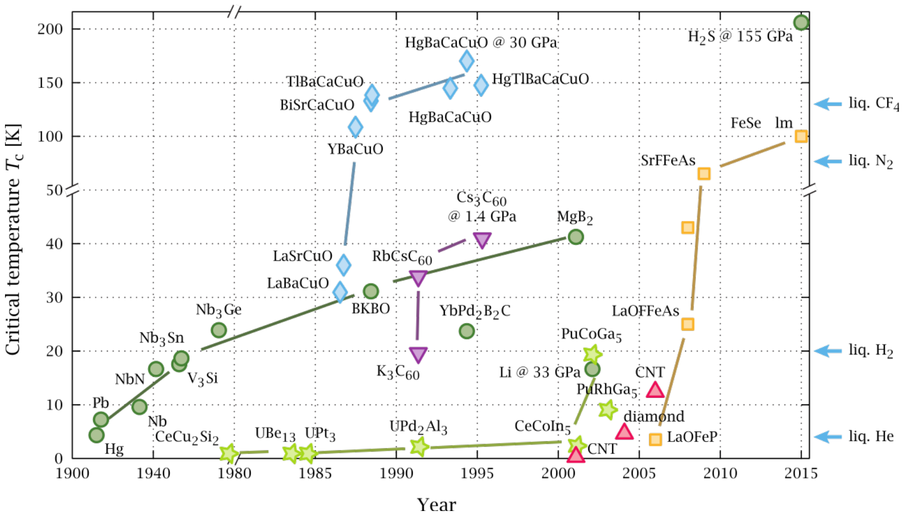

Figure 1.6: Critical temperature of superconducting materials by their year of discovery Typical BCS superconductors are represented by green circles, the blue rhombi represent cuprate superconductors. On the right side, the boiling temperature of common cryogenic fluids is shown. This figure has been reproduced from [24].

where n copper oxide planes CuO_2 are interspaced by $n-1$ alkaline earth or rare earth atoms A and a "charge reservoir" group X. The copper oxide planes are common to all these materials and hence are believed to be the locus of superconductivity in cuprates. For example, $La_{2-x}Sr_xCuO_4$ has only $n = 1$ layer (no spacer A), $Bi_2Sr_2CaCu_2O_{8+\delta}$ has $n = 2$ layers interspaced by calcium atoms and $Sr_xCa_{1-x}CuO_2$ has no charge group but essentially $n = \infty$. Materials with a fixed spacer A and charge group X but different n form homologous series. For a given homologous series the superconducting transition temperature typically increases with the number of CuO_2 planes but appears to saturate and decrease for $n > 3$. As the hopping time between different multilayers is much larger than the characteristic time of Cooper pair dynamics, the multilayers can be viewed as independent stacks of quasi-2D lattices. The layered structure also strongly modulates the transport properties of the crystal as the conductance along the c-axis is a few orders of magnitude lower than in the in-plane direction. Measurements of the critical magnetic field indicates that Cooper pairs have a characteristic size of $10-30$ which is roughly fours order of magnitude smaller than in normal BCS superconductors.

The charge reservoir X is used to control the density of charges around the copper oxide planes. As shown in figure 1.8, superconductivity appears only in a narrow range of hole doping $p \sim 0.05 - 0.27$ at low temperature. Close to the charge neutral system $p < 0.04$, neutron diffraction experiments show that cuprates are antiferromagnets. In between the two phases is a "strange metal" phase which exhibits properties of magnetic spin glasses. When the copper

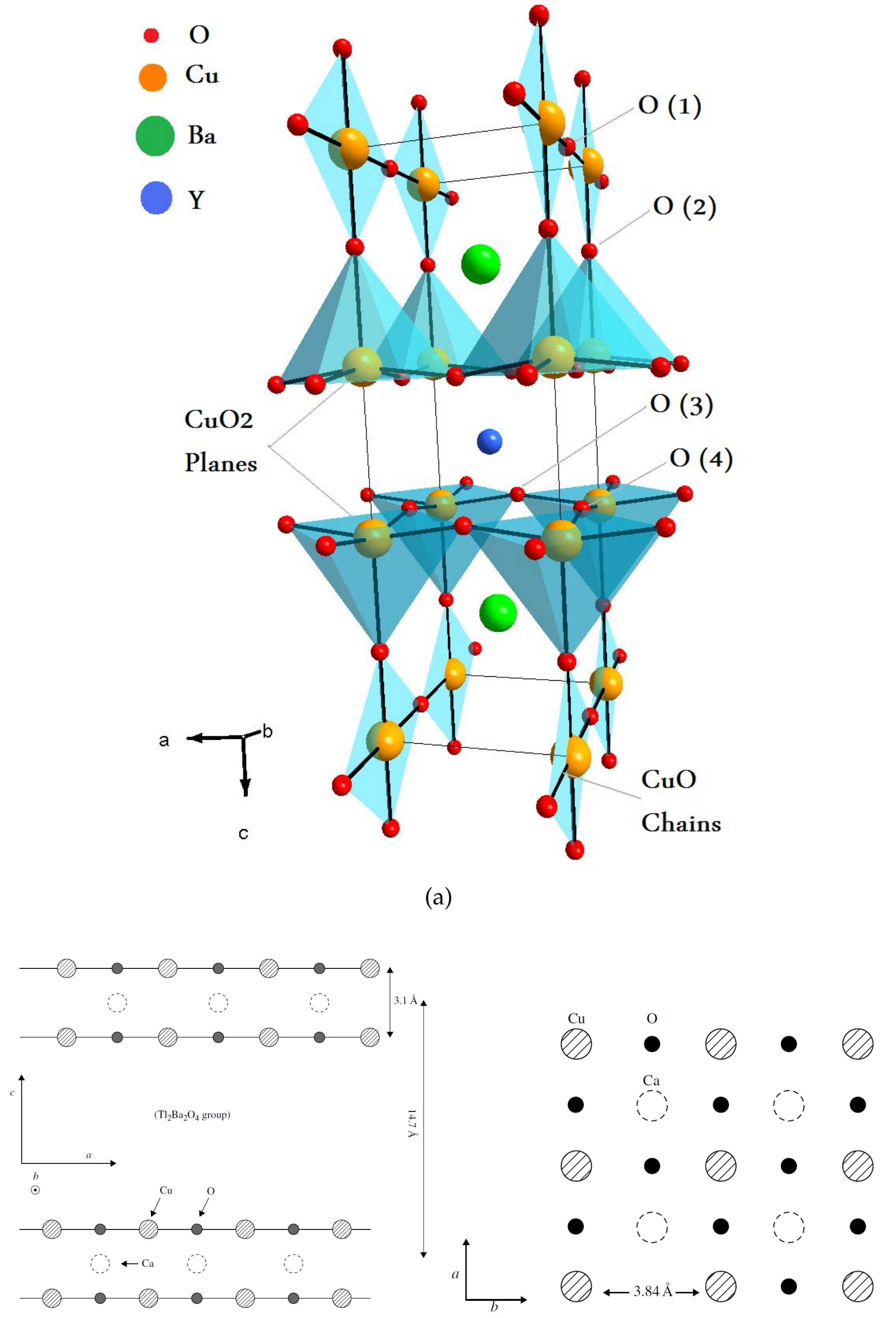
O
Cu
Ba
Y
O (1)
O (2)
CuO2
Planes
O (3)
O (4)
a
b
c
CuO
Chains
3.1 Å
14.7 Å
(Tl$_2$Ba$_2$O$_4$ group)
c
a
b
Cu
O
Ca
Cu
O
Ca
a
b
3.84 Å

(a)

(b)

(c)

Figure 1.7: Cuprates are complex and intricate materials. In (a), the orthorhombic crystalline unit cell of $YBa_2Cu_3O_{7-x}$ ($T_c = 92$°K at $x \approx 0.15$) has $n = 2$ CuO_2 layers spaced by yttrium atoms. Additional structures such as CuO chains can be found in cuprates. In (b) and (c) show respectively the vertical and the in-place cross-sections of $Tl_2Ba_2CaCuO_8$ ($T_c = 108$°K) with a tetragonal structure. Figure (a) has been reproduced from [25], while figures (b) and (c) have been reproduced from [16].

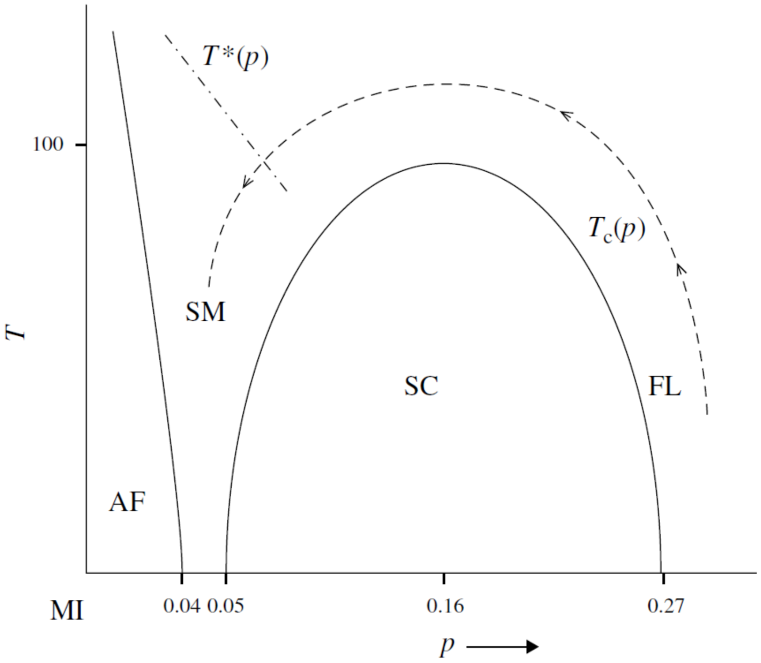

Figure 1.8: The typical phase diagram of superconducting cuprates as a function of "hole doping" p (controlled by stoichiometry) and temperature T. Between half-filling $p = 0$ to $p \approx 0.04$, the material is an anti-ferromagnet (AF) up to high temperatures. The superconducting dome (SC) appears for $0.05 < p < 0.27$ and T_c often reaches ~ 100°K for $p \approx 0.16$. For dopings $p > 0.27$, the electrons behave as a traditional Fermi liquid (FL). Going around the dome back to $0.04 < p < 0.05$, there is a transition to a "strange metal" phase (SM) where the interaction between spin waves produces a spin glass behavior. This figure has been reproduced from [16].

oxide planes are depleted in electrons such that $p > 0.27$ then the standard Fermi liquid behavior is recovered.

P. W. Anderson proposed that superconductivity in cuprates comes from the repulsive Coulomb interaction between the conduction electrons in the $d_{x^2-y^2}$ orbital of the copper sites [26]. The simplest model with these characteristics is the two-dimensional Fermi-Hubbard model (FHM) [27]. In the undoped regime there is one electron per $d_{x^2-y^2}$ orbital (for each Cu). The local electronic repulsion explains the Mott insulating behavior and the ground state orders the local magnetic moments in an anti-ferromagnetic pattern with spin-waves as elementary excitations. Increasing the number of holes opens an interaction channel between spin waves until the anti-ferromagnetic ordering is lost and the interacting quasi-particle picture starts to dominate. The hole-like excitations interact through spin-waves such that the conduction electrons condense into Cooper pairs. A complete theory of the full spectrum of excitations in the 2D FHM is still missing and may well be impossible to develop for the general strong correlation problem [28]. The FHM is the simplest model which is hoped to contain most of the essential ingredients for explaining cuprate superconductivity. One can think that interacting FHM lattices could be used to explain the critical temperature trends in homologous series. Indeed, a repulsive interaction between in-plane Cooper pairs could produce a Bose-Einstein condensation effect in multilayers as well as increase the density of states close to the Fermi surface [29–31].

2

THE FERMI-HUBBARD MODEL

2.1 OVERVIEW

The FHM [27] is a central tool in the study of strongly correlated electrons in condensed matter physics [32, 33]. It captures the simplest essence of the atomic structure of materials and the second quantization of the many-body interacting wave function. It can be used to model the Mott insulator phenomenon in transition metals [27, 34], itinerant magnetism [35], high-T_c superconductors [26, 36–38], heavy-fermion compounds [39], atoms in optical lattices [40, 41] and many others. It was also used to chemistry to describe extended π-electron systems in the Pariser-Parr-Pople model [42–44], where hopping and interaction are defined on a graph of spin orbitals. The exact solutions to the one-dimensional Hubbard model are known and well understood [45–47] but the two- and three-dimensional models are known not to have general closed form solutions and are subject to important theoretical studies [48–54]. An elegant approximation method valid for short-range interactions is cluster perturbation theory (CPT), where a lattice is divided into manageable identical clusters which are solved and then recomposed into a lattice through with perturbation theory [55, 56]. However, the method is not sufficient to systematically account for broken symmetries in the FHM and has to be extended. In superconductors and anti-ferromagnets, local interactions can have long-range effects and order parameters can appear in different regions of phase space. These effects can be taken into account in the Green's function of a cluster by finding the stationary point of the lattice's grand canonical potential when the self-energy of a cluster is taken as the variational parameter [57–59]. This self-energy functional theory (SFT) is a great computational tool to study the important macroscopic thermodynamic phases of the Hubbard model starting from its microscopic description. In the context of the SFT, the CPT approximation is generalized to what is known as the variational cluster approach (VCA).

This chapter aims at being self-contained by providing all the concepts required to implement the solver on a general purpose quantum computer [60]. It is structured in the following manner. Section 2.3 summarizes the VCA used to compute properties of the FHM. In subsection 2.3.1, a variational principle of the self-energy for the grand canonical potential of the model is outlined such that it can account for possible long-range ordering effects. Subsection 2.3.2 formalizes the approximation where the FHM lattice is divided in independent clusters linked with hopping terms. Section 2.4 introduces the detailed formal description of a cluster using the example of a 2D lattice with superconductivity starting in subsection 2.4.1. Subsection 2.4.2 proceeds with reviewing the formalism to compute the Green's function of the lattice from the independent clusters and subsection 2.4.3 lists methods to compute observables of interest once the variational problem is solved. Section 3.3 covers the computer intensive step where the eigenvalue problem of the cluster Hamiltonian must be solved at each iteration of the variational solver. Subsection 2.5 summarizes the solution method on a classical computer.

2.2 THE FERMI-HUBBARD MODEL

The FHM is an effective description of the microscopic physics of the electrons in a solid [20] useful in calculating the properties of Fermi liquids [16], Mott insulators, anti-ferromagnets , superconductors and other metallic phases. The model describes a simple electronic band in a periodic lattice Γ where electrons are free to hop between orbitals (or sites) with kinetic energy t and interact via a simple two-body Coulomb term U analogous to Eq. (1.7) (but here the effective screened interaction is repulsive).

The model describes a simple electronic band in a periodic square lattice where electrons are free to hop between orbitals (or sites) with kinetic energy t and interact via a simple two-body Coulomb term U. The standard form of the FHM Hamiltonian is given by

$$\mathcal{H} = -t \sum_{\langle i,j \rangle,\sigma} c^{\dagger}_{i\sigma} c_{j\sigma} + U \sum_{i} n_{i\uparrow} n_{i\downarrow} - \mu \sum_{i,\sigma} n_{i\sigma}, \tag{2.1}$$

where μ is the chemical potential that controls the occupation of the band n. The $c_{i\sigma}(c^{\dagger}_{i\sigma})$ are the fermionic annihilation (creation) operators and the number operators are $n_{i\sigma} = c^{\dagger}_{i\sigma} c_{i\sigma}$. The hopping energy $t = 1$ is assumed to be the reference energy and inverse time unit. Assuming that the lattice is translationally invariant and and only nearest-neighbor hopping is considered, then the only parameters that control the physics of the FHM are the ratio $\frac{U}{t}$, the filling factor n, the temperature T and the geometry of the lattice. As only few parameters are involved, it is one of the simplest model of correlated electrons.

The model is analytically solvable in the tight-binding limit $\frac{U}{t} \to 0$ and the atomic limit $\frac{t}{U} \to 0$. For a finite $\frac{U}{t}$, there is competition from different orders (anti-ferromagnetism, superconductivity). No general solution is known for more than one dimension [46, 47, 61], where the solution is found exactly with the Bethe ansatz and behaves like a Tomonaga-Luttinger liquid. In low dimensions, the kinetic and interaction energies are on the same scale, so perturbation theory from either a wave or particle picture quickly diverges. Other methods such as random phase approximation satisfy conservation laws but violate the Mermin-Wagner theorem and the Pauli principle. Since the double occupancy of a site $\langle n_{i\uparrow} n_{i\downarrow} \rangle$ is an important quantity in the physics FHM, the violation of the Pauli principle does not allow for reliable solutions. At low temperatures relevant to the superconducting phenomenon, quantum Monte Carlo (QMC) has a sign problem [62] which is such that studying the low-temperature phases of the FHM yields ambiguous results [63, 64]. The difficulty and proliferation of coupling constants in the renormalization group approach is unbiased but generally requires additional approximations.

Many numerical methods have been developed to compute the thermodynamic properties of the FHM [32, 65]. As such, dynamical mean-field theory (DMFT) does not take into account the strong momentum dependence of the self-energy in low-dimension systems and cannot model d-wave superconductivity in the FHM. However, as shown in figure 2.1, mean field methods like the dynamical impurity approximation (DIA) and DMFT [66–68], unified under the broader SFT [56, 57, 69], can asymptotically approach solutions of the model by simulating the dynamics of increasingly larger clusters that contain the information of the quantum fluctuations of the system. Numerical clusters methods are the VCA and cellular dynamical mean-field theory (CDMFT), which is defined with self-consistent equations [70, 71]. Another method is the dynamical cluster approximation (DCA), which trades off the spatial continuity of the self-energy to avoid the artificial translation symmetry breaking of the lattice of the other cluster methods. However, simulating those clusters on a classical computer is a task that requires an exponential amount of computing resources as the cluster size is increased.

2.2.1 *Some known properties*

In $D = 1$, the exact solutions of the FHM can be calculated with the Bethe ansatz [46, 47, 61]. The ground state energy can be calculated exactly and it can be shown that for $U \neq 0$ the 1D chain undergoes a Mott metal-insulator transition at half-filling (one electron per site). The correlation functions can be computed from quantum inverse scattering methods [72]. In the $D \to \infty$ limit, DMFT can be applied to obtain exact solutions of the FHM [66, 68] and model a Mott transition between a paramagnetic metal and a correlated insulator.

The Hamiltonian (2.1) has several symmetries which are independent of the dimensionality of the lattice [54] (of course, the Hamiltonian has the spatial symmetry of the translation-invariant lattice). First, it conserves the total number of particles $N = \sum_{\mathbf{r}} \sum_{\sigma} c^{\dagger}_{\mathbf{r}\sigma} c_{\mathbf{r}\sigma}$, which can be viewed as a consequence of gauge symmetry. On a lattice which can be partitioned into two sublattices A and B where each

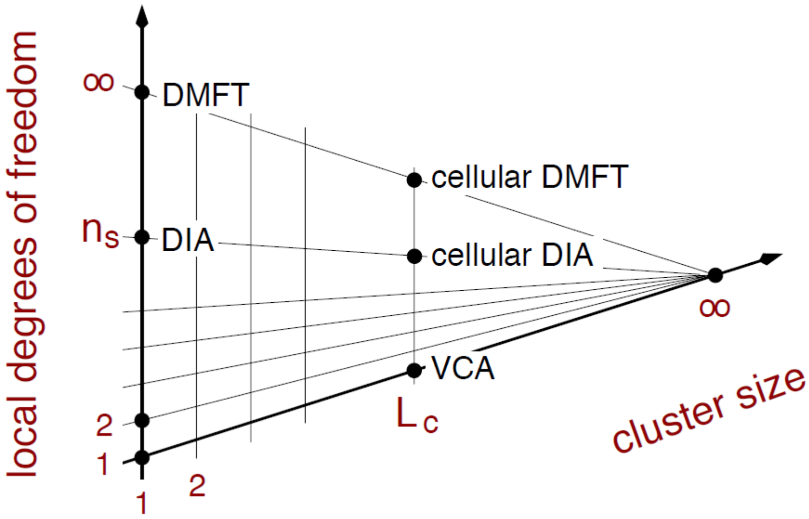
local degrees of freedom
∞
DMFT
cellular DMFT
n_s
DIA
cellular DIA
∞
VCA
2
1
L_c
1
2
cluster size

Figure 2.1: The landscape of numerical methods for the strong correlation problem. In the DIA, a cluster has only one correlated site $L_c = 1$ and n_s uncorrelated bath sites, neglecting all non-local two-particle spatial correlations. The limit $n_s \to \infty$ of the DIA is DMFT. In the VCA, there are more than one site $L_c > 1$ to account for spatial correlations. Adding bath sites to the VCA to increase the dynamical accuracy of the simulation yields the cellular DIA and the limit $n_s \to \infty$ is CDMFT, which is usually solved with self-consistent loops. This figure has been reproduced from [69].

node in A is only connected to nodes in B (and vice-versa, such as a checkerboard partition of the square lattice), the particle-hole transformation $c^{\dagger}_{\mathbf{r}\sigma} \rightleftharpoons (-1)^{\mathbf{r}} c_{\mathbf{r}\sigma}$ leaves the Hamiltonian invariant at half-filling. In general, the Hamiltonian also has a $SU(2)$ symmetry with respect to the components of the global spin operator $\mathbf{S} = \begin{pmatrix} S_x & S_y & S_z \end{pmatrix}$ and its magnitude $\mathbf{S}^2$ as $\mathcal{H}$, S_z and $\mathbf{S}^2$ can be diagonalized simultaneously. The eigenvalue of $\mathbf{S}^2$ are noted $S(S+1)$ where S is the spin of the eigenstate, if $S \propto N$ has an extensive value, then the state is ferro- or ferri-magnetic. The components of the spin operators form an algebra $\left[S_x, S_y\right] = iS_z$ and are defined as the sum over all space

$$S_\alpha = \sum_{\mathbf{r}} S_{\alpha\mathbf{r}} \tag{2.2}$$

of the local spin operators $\mathbf{S}_{\mathbf{r}} = \begin{pmatrix} S_{x\mathbf{r}} & S_{y\mathbf{r}} & S_{z\mathbf{r}} \end{pmatrix}$ whose components $\alpha = \{x, y, z\}$ are given by

$$S_{\alpha\mathbf{r}} = \frac{1}{2} \sum_{\sigma\sigma'} c^{\dagger}_{\mathbf{r}\sigma} \left(\sigma_\alpha\right)_{\sigma\sigma'} c_{\mathbf{r}\sigma'}, \tag{2.3}$$

where the Pauli matrices have the standard form

$$\begin{aligned} \sigma_x &= \begin{pmatrix} 0 & 1 \\ 1 & 0 \end{pmatrix} \\ \sigma_y &= \begin{pmatrix} 0 & -i \\ i & 0 \end{pmatrix} \\ \sigma_z &= \begin{pmatrix} 1 & 0 \\ 0 & -1 \end{pmatrix}. \end{aligned} \tag{2.4}$$

At half-filling on bipartite lattices with L sites, there is another $SU(2)$ symmetry that can be obtained from a modified particle-hole transformation. It's generators are

$$\begin{aligned} \hat{S}_z &= \tfrac{1}{2}(N-L) \\ \hat{S}_+ &= \textstyle\sum_{\mathbf{r}\in A} c^{\dagger}_{\mathbf{r}\uparrow} c^{\dagger}_{\mathbf{r}\downarrow} - \sum_{\mathbf{r}\in B} c^{\dagger}_{\mathbf{r}\uparrow} c^{\dagger}_{\mathbf{r}\downarrow} \\ \hat{S}_- &= \hat{S}^{\dagger}_+. \end{aligned} \tag{2.5}$$

Therefore, at half-filling on bipartite lattices, the FHM has a $SU(2) \otimes SU(2) = SO(4)$ symmetry.

Some theorems concerning the magnetic behavior of the FHM at $T = 0$ are knowns for systems of finite size. For example, Lieb's theorem [73] states that the ground state of the attractive FHM $U < 0$ with

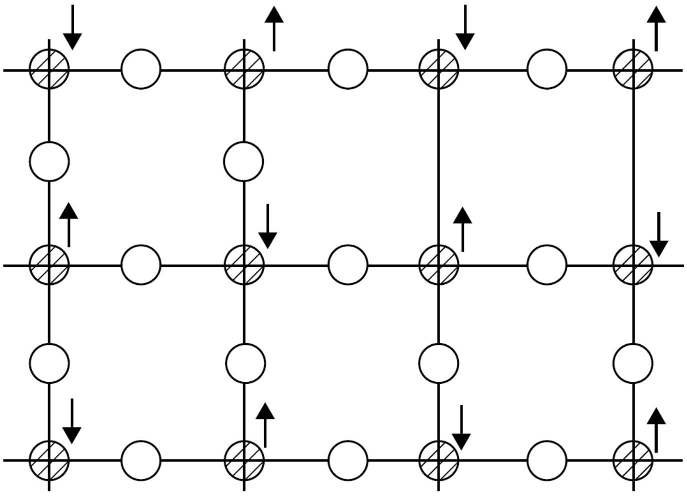

Figure 2.2: The Mott insulating anti-ferromagnetic state at half-filling on a CuO_2 plane.. This figure has been reproduced from [16].

an even number of particles is unique and has total spin zero $S = 0$. Functional renormalization calculations notably find a s-wave instability in the repulsive regime [53]. As as corollary to Lieb's theorem, the ground state of the repulsive model $U > 0$ in the zero S_z subspace is known to be unique and the total spin S follows Hund's rule. An example is the anti-ferromagnetic state illustrated in figure 2.2. As a function of the filling factor n, renormalization theory can identify an anti-ferromagnetic instability close to half-filling and $d_{x^2-y^2}$ pairing when a small negative next-nearest-neighbor hopping t' is included in the model. More ordering phenomena like ferromagnetism, f-wave pairing and anisotropic Pomeranchuk deformations of the Fermi surface are found as more complex features are added to the FHM [54]. For weak interaction, a Fermi liquid is typically expected.

2.2.1.1 *The Mermin-Wagner theorem*

The Mermin-Wagner theorem [74] encapsulates many of the contentions about the physics at play in the FHM. Essentially, it states that continuous symmetry (like $U(1)$ or $SU(2)$) cannot be broken at finite temperature in less than three spatial dimensions. This implies that thermal fluctuations are commensurate with all ordering mechanisms and superconductivity [75] and crystalline order [76] cannot be stable in two dimensions and less. The Mermin-Wagner theorem [74] applied to the 2D FHM [77] states that correlation functions at non-zero temperature decay spatially as following the power laws

$$\left|\left\langle c_{i\uparrow}^{\dagger} c_{i\downarrow}^{\dagger} c_{j\downarrow} c_{j\uparrow} \right\rangle\right| \leq \begin{cases} \left|\mathbf{r}_i - \mathbf{r}_j\right|^{-\alpha T} & \text{if } T \ll T_0 \\ \left|\mathbf{r}_i - \mathbf{r}_j\right|^{-2\alpha T_0 \ln T} & \text{if } T \gg T_0 \end{cases} \tag{2.6}$$

for $\alpha > 0$ and T_0 some constant temperature. This is derived in the thermodynamic limit and assumes that the hopping has a finite range. As a consequence, there should be no spontaneous transition or long-range ordering at finite temperature in the FHM. But like in the case of 2D materials like graphene, some "medium range" ordering can occur and be stabilized by weak long-range interactions [78]. It also does not forbid continuous Kosterlitz-Thouless transitions, where the ground state is a bound pair of vortex and anti-vortex which dissociates at critical temperature T_0. In the case of the FHM, a fictitious long-range molecular Weiss field can be introduced as computational tool to study continuous transitions. This strongly suggests using cluster methods for numerical approaches of the problem. The Mermin-Wagner theorem also acts as a blessing in the sense that the very long-range behavior of the correlation functions is trivial and clusters encompassing a small region on the scale of a few times the coherence length ξ should be sufficient to model the strongly correlated physics. This fundamentally remains a hard problem as it has been shown that scattering in the FHM is sufficient to implement universal quantum computation [52]. Moreover, generalized versions of the FHM can be well defined and constructed such that it is not possible to decide whether their excitation spectra are gapped or not in the thermodynamic limit [28], signifying the infinite richness of strongly correlated physics.

2.3 SOLVING THE FERMI-HUBBARD MODEL WITH THE VARIATIONAL CLUSTER APPROACH

The type of data that we want to simulate in the FHM are thermodynamic phase information and electrodynamic properties [29] such as angular-resolved photoemission spectroscopy (ARPES) spectra [79, 80]. The goal of this section is to introduce the important physical quantities of the main loop of the numerical variational solver used to extract properties of the FHM. Since the interesting observables typically correspond to the response of the system to external perturbations, the central object of study is the Green's function which contains both the thermal and the dynamical properties of the system (see section 1.2). To compute the Green's function, a variational principle on the grand canonical potential is derived from functional arguments. The Green's functional variational problem is then mapped to a self-energy variational problem to account for possible spontaneous symmetry breaking from long-range ordering in a self-consistent manner. At last the lattice approximation is introduced to complete the description of the lattice variational solver.

2.3.1 *The grand canonical potential as a functional of the self-energy*

Since the anomalous quantities Eq. (1.34) do not conserve the total number of particles, the thermodynamic quantities are evaluated in the grand canonical ensemble from the grand potential

$$\begin{aligned}\Omega &\equiv -T\ln Z \\ &= \langle E\rangle - TS - \mu\langle N\rangle ,\end{aligned} \tag{2.7}$$

where Z is the partition function and S is the entropy. Average quantities can be evaluated from the relations

$$\begin{aligned}\langle N\rangle &= -\tfrac{\partial\Omega}{\partial\mu} \\ S &= -\tfrac{\partial\Omega}{\partial T}.\end{aligned} \tag{2.8}$$

Since we want to work with dynamical quantities, the grand potential has to be expressed as a functional of a Green's function (1.37).

2.3.1.1 *The Luttinger-Ward formalism*

The Green's function $\mathbf{G}$ of the full system described by $\mathcal{H}$ can be obtained exactly from the bare single-particle Green's function of the non-interacting lattice (tight-binding) $\mathbf{G_{0t}}$ and the self-energy $\mathbf{\Sigma} = \mathbf{G_{0t}^{-1}} - \mathbf{G}^{-1}$ by solving the Dyson equation represented in figure 1.5

$$\mathbf{G} = \mathbf{G_{0t}} + \mathbf{G_{0t}}\mathbf{\Sigma}\mathbf{G}. \tag{2.9}$$

When there is no interaction, the self-energy is zero and the tight-binding Green's function for a given one-body hopping matrix $\mathbf{t}$ is

$$\mathbf{G_{0t}^{-1}} = \omega - \mathbf{t}. \tag{2.10}$$

The model can be considered "solved" once the single-particle Green's function $\mathbf{G}$ can be computed accurately for any interesting input coordinates (such as position / momentum, time / energy). A method to obtain the Green's function consists in rewriting the Dyson equation as a variational principle on the grand canonical potential of the system. To accomplish this task, it is useful to introduce the Luttinger-Ward functional [59, 82] of the Green's function $\Phi[\mathbf{G}]$ which generates all two-body skeleton diagrams (see figure 2.3) and has the interesting property that its functional derivative with respect to $\mathbf{G}$ is simply

$$\frac{\delta\Phi[\mathbf{G}]}{\delta\mathbf{G}} = \mathbf{\Sigma}. \tag{2.11}$$

Furthermore, the functional form of $\Phi[\mathbf{G}]$ depends only on the form of the interaction U and is independent of the one-body terms in

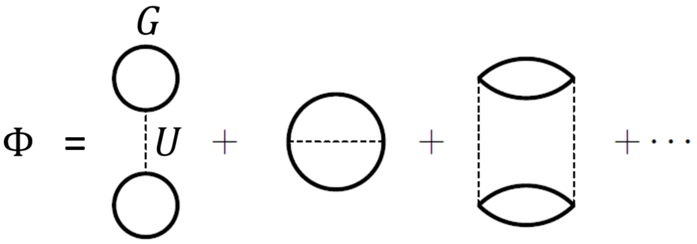

Figure 2.3: The Luttinger-Ward functional Φ is a scalar representing the sum of all the two-body dressed skeleton diagrams. The dressed skeleton diagrams are defined as closed connected diagrams of the fully interacting propagator without external propagators and self-energy diagram insertions [81]. The functional derivative of a dressed skeleton corresponds to the removal of a propagator line and results in a dressed skeleton diagram with two links for external propagators which contributes to the self-energy. The functional derivative with respect to $\mathbf{G}$ gives all the diagrams for the computation of $\mathbf{\Sigma}$. In the case where $U = 0$ then $\Phi\left[\mathbf{G}\right] = 0$.

$\mathcal{H}$. In statistical mechanics, observables are derived from a thermodynamic potential. For many-body systems, it is typically easier to let the total number of particles fluctuate and work with the grand canonical ensemble. The grand canonical potential of the full lattice can be defined from the Luttinger-Ward functional as a functional of $\mathbf{G}$

$$\Omega_t\left[\mathbf{G}\right] = \Phi\left[\mathbf{G}\right] - \mathrm{Tr}\left[\left(\mathbf{G}_{\mathbf{0t}}^{-1} - \mathbf{G}^{-1}\right)\mathbf{G}\right] + \mathrm{Tr}\ln\left[-\mathbf{G}\right], \tag{2.12}$$

such that the Dyson equation (2.9) can be recovered as the stationary point with respect to the variation of $\mathbf{G}$:

$$\frac{\delta\Omega_t\left[\mathbf{G}\right]}{\delta\mathbf{G}} = \mathbf{\Sigma} - \mathbf{G}_{\mathbf{0t}}^{-1} + \mathbf{G}^{-1} = 0. \tag{2.13}$$

In Ref. [58], Potthoff describes three types of approximation strategy to solve this variational problem. A type I approximation would try to simplify the Euler equation from a heuristic argument but could suffer from thermodynamic inconsistencies. A type II approximation would correspond to computing the $\Phi\left[\mathbf{G}\right]$ functional only for a finite set of diagrams, but justifying the use of a particular functional form over other possibilities is in itself not trivial. Finally, in a type III approximation, thermodynamical consistency is preserved as well as the exact form of the Luttinger-Ward functional but the trial Green's functions are chosen from a restricted domain where the self-energy is constrained. The VCA is a type III approximation. The main advantage of this type of scheme is that it allows for a systematic construction of increasingly accurate solutions to many-body problems with local interactions. In the case of the FHM, a good scheme to systematically approximate the self-energy is to consider a reference lattice of isolated clusters Γ' with the same local interaction term U as the lattice Γ and pick $\mathbf{\Sigma}$ from the exact solution of the reference lattice. This method allows for the construction of solutions to the FHM that are very accurate except for long range correlations that exceed the dimensions of the clusters. The main advantage of this scheme is that the solutions are guaranteed to become asymptotically exact as the size of the cluster reaches the size of the original lattice. The next step consists in rewriting the grand canonical potential Ω_t as a functional of the lattice self-energy Σ instead of the Green's function $\mathbf{G}$.

2.3.1.2 *Self-energy functional theory*

The variational principle of the self-energy of a cluster [57] intends to account for solutions of the Hubbard model with spontaneous symmetry breaking caused by long-range interactions. The grand canonical potential $\Omega_t\left[\mathbf{G}\right]$ can be rewritten as a functional of the self-energy $\Omega_t\left[\mathbf{\Sigma}\right]$ by applying the Legendre transformation $\mathbf{G}\left[\mathbf{\Sigma}\right] = \left(\mathbf{G_{0t}^{-1}} - \mathbf{\Sigma}\right)^{-\mathbf{1}}$ such that

$$\begin{aligned} \Omega_t\left[\mathbf{G}\right] &= \Phi\left[\mathbf{G}\right] - \mathrm{Tr}\left[\left(\mathbf{G_{0t}^{-1}} - \mathbf{G^{-1}}\right)\mathbf{G}\right] + \mathrm{Tr}\ln\left[-\mathbf{G}\right] \\ &= \underbrace{\Phi\left[\mathbf{G}\right] - \mathrm{Tr}\left[\Sigma\mathbf{G}\right]}_{\Lambda[\Sigma]} + \mathrm{Tr}\ln\left[-\mathbf{G}\right] \\ &= \Lambda\left[\mathbf{\Sigma}\right] - \mathrm{Tr}\ln\left[-\mathbf{G_{0t}^{-1}} + \mathbf{\Sigma}\right] \\ &= \Omega_t\left[\mathbf{\Sigma}\right]. \end{aligned} \tag{2.14}$$

Let's then notice that $\Omega_t\left[\mathbf{\Sigma}\right]$ is still exact and now only depends on the self-energy Σ and the non-interacting Green's function $\mathbf{G_{0t}}$. The Legendre transformed Luttinger-Ward functional $\Lambda\left[\mathbf{\Sigma}\right]$ has the nice property

$$\frac{\delta\Lambda\left[\mathbf{\Sigma}\right]}{\delta\mathbf{\Sigma}} = -\mathbf{G}, \tag{2.15}$$

which is used to recover the Dyson equation of the system and the variational principle depending on the self-energy

$$\frac{\delta\Omega_t\left[\mathbf{\Sigma}\right]}{\delta\Sigma} = \left(\mathbf{G_{0t}^{-1}} - \Sigma\right)^{-1} - \mathbf{G} = 0. \tag{2.16}$$

As shown in figure 2.4, solutions to the FHM can be found by varying the self-energy until a physical value of the Green's function is found and the Dyson equation is satisfied. However, since this is in general a saddle-point problem, the optimal point cannot be interpreted as an

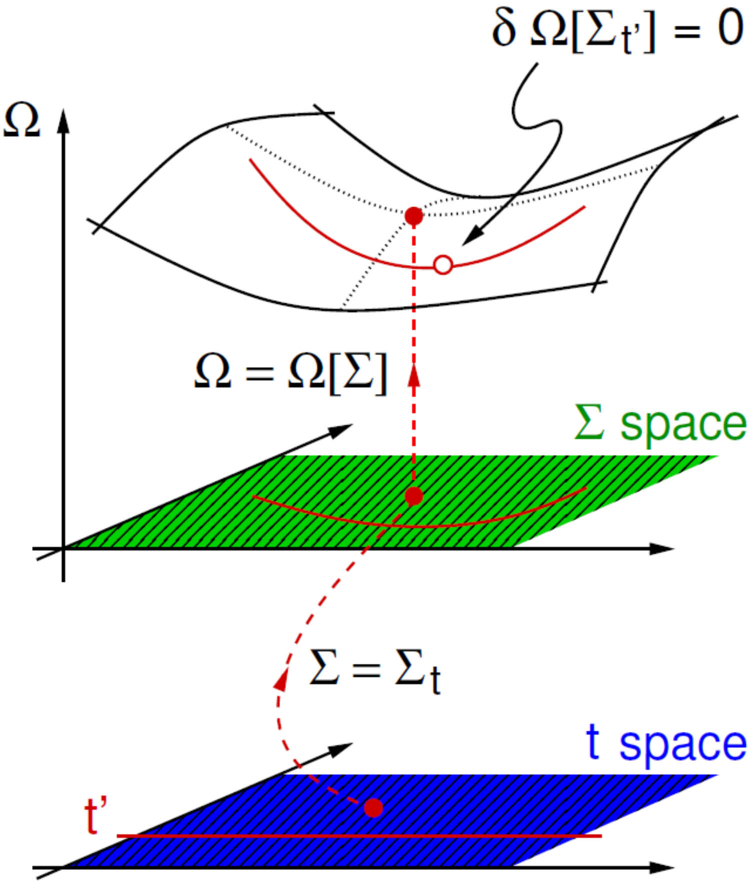

Figure 2.4: How the different functional spaces are connected. The red dots represent the exact self-energy at the stationary point of Eq. 2.16. The functional dependence of $\Omega_t\,[\boldsymbol{\Sigma}]$ is not known for the complete space of self-energies, but only those parametrized by the single-particle parameters $\mathbf{t}'$ shown by the red lines. The stationary point on that sub-manifold corresponds to the approximate grand canonical potential. This figure has been reproduced from [69].

upper bound to the exact energy (as in the Ritz variational method) but as the most "physical" approximation of the grand canonical potential allowed by a given parametrization of the self-energy. Computing the exact single-particle self-energy for a large lattice and storing the result are tasks beyond the capabilities of classical computers. The idea of cluster methods used to approximate the solution of the full lattice Γ is to divide it into a reference lattice Γ' of clusters of a small number (i.e. computer tractable) of sites, solve a cluster exactly and use perturbation theory to approximate the properties of the full lattice.

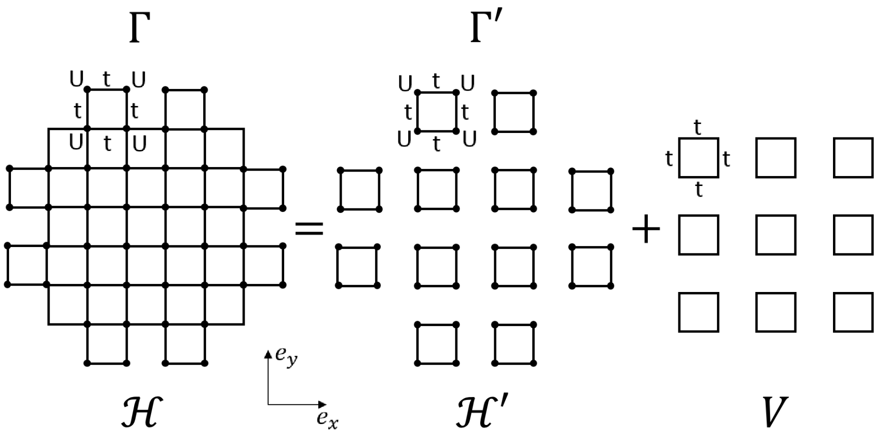

Figure 2.5: The essence of the VCA method is to remove the one-body links (denoted t) between small clusters (contained in $\mathbf{V}$) from the lattice Γ and consider only the reference lattice Γ' whose Hamiltonian $\mathcal{H}'$ is block diagonal in the Wannier basis and easier to solve than the complete problem $\mathcal{H}$. The reference system generates a manifold of trial self-energies Σ' parametrized by single-particle parameters $\mathbf{t}'$. The self-energy functional can be evaluated exactly on this manifold as the interaction part of the Hamiltonian (the Us) is left unchanged.. The solution becomes asymptotically exact as the clusters are made to include more sites.

2.3.2 *The variational cluster approach*

Large lattices with millions of orbitals are impossible to simulate exactly on classical computers since the memory required to store for the associated state vectors scales exponentially in cluster size. A method to mitigate this problem makes use of the translation invariance of the lattice. It consists in breaking down the lattice in several independent clusters and making use of the universality of the Luttinger-Ward functional to recast the variational equation (2.16) on a cluster-restricted domain of the self-energy. The exact solutions are recovered when the size of the cluster is equal to the size of the original lattice [83].

Good and thorough introductions to the VCA method can be found in [56, 84]. In the restricted Hilbert space of a cluster, the goal is to variationally find a self-energy Σ' such that it is most physical (by satisfying the VCA version of the Dyson equation) and minimizes the free energy. As hinted at the end of subsection 2.3.1 and shown in figure 2.5, the VCA approximation consists in subdividing a full lattice Γ into a reference lattice of identical clusters Γ' and solving the reference model exactly in order to obtain its self-energy Σ'. In this context, the Green's function of a cluster is a frequency dependent matrix given by

$$\mathbf{G}'^{-1}(\omega) = \omega - \mathbf{t}' - \Sigma'(\omega) \tag{2.17}$$

The Legendre transformed Luttinger-Ward functional Λ only depends on the interaction part of the Hamiltonian. Since by definition the interaction part of the Hamiltonian is the same for the full system and the reference system, the identity $\Lambda\left[\mathbf{\Sigma}'\right] = \Lambda\left[\mathbf{\Sigma}\right]$ must hold. Let's note that this scheme would not work directly in the case of the extended FHM (where there is intersite interaction), since a reference system of independent clusters cannot be found by simply removing one-body links of the Hamiltonian [85]. As in Eq. (2.14), the grand canonical potential of the reference system is given by

$$\Omega' \equiv \Omega_{t'}\left[\mathbf{\Sigma}'\right] = \Lambda\left[\mathbf{\Sigma}\right] - \operatorname{Tr}\ln\left[-\mathbf{G}'\right], \tag{2.18}$$

where $\mathbf{G}'$ is the Green's function of the reference system. When they are both evaluated at the self-energy of the reference system, the difference between the grand canonical potential of the full lattice and the reference system is

$$\Omega_{t}\left[\mathbf{\Sigma}'\right] = \Omega' + \operatorname{Tr}\ln\left[-\mathbf{G}'\right] - \operatorname{Tr}\ln\left[-\mathbf{G}\right]. \tag{2.19}$$

This relation is exact, the only approximation of the VCA is in the restriction of the domain of the self-energy. It can be further simplified as the VCA is built within SFT as a well-defined variational extension to the CPT. The full lattice Green's function $\mathbf{G}\left[\mathbf{\Sigma}\right]$ is equal to the CPT Green's function if its self-energy is restricted to the domain of the reference system. As in figure 2.5, it is useful to define $\mathbf{V} \equiv \mathbf{t} - \mathbf{t}'$ as a perturbation, where $\mathbf{t}$ contains all the one-body terms of the full lattice Γ and $\mathbf{t}'$ represents all the one-body terms of the lattice of clusters Γ'. As a result of strong-coupling perturbation theory, the CPT Green's function is given by

$$\mathbf{G}\left[\mathbf{\Sigma}'\right] = \mathbf{G}_{\mathrm{cpt}} = \left(\mathbf{G}'^{-1} - \mathbf{V}\right)^{-1}. \tag{2.20}$$

With some algebra, Eq. (2.19) can be written as

$$\Omega_{t}\left[\mathbf{\Sigma}'\right] = \Omega' - \operatorname{Tr}\ln\left[\mathbf{1} - \mathbf{V}\mathbf{G}'\right]. \tag{2.21}$$

The functional is exact as no classes of diagrams have been explicitly excluded. At the saddle-point, it represents the quantity which is physically the closest to the physical grand canonical potential of the full lattice when the self-energy is computed on the reference lattice. The effect of single-particle correlations and intra-cluster two-particle correlations is treated non-perturbatively but the inter-cluster two-particle effects are neglected in the one-particle spectrum. Even if only a small cluster is exactly solved, the self-energy variational principle (2.16) can be used to study the properties of the infinite system like the various order parameters in a thermodynamically consistent framework. Since the VCA is a well defined generalization of the CPT, it also shares similar characteristics. It is exact in the limit $\frac{U}{t} \to 0$ where the self-energy disappears to yield the tight binding model. It is also exact in the strong-coupling limit $\frac{t}{U} \to 0$, where all sites are effectively decoupled. The method is easy to generalize to non-homogeneous lattices. The next section introduces the details of the objects required to compute (2.21) and find its stationary point as well as some observables that can then be calculated.

2.4 EXAMPLE ON A SQUARE LATTICE WITH SUPERCONDUCTIVITY

In this section the self-energy variational approach is used to model superconductivity in a FHM lattice. A more general formulation of possible orders could be made (for arbitrary ordering potentials and cluster graph), but the goal of this section is only to introduce the types of formal elements required to describe a cluster. Other types of order parameters can be found in the literature [39]. First the different terms in the Hamiltonian of the cluster are explained. Then the detailed formalism of the VCA is given through the example of a square lattice with superconductivity. Finally, various quantities involved in the computation of useful observables are listed. Some of my numerical results on a 2×2 cluster are included as examples of calculations.

2.4.1 *Hamiltonian of a cluster*

Each cluster includes only a small portion of the terms of the original lattice and variational terms must also be included to account for possible long-range order. For convenience, let's assume that Γ is a square lattice with constant spacing a. It is broken down into N_c clusters each with L_c orbitals ("sites") with two electrons each (spin up $\uparrow$ and spin down $\downarrow$). The small parameter in the approximation is L_c^{-1}, which means that increasing the size of the cluster also increases the accuracy of the simulation. The Hamiltonian of each cluster is given by

$$\mathcal{H}' = \mathcal{H}_{\text{FH}} + \mathcal{H}_{\text{local}} + \mathcal{H}_{\text{s-pair}} + \mathcal{H}_{\text{d}_{\text{x}^2-\text{y}^2}} + \mathcal{H}_{\text{AF}}, \tag{2.22}$$

where the FHM terms remaining in Γ' are given by

$$\mathcal{H}_{\text{FH}} = -t \sum_{\langle i,j \rangle,\sigma} c_{i\sigma}^{\dagger} c_{j\sigma} + U \sum_{i} n_{i\uparrow} n_{i\downarrow}, \tag{2.23}$$

which is the same as (2.1) without the chemical potential term. The chemical potential must be kept as a variational term to enforce the thermodynamic consistency of the electronic occupation value

$$\mathcal{H}_{\text{local}} = -\mu' \sum_{i,\sigma} n_{i\sigma}. \tag{2.24}$$

It can be seen that at the stationary point $\frac{\partial \Omega_t}{\partial \mathbf{t}'} = 0$, the electronic occupation expectation value is

$$\langle n \rangle = \operatorname{Tr} \mathbf{G} = -\frac{d\Omega_t}{d\mu} = -\left(\frac{\partial \Omega_t}{\partial \mu} + \frac{\partial \Omega_t}{\partial \mathbf{t}'} \cdot \frac{d\mathbf{t}'}{d\mu} \right) \tag{2.25}$$

where the two methods converge to the same average occupation at the stationary point. Keeping the chemical potential fixed in the cluster Hamiltonian would break this condition.

The ordered phases of the FHM can be studied by introducing artificial symmetry breaking terms to the cluster Hamiltonian and treating them as variational variable. The choice of these terms is somewhat arbitrary and is usually justified by the physics of the system studied. For example in the FHM, it is often interesting to study the competition between superconducting order parameters with different symmetries and the anti-ferromagnetic ordering. A variational singlet pairing term is introduced as

$$\mathcal{H}_{\mathrm{s-pair}} = \Delta' \sum_i \left(c^\dagger_{i\uparrow} c^\dagger_{i\downarrow} + c_{i\downarrow} c_{i\uparrow} \right), \tag{2.26}$$

while a $d_{x^2-y^2}$ singlet pairing takes the form [56]

$$\mathcal{H}_{\mathrm{d_{x^2-y^2}}} = \Delta'_d \sum_{ij} d_{ij} \left(c^\dagger_{i\uparrow} c^\dagger_{j\downarrow} + c_{j\downarrow} c_{i\uparrow} \right), \tag{2.27}$$

where $\mathbf{R}$ are the vector positions of the sites in the cluster and

$$d_{ij} = \begin{cases} 1 & \text{if } \mathbf{R}_i - \mathbf{R}_j = \pm a \mathbf{e_x} \\ -1 & \text{if } \mathbf{R}_i - \mathbf{R}_j = \pm a \mathbf{e_y} \\ 0 & \text{otherwise.} \end{cases} \tag{2.28}$$

The variational Néel anti-ferromagnetic Weiss field takes the form

$$\mathcal{H}_{\mathrm{AF}} = M' \sum_i e^{i\mathbf{Q}\cdot\mathbf{R}_i} \left(n_{i\uparrow} - n_{i\downarrow} \right), \tag{2.29}$$

where $\mathbf{Q} = (\pi, \pi)$ is the anti-ferromagnetic wave vector.

2.4.2 *The superlattice of clusters*

The relation between the original lattice and the lattice of clusters is given in more details along with useful notations. The main objects of interest also used in the quantum subroutine of chapter 3 are introduced in this subsection.

2.4.2.1 *The superlattice in reciprocal space*

To make the procedure clear and concrete, let's work on the example of the superconducting order parameter on a 2D lattice. For a good

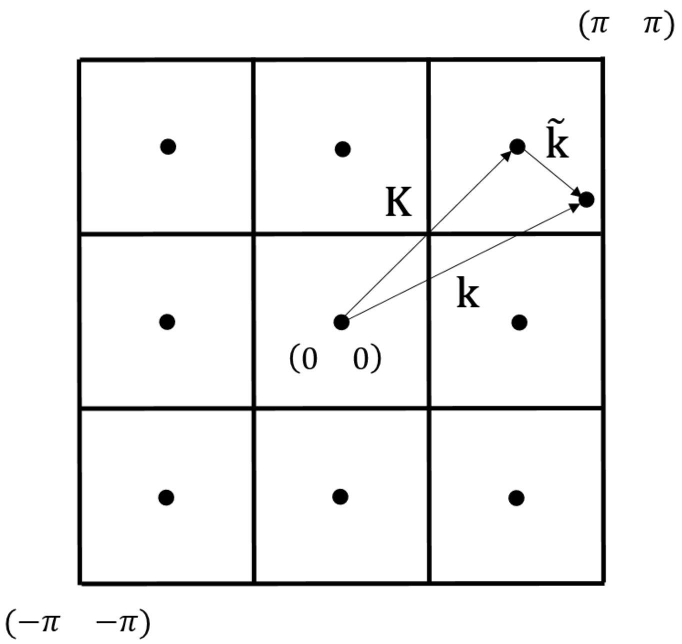

Figure 2.6: Reduced Brillouin zone of the reciprocal lattice. The quasi-momentum vector **k** belong to the reciprocal lattice of Γ while the K component belongs to the reciprocal lattice of a single cluster. The $\tilde{\mathbf{k}}$ vector belongs to the reciprocal superlattice (hopping between clusters).

explanation of quantum cluster theories and the details for computations on clusters of arbitrary size see [56, 84]. A square lattice with 8 orbitals per cluster is required to study s-wave and d-wave superconductivity in the FHM. Let's take a lattice Γ with N sites and divide it in clusters of $L_c = 2 \times 2 = 4$ sites, then the number of clusters is simply $N_c = \frac{N}{L_c}$. Let's label these 4 sites as 1, 2, 3 and 4. As shown in figure 2.6, when the full lattice is Fourier transformed, the first Brillouin zone in quasi-momentum space is given by

$$k_{x/y} = \frac{2\pi m_{x/y}}{\sqrt{N}a}, \quad m_{x/y} = 0, \ldots, \sqrt{N} - 1 \tag{2.30}$$

and the reciprocal superlattice is given by

$$\tilde{k}_{x/y} = \frac{2\pi q_{x/y}}{\sqrt{N_c}a}, \quad q_{x/y} = 0, \ldots, \sqrt{N_c} - 1 \ . \tag{2.31}$$

2.4.2.2 *The saddle-point problem*

The observable properties of the Hamiltonian (2.1) can be computed from the CPT formula (2.20) by finding variational parameters (μ',Δ', Δ'_d, M', etc.) that generate Σ for which the Dyson equation (2.16) is stationary. In practice, this condition is reformulated explicitly over the variational parameters as

$$\frac{\partial \Omega_t}{\partial \mathbf{t}'} = 0. \tag{2.32}$$

In the superconducting FHM example, this would correspond to solving the saddle-point problem

$$\begin{pmatrix} \frac{\partial \Omega_t}{\partial \mu'} \\ \\ \frac{\partial \Omega_t}{\partial \Delta'} \\ \\ \frac{\partial \Omega_t}{\partial \Delta'_d} \\ \\ \frac{\partial \Omega_t}{\partial M'} \end{pmatrix} = \begin{pmatrix} 0 \\ 0 \\ 0 \\ 0 \end{pmatrix}, \tag{2.33}$$

which is done efficiently on a classical computer once $\Omega_t\left[\mathbf{t}'\right]$ can be evaluated for a given set of parameters (for example, by a Newton-Raphson method). In the case of a lattice problem, the grand potential functional takes the following form

$$\Omega_t = \Omega'_{t'} - \frac{1}{N} \oint_C \frac{dz}{2\pi i} \sum_{\tilde{\mathbf{k}}} \ln \det \left[\hat{\mathbf{I}} - \hat{\mathbf{V}}\left(\tilde{\mathbf{k}}\right) \hat{\mathbf{G}}'\left(z\right) \right], \tag{2.34}$$

where $\hat{\mathbf{V}}\left(\tilde{\mathbf{k}}\right)$ and $\hat{\mathbf{G}}'\left(z\right)$ both depend on the chosen variational parameters (the hat notation is explained below, it refers to the Nambu space). The contour integral $\oint_C dz$ can be done as a real line integral, as a Matsubara sum or as an efficient summation based on the continued fraction expansion of the Fermi function [86] .

2.4.2.3 *The eigenvalue problem*

In order to evaluate the energy-dependent Green's function $\hat{\mathbf{G}}'\left(z\right)$, the eigenvalue problem for one cluster

$$\mathcal{H}' \left|\phi_n\right\rangle = E_n \left|\phi_n\right\rangle \tag{2.35}$$

must be solved for different parameters until the stationary point is reached. For $2L_c$ orbitals , the eigenvalue problem of the Hamiltonian can be solved in the occupation eigenbasis defined by

$$\left|n_{1\uparrow} \dots n_{L_c\uparrow} n_{1\downarrow} \dots n_{L_c\downarrow}\right\rangle = \prod_{i=1}^{L_c} \left(c^\dagger_{i\uparrow}\right)^{n_{i\uparrow}} \prod_{i=1}^{L_c} \left(c^\dagger_{i\downarrow}\right)^{n_{i\downarrow}} \left|\mathrm{Vac}\right\rangle, \tag{2.36}$$

where $\left|\mathrm{Vac}\right\rangle$ is the many-body vacuum. The dimension of this Hilbert space is 4^{L_c} which means that storing the matrices of the calculation scales prohibitively with cluster size on a classical computer. Let's note that spatial symmetries that commute with the cluster Hamiltonian $\mathcal{H}'$ can be used to reduce the memory requirement of the computation [56]. In all cases, it is useful to introduce the Nambu (singlet particle-hole) space notation. This notation is especially useful when considering quantum mechanical problems where an order parameter can appear from broken gauge symmetries. In this space, field operators are replaced by a vector $\hat{\psi}_i^\dagger = \begin{pmatrix} c_{i\uparrow}^\dagger & c_{i\downarrow} \end{pmatrix}$ such that the energy-dependent Green's function of a cluster can be represented in the form

$$\begin{aligned} \hat{\mathbf{G}}'(\omega) &\equiv \left\langle \hat{\psi}\hat{\psi}^\dagger \right\rangle_\omega \\ &= \begin{pmatrix} \mathbf{G}'(\omega) & \mathbf{F}'(\omega) \\ \mathbf{F}'^\dagger(\omega) & -\mathbf{G}'(-\omega) \end{pmatrix}, \end{aligned} \tag{2.37}$$

where the elements $G'_{ij}(\omega) = \left\langle c_{i\uparrow} c_{j\uparrow}^\dagger \right\rangle_\omega$ are the components of the single-particle Green's function and $F'_{ij}(\omega) = \left\langle c_{i\uparrow} c_{j\downarrow} \right\rangle_\omega$ are the components of the anomalous Green's function (see section 1.2.2). The $\langle \ldots \rangle_\omega$ notation corresponds to the frequency-dependent correlation function (i.e., the Fourier transformed two-point time correlation function). In the 4-site example, these matrices would have the form

$$\mathbf{G}'(\omega) = \begin{pmatrix} \left\langle c_{1\uparrow}c_{1\uparrow}^\dagger \right\rangle_\omega & \left\langle c_{1\uparrow}c_{2\uparrow}^\dagger \right\rangle_\omega & \left\langle c_{1\uparrow}c_{3\uparrow}^\dagger \right\rangle_\omega & \left\langle c_{1\uparrow}c_{4\uparrow}^\dagger \right\rangle_\omega \\ \left\langle c_{2\uparrow}c_{1\uparrow}^\dagger \right\rangle_\omega & \left\langle c_{2\uparrow}c_{2\uparrow}^\dagger \right\rangle_\omega & \left\langle c_{2\uparrow}c_{3\uparrow}^\dagger \right\rangle_\omega & \left\langle c_{2\uparrow}c_{4\uparrow}^\dagger \right\rangle_\omega \\ \left\langle c_{3\uparrow}c_{1\uparrow}^\dagger \right\rangle_\omega & \left\langle c_{3\uparrow}c_{2\uparrow}^\dagger \right\rangle_\omega & \left\langle c_{3\uparrow}c_{3\uparrow}^\dagger \right\rangle_\omega & \left\langle c_{3\uparrow}c_{4\uparrow}^\dagger \right\rangle_\omega \\ \left\langle c_{4\uparrow}c_{1\uparrow}^\dagger \right\rangle_\omega & \left\langle c_{4\uparrow}c_{2\uparrow}^\dagger \right\rangle_\omega & \left\langle c_{4\uparrow}c_{3\uparrow}^\dagger \right\rangle_\omega & \left\langle c_{4\uparrow}c_{4\uparrow}^\dagger \right\rangle_\omega \end{pmatrix} \tag{2.38}$$

and

$$\mathbf{F}'(\omega) = \begin{pmatrix} \left\langle c_{1\uparrow}c_{1\downarrow} \right\rangle_\omega & \left\langle c_{1\uparrow}c_{2\downarrow} \right\rangle_\omega & \left\langle c_{1\uparrow}c_{3\downarrow} \right\rangle_\omega & \left\langle c_{1\uparrow}c_{4\downarrow} \right\rangle_\omega \\ \left\langle c_{2\uparrow}c_{1\downarrow} \right\rangle_\omega & \left\langle c_{2\uparrow}c_{2\downarrow} \right\rangle_\omega & \left\langle c_{2\uparrow}c_{3\downarrow} \right\rangle_\omega & \left\langle c_{2\uparrow}c_{4\downarrow} \right\rangle_\omega \\ \left\langle c_{3\uparrow}c_{1\downarrow} \right\rangle_\omega & \left\langle c_{3\uparrow}c_{2\downarrow} \right\rangle_\omega & \left\langle c_{3\uparrow}c_{3\downarrow} \right\rangle_\omega & \left\langle c_{3\uparrow}c_{4\downarrow} \right\rangle_\omega \\ \left\langle c_{4\uparrow}c_{1\downarrow} \right\rangle_\omega & \left\langle c_{4\uparrow}c_{2\downarrow} \right\rangle_\omega & \left\langle c_{4\uparrow}c_{3\downarrow} \right\rangle_\omega & \left\langle c_{4\uparrow}c_{4\downarrow} \right\rangle_\omega \end{pmatrix}. \tag{2.39}$$

Methods to evaluate $\hat{\mathbf{G}}'(\omega)$ on classical and quantum computer are given in section 3.3.

Let's notice that in the $L_c = 2 \times 2$ cluster, 32 different correlation functions have to be evaluated. In the general case, the number of correlation functions simply scales as $4 \cdot L_c^2$, which is much smaller than the exponential scaling required for storing the full density matrix. See subsection2.5 and subsection 3.3.1 for the procedure to obtain these Green's functions.

At this point, the CPT potential in the reciprocal superlattice basis can also be defined as

$$\hat{\mathbf{V}}\left(\tilde{\mathbf{k}}\right) \equiv \hat{\mathbf{t}}\left(\tilde{\mathbf{k}}\right) - \hat{\mathbf{t}}', \tag{2.40}$$

where $\hat{\mathbf{t}}\left(\tilde{\mathbf{k}}\right)$ contains all the one-body terms of the bare lattice Γ (i.e. no interaction terms) of the Hamiltonian (2.1). For the example of the square lattice, this gives

$$\hat{\mathbf{t}}\left(\tilde{\mathbf{k}}\right) = \begin{pmatrix} \mathbf{A}\left(\tilde{\mathbf{k}}\right) & \mathbf{0} \\ \mathbf{0} & -\mathbf{A}\left(\tilde{\mathbf{k}}\right) \end{pmatrix}, \tag{2.41}$$

where

$$\mathbf{A}\left(\tilde{\mathbf{k}}\right) = \begin{pmatrix} -\mu & \epsilon\left(\tilde{k}_x\right) & \epsilon\left(\tilde{k}_y\right) & 0 \\ \epsilon^*\left(\tilde{k}_x\right) & -\mu & 0 & \epsilon\left(\tilde{k}_y\right) \\ \epsilon^*\left(\tilde{k}_y\right) & 0 & -\mu & \epsilon\left(\tilde{k}_x\right) \\ 0 & \epsilon^*\left(\tilde{k}_y\right) & \epsilon^*\left(\tilde{k}_x\right) & -\mu \end{pmatrix} \tag{2.42}$$

and the dispersion relation for the square lattice is

$$\epsilon\left(\tilde{k}\right) = -t\left(1 + e^{-2i\tilde{k}a}\right). \tag{2.43}$$

The $\hat{\mathbf{t}}'$ term in Eq. (2.40) contains all one-body terms of a cluster (2.22), including the variational terms. In the example,

$$\hat{\mathbf{t}}' = \begin{pmatrix} \mathbf{B} & \mathbf{C} \\ \mathbf{C} & \mathbf{D} \end{pmatrix}, \tag{2.44}$$

where

$$\mathbf{B} = \begin{pmatrix} -\mu' + M' & -t & -t & 0 \\ -t & -\mu' - M' & 0 & -t \\ -t & 0 & -\mu' - M' & -t \\ 0 & -t & -t & -\mu' + M' \end{pmatrix} \tag{2.45}$$

and

$$\mathbf{D} = \begin{pmatrix} \mu' + M' & t & t & 0 \\ t & \mu' - M' & 0 & t \\ t & 0 & \mu' - M' & t \\ 0 & t & t & \mu' + M' \end{pmatrix}. \tag{2.46}$$

The pairing part is given by

$$\mathbf{C} = \begin{pmatrix} \Delta' & \Delta'_d & -\Delta'_d & 0 \\ \Delta'_d & \Delta' & 0 & -\Delta'_d \\ -\Delta'_d & 0 & \Delta' & \Delta'_d \\ 0 & -\Delta'_d & \Delta'_d & \Delta' \end{pmatrix}. \tag{2.47}$$

2.4.2.4 *The lattice-perturbed Green's function*

Once the saddle point $\mathbf{t}_* = \begin{pmatrix} \mu'_* \\ \Delta'_* \\ \Delta'_{d*} \\ M'_* \end{pmatrix}$ of Eq. (2.32) is found, the function $\hat{\mathbf{G}}'\left(\omega, \mathbf{t}_*\right)$ and $\hat{\mathbf{V}}\left(\tilde{\mathbf{k}}, \mathbf{t}_*\right)$ are evaluated and the lattice-perturbed Green's function can be computed. From here the dimensionality of the matrices involved in the calculations scales only as the square of the number of orbitals and can be performed easily on a classical computer. The lattice-perturbed Green's function can be calculated to first order as

$$\begin{aligned} \hat{\mathcal{G}}\left(\tilde{\mathbf{k}}, \omega\right) &= \left(\hat{\mathbf{G}}'^{-1}\left(\omega\right) - \hat{\mathbf{V}}\left(\tilde{\mathbf{k}}\right)\right)^{-1} \\ &= \begin{pmatrix} \mathcal{G}'\left(\tilde{\mathbf{k}}, \omega\right) & \mathcal{F}'\left(\tilde{\mathbf{k}}, \omega\right) \\ \mathcal{F}'^{\dagger}\left(\tilde{\mathbf{k}}, \omega\right) & -\mathcal{G}'\left(\tilde{\mathbf{k}}, -\omega\right) \end{pmatrix}. \end{aligned} \tag{2.48}$$

Note that the $\mathcal{G}$ and $\mathcal{F}$ matrices have dimension $L_c \times L_c$. At this point the problem is solved and many observable quantities can be computed efficiently [20].

2.4.3 *Calculation of observables*

Based on [87], this subsection contains examples of observables useful in explaining the result of experiments and landmark properties of the FHM.

The average particle density is

$$n = \langle n_{i\sigma} \rangle = \frac{1}{NL_c} \oint_C \frac{dz}{2\pi i} \sum_{\tilde{\mathbf{k}}} \sum_{i=1}^{L_c} \mathcal{G}_{ii}\left(\tilde{\mathbf{k}}, z\right) \tag{2.49}$$

and must agree with the value given by (2.25). The chemical potential μ can be scanned until a desired value of n is found. For superconducting problem in the FHM, it is useful to fix the chemical potential μ such that the lattice is maintained at quarter filling $n = 0.25$. The superconducting gap is given by

$$\Delta = \left\langle c_{i\uparrow} c_{j\downarrow} \right\rangle = \frac{1}{NL_c} \oint_C \frac{dz}{2\pi i} \sum_{\tilde{\mathbf{k}}} \sum_{i=1}^{L_c} \mathcal{F}_{ii}\left(\tilde{\mathbf{k}}, z\right). \tag{2.50}$$

To recover the Green's functions of the full lattice Γ, the "clustering" (which is a unitary transformation) is undone and, taking into account the artificial translational symmetry breaking of the lattice, the single-particle and anomalous CPT Green's functions are recovered in the lattice reciprocal space

$$\begin{aligned}\mathcal{G}_{\text{cpt}}\left(\mathbf{k},\omega\right) &= \tfrac{1}{L_c}\textstyle\sum_{i,j=1}^{L_c}\mathcal{G}_{ij}\left(\mathbf{k},\omega\right)e^{-i\mathbf{k}\cdot\left(\mathbf{r}_i-\mathbf{r}_j\right)} \\ \mathcal{F}_{\text{cpt}}\left(\mathbf{k},\omega\right) &= \tfrac{1}{L_c}\textstyle\sum_{i,j=1}^{L_c}\mathcal{F}_{ij}\left(\mathbf{k},\omega\right)e^{-i\mathbf{k}\cdot\left(\mathbf{r}_i-\mathbf{r}_j\right)}.\end{aligned} \tag{2.51}$$

From these quantities, the single-particle quasi-particle spectrum and the Bogoliubov quasi-particle spectrum can be evaluated as

$$\begin{aligned}A\left(\mathbf{k},\omega\right) &= -\tfrac{1}{\pi}\lim_{\eta\to0^+}\operatorname{Im}\mathcal{G}_{\text{cpt}}\left(\mathbf{k},\omega+i\eta\right) \\ F\left(\mathbf{k},\omega\right) &= -\tfrac{1}{\pi}\lim_{\eta\to0^+}\operatorname{Im}\mathcal{F}_{\text{cpt}}\left(\mathbf{k},\omega+i\eta\right),\end{aligned} \tag{2.52}$$

from which the density of states is found to be

$$N\left(\omega\right)=\frac{1}{N}\sum_{\mathbf{k}}A\left(\mathbf{k},\omega\right). \tag{2.53}$$

The Fermion momentum distribution and the condensation amplitude momentum distribution are respectively given by

$$\begin{aligned}N\left(\mathbf{k}\right) &= \oint_C \tfrac{dz}{2\pi i}\mathcal{G}_{\text{cpt}}\left(\mathbf{k},z\right) \\ F\left(\mathbf{k}\right) &= \oint_C \tfrac{dz}{2\pi i}\mathcal{F}_{\text{cpt}}\left(\mathbf{k},z\right).\end{aligned} \tag{2.54}$$

For the case of a lattice with superconductivity, an interesting observable is the pair coherence length in real and reciprocal space given by

$$\xi^2=\frac{\sum_{\mathbf{r}}\mathbf{r}^2\left|F\left(\mathbf{r}\right)\right|^2}{\sum_{\mathbf{r}}\left|F\left(\mathbf{r}\right)\right|^2}=\frac{\sum_{\mathbf{k}}\left|\nabla_{\mathbf{k}}F\left(\mathbf{k}\right)\right|^2}{\sum_{\mathbf{k}}\left|F\left(\mathbf{k}\right)\right|^2}. \tag{2.55}$$

Depending on the problem, more observables can be computed with similar methods. Note also that the contour integrals map to the following form in the real time domain

$$\oint_C\frac{dz}{2\pi i}\mathcal{G}^R\left(z\right)\to\int_{-\infty}^{\infty}d\omega f\left(\omega\right)\mathcal{G}^R\left(\omega\right) \tag{2.56}$$

in the case where the retarded part of the Green's function is used to compute the integral. The Fermi function has the usual form $f\left(\omega\right)=\frac{1}{1+e^{\frac{\mu-\omega}{T}}}$. The self-energy variational approach has been outlined and the method which starts with a Hubbard-like description of the microscopic details of a given solid and computes its thermodynamic properties in a systematic way is complete. The next section reviews how the eigenvalue problem (2.35) is typically solved on classical computers and introduces the quantum subroutine.

2.4.4 *Ozaki summation*

The typical Matsubara summations [20] require tens of thousand of imaginary points $i\omega_p$ before convergence can be reached. The Ozaki summation method based on the continued fraction representation of the Fermi-Dirac function reaches the same accuracy in less than a few hundred points [86]. It is therefore advisable to compute the observables of many-electron systems using the following expansion of the Fermi-Dirac function $f(\omega)$:

$$\begin{aligned} &\tfrac{1}{1+e^{\omega}} \\ =\;& \tfrac{1}{2} - \tfrac{\omega}{4}\left(\cfrac{1}{1+\cfrac{\left(\frac{\omega}{2}\right)^2}{3+\cfrac{\left(\frac{\omega}{2}\right)^2}{\cfrac{\cdots}{(4M-1)+\ddots}}}}\right) \\ \approx\;& \tfrac{1}{2} + \textstyle\sum_{p=1}^{M} \frac{R_p}{\omega - iz_p} + \sum_{p=1}^{M} \frac{R_p}{\omega + iz_p} \\ =\;& \tfrac{1}{2} - \tfrac{\omega}{4}\left\{\left(i\omega B - A\right)^{-1}\right\}_{11} \end{aligned} \tag{2.57}$$

The resolvent equation is solved for R_p and the poles z_p. The density matrix ρ can be computed from the weighted sum

$$\begin{aligned} &\rho \\ =\;& \lim_{\eta\to 0^+} \lim_{R\to\infty} \mathrm{Im}\left[-\tfrac{2}{\pi}\int_{-R+\mu}^{R+\mu} dE\, G\left(E+i\eta\right) f\left(E\right)\right] \\ =\;& \mu^{(0)} - \mathrm{Re}\left[\tfrac{4}{\beta}\textstyle\sum_{p=1}^{M} G\left(\mu + i\frac{z_p}{\beta}\right) R_p\right] \end{aligned} \tag{2.58}$$

where the zeroth-order moment is given by

$$\mu^{(0)} = \lim_{R\to\infty} iRG\left(iR\right). \tag{2.59}$$

In Matsubara summations, $R_p = 1$ for all points. We chose $M = 300$ and $R = 10^{10}$ for the numerical calculations. Numerical calculations at arbitrary finite temperature case can be handled by using the density matrix formalism and by replacing the contour integrals by Ozaki summations. In the literature, zero temperature calculations usually proceed with a Lanczos diagonalization followed by integration along the imaginary energy axis [56].

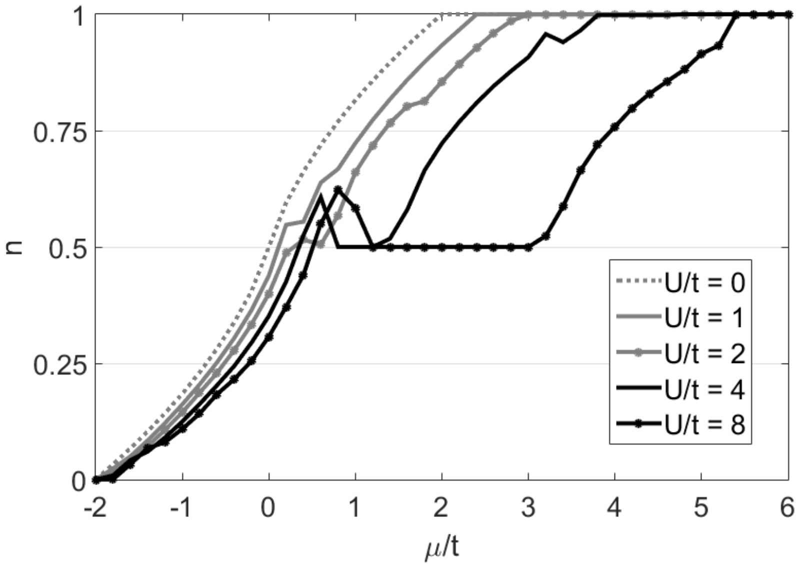

Figure 2.7: Orbital filling factor n as a function of the chemical potential μ calculated with the CPT.

2.4.5 *Cluster perturbation theory*

The CPT is embodied in Eq. 2.48. It corresponds to the specific case of the VCA with trivial values for the variational parameters. As such, it cannot account for broken symmetries in correlated systems [32]. In figure 2.7, we show the orbital filling factor n as a function of the chemical potential for several interaction energies U. As a rule of thumb, half-filling $n = \frac{1}{2}$ is obtained at $\mu \approx \frac{U}{4}$ (from the particle-hole transformation on a bipartite lattice, this should be $\mu \approx \frac{U}{2}$). The function n is not monotonically increasing with μ and is therefore not thermodynamically consistent.This is a consequence of ill-defined degrees of freedom in the single-particle parameter space. However, this can used as an initial point for variational calculations.

In figure 2.8, we reproduced the figure found in [32, 88] showing the ground state $E_0 = \Omega + 2\mu n$ of a single impurity of the FHM at half-filling calculated from the CPT method (without variational parameters). By considering variational parameters of the cluster self-energy, the ground state energy can be lowered for $U \neq 0$.

When non-trivial variational parameters are fixed, CPT can be used to compute ARPES spectra and other quantities of interest. In figure 2.9, we show the exact spectral density $A(k, \omega)$ for the tight-binding model $U = 0$ and the CPT spectral density at $U = 8$ at half-filling. A large gap opening along the X direction is typical of the Mott insulating phenomenon. Since we are interested in calculating phase diagrams such as the one shown in figure 1.8 and the CPT cannot take into account broken symmetries, variational terms must be taken into account.

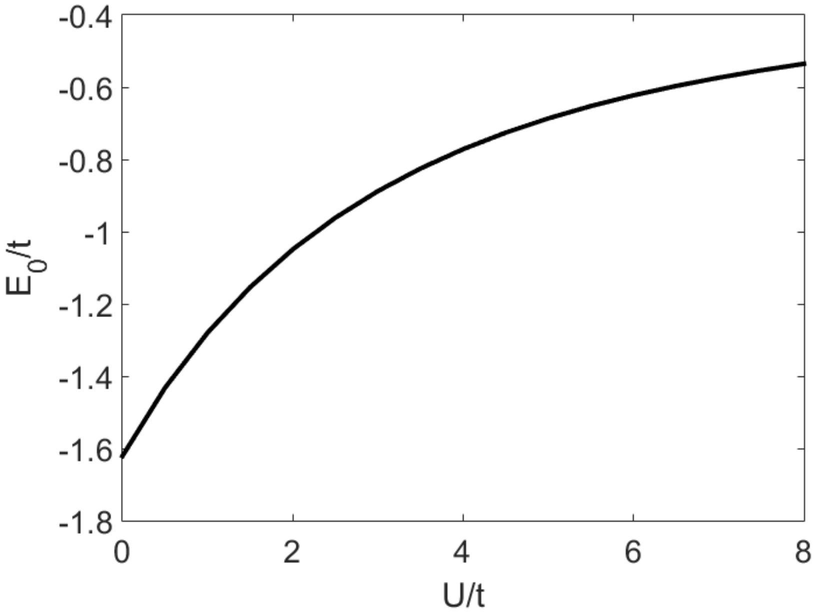

Figure 2.8: Ground state energy E_0 of an impurity as a function of the interaction energy U calculated from the CPT. It is exact at $U = 0$ and represent an upper bound for $U > 0$. The zero-temperature calculations is approximated by setting the temperature at $T = \frac{t}{1000}$. This reproduces the results obtained in [88].

2.4.6 *Potthoff functional at finite temperature*

Here we show the typical landscape of the Potthoff functional (2.34) for anti-ferromagnetic (4.12) and superconducting (4.17) variational parameters. The cluster chemical potential (4.11) is also kept as a variational parameter to enforce thermodynamical consistency. The interaction strength is in the strong coupling regime $U = 8$, a typical parameter in the study of cuprate superconductivity. The Potthoff functional and the norm of its gradient at two different temperatures are shown in figure 2.10. The stationary point is found in the region where $n = \frac{1}{2}$ and the norm of the gradient is minimal. In the case where positive and negative values are possible, the positive one is chosen. The VCA lowers the energy found in figure 2.8 at low temperature by allowing an anti-ferromagnetic order such as the one shown in figure 2.2. The ordering disappears at high temperature.

Figure 2.11 shows the Potthoff functional and the norm of its gradient when considering a d-wave superconducting order parameter at low temperature. The starting point corresponds to the CPT calculation which gives a filling factor $n = \frac{1}{2}$. A more complete calculation would take the value consistent with $\langle n \rangle = -\frac{d\Omega_t}{d\mu}$ and have an increased precision for smaller Δ'_d. We find a finite value of the d-wave parameter at half-filling which is consistent with other works which do not include a next-nearest-neighbor hopping term [32, 65]. How-

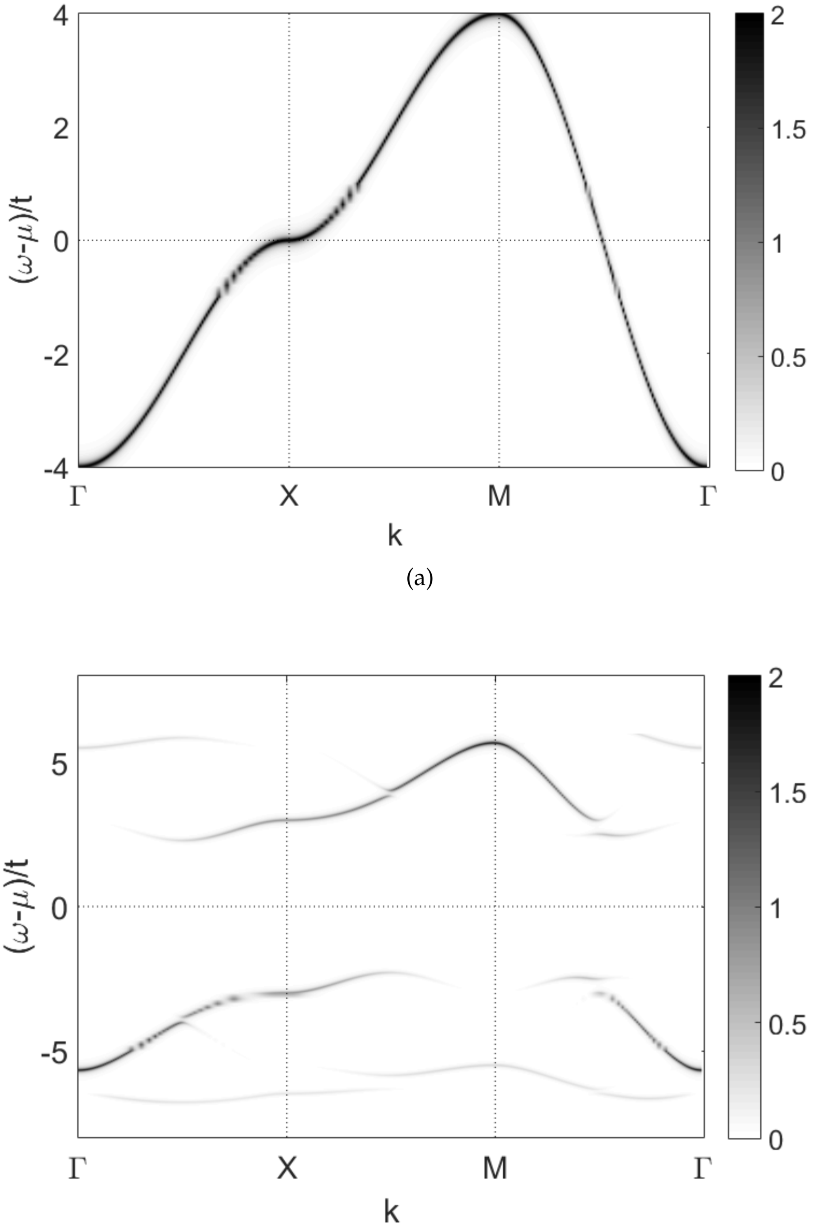

(a)

(b)

Figure 2.9: Spectral density $A(k,\omega)$ at $U = 0$ and $\mu = 0$ in (a) and $U = 8$ and $\mu = 2$ in (b). The CPT without variational parameters was used with a broadening $\eta/t = 0.05$.

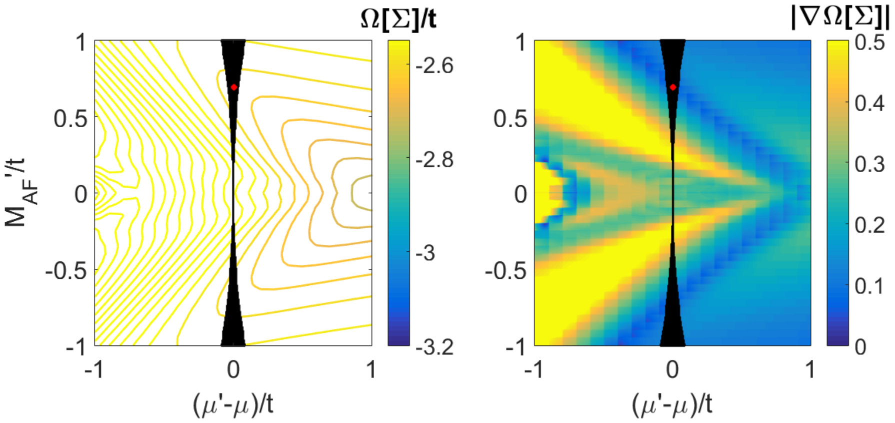

(a) $\frac{T}{t} = 0.1$

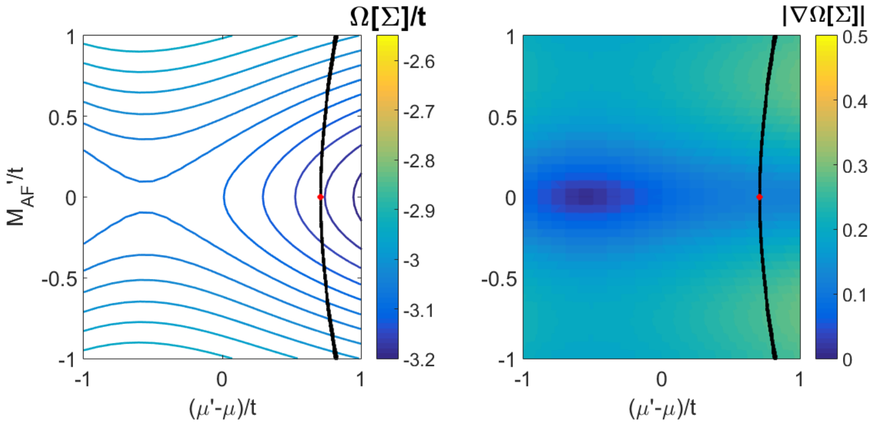

(b) $\frac{T}{t} = 1$

Figure 2.10: Anti-ferromagnetism in the FHM at low and high temperature. The interaction is $\frac{U}{t} = 8$ and half-filling is obtained at $\frac{\mu}{t} = 2$. In the figure, the black region corresponds to half-filling $n = \frac{1}{2}$. The red dot corresponds to the minimum of the gradient of Potthoff functional in the half-filled lattice. In (a) the temperature $\frac{T}{t} = 10^{-1}$, the saddle-point is located at $\mu' = \mu$ and $\frac{M'_{AF}}{t} \approx 0.69$ and the energy of the ground state $\frac{E_0}{t} = -0.61$ which is lower than the one found in figure 2.8. In (b) the temperature $\frac{T}{t} = 1$, the saddle-point in the half-filled region is located at $\frac{\mu' - \mu}{t} \approx 0.71$ and $M'_{AF} = 0$.

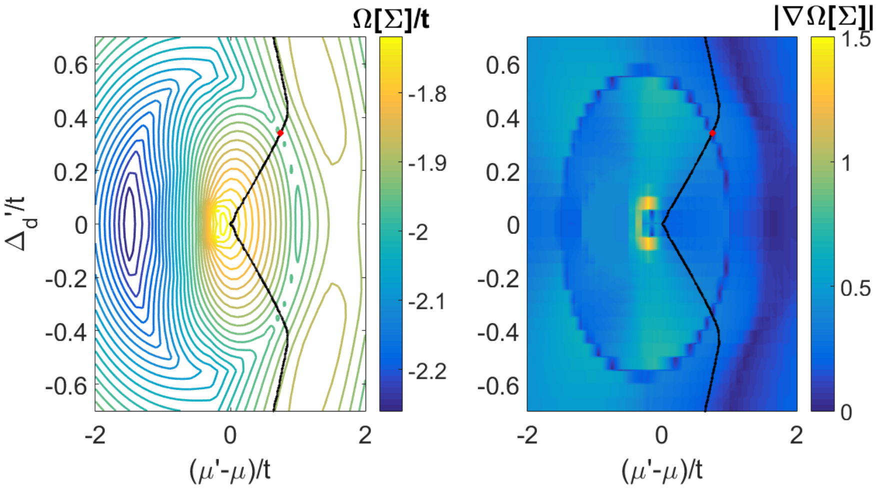

Figure 2.11: The interaction is $\frac{U}{t} = 8$ and the chemical potential is chosen to be $\frac{\mu}{t} = 2$. The black region corresponds to half-filling $n = \frac{1}{2}$ which goes through the center $\mu' = \mu$ and $\Delta_d' = 0$. The temperature is set at $\frac{T}{t} = 10^{-3}$. The red dot at $\frac{\mu' - \mu}{t} \approx 0.74$ and $\frac{\Delta_d'}{t} \approx 0.33$ corresponds to the minimum of the gradient of Potthoff functional.

ever we find a superconducting parameter which is an order of magnitude larger than the ones previously found in the literature. The main difference between the methods is the use of the density matrix formalism and Ozaki summation technique in the present work.

Verifying whether the FHM is sufficient to describe the phenomenon of superconductivity in cuprate is still an open question. Increasing the size of clusters to increase the accuracy of the simulation is a computationally expensive task. The scaling of classical memory resources required is actually exponential in the number of spin orbitals modeled. Therefore it may be advisable to use the help of quantum processors to proceed with larger and more complex calculations.

2.5 THE METHOD ON A CLASSICAL COMPUTER

The resource intensive part of the numerical variation solver is the computation of the energy-dependent Green's function of the cluster $\hat{\mathbf{G}}'(\omega, \mathbf{t})$. On a classical computer, the memory used to store the description of the state of the system scales exponentially in system size.

Typically, the Hamiltonian (2.22) is encoded in the occupation basis (2.36) and the Schrödinger equation (2.35) is solved explicitly using an appropriate numerical diagonalization method. As shown in table 2.1, the memory usage scales exponentially with system size and diagonalization typically scales as $O\left(L_c^3\right)$ in the number of arithmetic operation required. When successful, a set of eigenvalues $\{E_n\}$ and

Number of orbitals	Memory required
3	1 KB
8	1 MB
13	1 GB
18	1 TB
23	1 PB

Table 2.1: Order of magnitude estimation of the classical memory required to store the full finite temperature density matrix of a cluster with a given number of irreducible orbitals for a general cluster Hamiltonian. It is assumed that each matrix element is stored as a complex double-precision number (16 bytes/element) and no optimization is used.

associated eigenstates $\{|\phi_n\rangle\}$ are obtained. If the cluster has L_c sites with 2 electrons each (spin up and down), then there are 4^{L_c} eigenstates. The rest of the procedure is the following:

1. Write $\omega_{mn} = E_n - E_m$.

2. Write the occupation probabilities $P_{mn} = \frac{e^{-\beta E_n}+e^{-\beta E_m}}{Z}$. Note that $\beta \equiv T^{-1}$ is the inverse temperature and $Z = \mathrm{Tr}\left(e^{-\beta\mathcal{H}'}\right)$ is the partition function.

3. Define the electron-like and hole-like amplitude $Q^{(e\uparrow)}_{imn} = \langle\phi_m|\, c_{i\uparrow}\, |\phi_n\rangle$ and $Q^{(h\downarrow)}_{imn} = \langle\phi_m|\, c^{\dagger}_{i\downarrow}\, |\phi_n\rangle$.

4. Vectorize the $m, n \longrightarrow r$ indices to obtain the matrices $\hat{E}_{rs} = \delta_{rs}\omega_r$ and $\hat{\Pi}_{rs} = \delta_{rs}P_r$. The amplitude matrices then take the form

$$\hat{\mathbf{Q}} = \begin{pmatrix} Q^{(e\uparrow)}_{1r} \\ \vdots \\ Q^{(e\uparrow)}_{L_c r} \\ Q^{(h\downarrow)}_{1r} \\ \vdots \\ Q^{(h\downarrow)}_{L_c r} \end{pmatrix} \tag{2.60}$$

   and can be recast as $\hat{\mathbf{Q}}' = \hat{\mathbf{Q}}\sqrt{\hat{\Pi}}$ at non-zero temperature. It is also useful to define and compute $\hat{\mathbf{g}}(\omega) = \frac{\hat{\mathbf{1}}}{\omega - \hat{\mathbf{E}}}$. It an be noted that $\hat{\mathbf{Q}}$ is a $2L_c \times 16^{L_c}$ matrix which scales exponentially in memory with the size of the system being studied.

5. Then compute (2.37) as $\hat{\mathbf{G}}'(\omega) = \hat{\mathbf{Q}}'\hat{\mathbf{g}}(\omega)\,\hat{\mathbf{Q}}'^{\dagger}$. This is the most time-consuming step on a classical computer, especially at non-zero temperature.

6. The grand potential functional (2.34) and the lattice-perturbed Green's function (2.48) can then be evaluated to respectively solve the saddle-point problem and compute observables.

In the following quantum method, these steps will be bypassed and $\hat{\mathbf{G}}'(\omega)$ obtained directly from the variational parameters.

Part II

THE QUANTUM VARIATIONAL CLUSTER APPROACH ON QUANTUM SIMULATORS

Nature isn't classical, dammit, and if you want to make a simulation of nature, you'd better make it quantum mechanical, and by golly it's a wonderful problem, because it doesn't look so easy.
— Richard Feynman [*89*]

3

SIMULATING THE FERMI-HUBBARD MODEL ON A QUANTUM COMPUTER

3.1 OVERVIEW

As seen in chapter 2, simulating a small cluster with a handful of electrons (or orbitals) is a difficult task for classical computers since the matrices involved in the computation scale exponentially in size with respect to the number of electronic orbitals. The quantity of information involved in the precise numerical treatment of large strongly correlated electronic systems quickly reaches magnitudes where no reasonable classical memory technology is sufficient to store it all. Therefore, being given access to a large controllable Hilbert space in a quantum computer offers the possibility of simulating electronic systems at the microscopic level with a greater complexity and accuracy than the ones accessible to classical computers [89].

This work is inspired from recently developed approaches in quantum simulations such as the simulation of spin systems [90, 91], fermionic systems and quantum chemistry [92–95] and boson sampling to extract vibronic spectra [96]. In general, it happens that the occupation state of an electronic orbital can be efficiently represented by one qubit on a quantum computer through the Jordan-Wigner transformation (JWT). The memory bottleneck in numerically representing the many-body wave function is overcome by making sure that it is never measured and stored on a classical memory at any point during the simulation. In the VCA, the quantities that need to be extracted from the wave function are the intra-cluster single-particle correlation functions whose number scales quadratically with the number of orbitals in a given cluster. On the practical side, it is not yet known how the computing power of quantum processing devices will scale in the future, but machines with a fews tens or hundreds of qubits could already be very useful to run quantum subroutines as part of larger classical simulation algorithms. This proposed method could open a practical way to model and engineer the electronic behavior of strongly-correlated materials with intricate crystalline structures in a unified and consistent manner. Furthermore the underlying SFT is very general and not restricted to the class of FHMs, formulations for extended interactions [85], disordered systems [97] and non-equilibrium dynamics [98] have already been developed. Similar schemes to simulate spin systems [99], the Bose-Hubbard model [100] or more exotic fields in lattice gauge theories [101, 102] can likely be constructed in a similar fashion.

After reviewing some basics of quantum computing in section 3.2, a memory efficient quantum subroutine to introduced in section 3.3.1. The procedure to measure the Green's function of the cluster is described in section 3.3.2. Appendix A presents numerical results where the quantum procedure to compute a cluster's Green's function is shown to be equivalent to traditional solution methods. In appendix A.4, details of the initial Gibbs state preparation are given for a specific algorithm.

3.2 QUANTUM COMPUTING

In 1982, Richard Feynman introduced the concept of quantum simulators for the purpose of simulating molecular processes which are beyond the reach of classical computers [89]. Since then, it is believed that general purpose quantum computers could solve some problems faster than their classical counterparts [103]. Problems that may benefit from quantum speed-up appear in the simulation of quantum chemistry and materials [104], in number theory such as the factoring problem [105] and in artificial intelligence. Here we quickly review some basic aspects of quantum computing and introduce some notation used in the following sections.

3.2.1 *Fundamentals of quantum computing*

The main technical challenges to building a practical quantum computer are summarized by the five DiVincenzo criteria [60]

1. *State initialization*. In the computational basis, a pure state $|\psi\rangle = \frac{\alpha|0\rangle+\beta|1\rangle}{\sqrt{|\alpha|^2+|\beta|^2}}$ is described by a linear superposition of a two-state system where α and β can be any complex numbers. Operating a quantum computer requires a "reset" operation which erases the quantum information of the state and returns the initialized qubit in the $|0\rangle$ state. In general, this process is irreversible.

2. *Addressing*. A quantum computer is composed of many qubit units which can be separately addressed. Distinguishable and uncorrelated units are described with the tensor product notation. For example, the state of two separable qubits can generally be represented in the form $\rho = \rho_1 \otimes \rho_2$. We also define a convenient tensor power notation

$$^{\otimes k} \equiv \begin{cases} 1 & k = 0 \\ \sigma & k = 1\,, \\ \sigma \otimes {}^{\otimes k-1} & k > 1 \end{cases} \tag{3.1}$$

where σ represent any 1-qubit operator.

3. *Universal quantum control.* A quantum computation U is a unitary transformation which can be decomposed in M discrete quantum gates such that an initialized n-qubit state is evolved into an "answer" state $|\psi_{\text{ans}}\rangle = U|0\rangle^{\otimes n} = U_M U_{M-1} \ldots U_1 |0\rangle^{\otimes n}$. In general, quantum computation can be done using only single-qubit quantum gates (see section 3.2.2) and two-qubit entangling operations, namely unitary quantum operations which produce non-separable two-qubit states.

4. *Measurements.* The state of an isolated subsystem A out of a larger system $A \oplus B$ is given by the partial trace $\rho_A = \mathrm{Tr}_B(\rho_{A\oplus B})$. If A is a qubit subsystem, the probability that $|0\rangle$ is measured is given by $P(\mathcal{M} = 0) = \langle 0|\rho_A|0\rangle$ while the probability that $|1\rangle$ is measured is given by $P(\mathcal{M} = 1) = \langle 1|\rho_A|1\rangle$. After a measurement, the state has "collapsed" to the measured state.

5. *Quantum memory.* Quantum bits are very fragile units of information. Any uncontrolled interaction with the environment will tend to erase useful quantum information, this is the phenomenon of decoherence. The characteristic times used to quantify the decoherence process is the energy relaxation time T_1 (where energy is lost to the environment) and the dephasing time T_ϕ (related to the fluctuation of energy levels from interactions with uncontrolled degrees of freedom). Typically, quantum algorithms require a "long" but finite time to run, hence coherence time is a valuable quantum resource intrinsic to quantum memories. A logical (or fault-tolerant) qubit is a quantum memory with arbitrarily long coherence time. Quantum error correction methods can in principle be used to increase the lifetime of qubits.

3.2.2 *Elementary quantum gates*

In table (3.1), we define the notation and the matrix representation on the computational basis of useful single qubits gates. Notably, the Hadamard gate $\mathbb{H}$ is often used to prepare a register in the superposition of all possible states

$$\mathbb{H}^{\otimes n}|0\rangle^{\otimes n} = \frac{1}{2^{\frac{n}{2}}}\sum_{k=0}^{2^n-1}|k\rangle\,, \tag{3.2}$$

where k is the appropriate binary representation. The Pauli operators $\sigma \in \{\sigma_x, \sigma_y, \sigma_z\}$ can also be viewed as generators of single-qubit rotation with angle θ such that

$$\begin{aligned} R_\sigma^\theta &\equiv e^{\frac{i\theta\sigma}{2}} \\ &= \mathbb{I}\cos\left(\tfrac{\theta}{2}\right) + i\sigma\sin\left(\tfrac{\theta}{2}\right). \end{aligned} \tag{3.3}$$

Gate	Matrix representation
$-\boxed{\mathbb{I}}-$	$\begin{pmatrix} 1 & 0 \\ 0 & 1 \end{pmatrix}$
$-\boxed{\sigma_x}-$	$\begin{pmatrix} 0 & 1 \\ 1 & 0 \end{pmatrix}$
$-\boxed{\sigma_y}-$	$\begin{pmatrix} 0 & -i \\ i & 0 \end{pmatrix}$
$-\boxed{\sigma_z}-$	$\begin{pmatrix} 1 & 0 \\ 0 & -1 \end{pmatrix}$
$-\boxed{\mathbb{H}}-$	$\frac{1}{\sqrt{2}}\begin{pmatrix} 1 & 1 \\ 1 & -1 \end{pmatrix}$
$-\boxed{\mathbb{J}}-$	$\frac{1}{\sqrt{2}}\begin{pmatrix} 1 & -i \\ 1 & i \end{pmatrix}$
$-\boxed{\mathbb{S}}-$	$\begin{pmatrix} 1 & 0 \\ 0 & i \end{pmatrix}$
$-\boxed{\mathbb{T}}-$	$\begin{pmatrix} 1 & 0 \\ 0 & e^{i\frac{\pi}{4}} \end{pmatrix}$
$-\boxed{\mathbb{Q}}-$	$\begin{pmatrix} 1 & 0 \\ 0 & e^{i\frac{\pi}{8}} \end{pmatrix}$

Table 3.1: Circuit and matrix representation of useful single-qubit gates.

Name	Gate	Matrix representation
CNOT	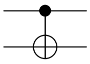	$\begin{pmatrix} 1 & 0 & 0 & 0 \\ 0 & 1 & 0 & 0 \\ 0 & 0 & 0 & 1 \\ 0 & 0 & 1 & 0 \end{pmatrix}$
SWAP	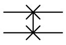	$\begin{pmatrix} 1 & 0 & 0 & 0 \\ 0 & 0 & 1 & 0 \\ 0 & 1 & 0 & 0 \\ 0 & 0 & 0 & 1 \end{pmatrix}$
c-U	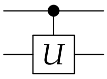	$\begin{pmatrix} 1 & 0 & 0 & 0 \\ 0 & 1 & 0 & 0 \\ 0 & 0 & \alpha & \beta \\ 0 & 0 & \gamma & \delta \end{pmatrix}$

Table 3.2: Circuit and matrix representation of useful two-qubit gates.

Elementary two-qubit gates are shown in table (3.2). The conditional-NOT (CNOT) is an entangling gate which is dependent on the state of the first qubit. A conditional-CNOT is also called a Toffoli gate, it can be used in classical circuits to define arbitrary reversible logical circuits. An arbitrary conditional unitary operation can be formally written as

$$c - U \equiv |0\rangle \langle 0| \otimes \mathbb{I} + |1\rangle \langle 1| \otimes U. \tag{3.4}$$

As a fundamental rule of quantum information, an unknown quantum state $|\psi\rangle$ cannot be copied. However, two quantum states can be exchanged between registers by using the SWAP operation such that

$$|\psi_B\rangle \otimes |\psi_A\rangle = \text{SWAP}\left(|\psi_A\rangle \otimes |\psi_B\rangle\right). \tag{3.5}$$

A conditional-SWAP is also known as a Fredkin gate.

3.2.3 *The quantum Fourier transformation*

There are two main heuristics for quantum algorithms. First, one can use one qubit as a probe to sample the trace of operators in an "analog" fashion by repeating a set of experiments [106]. Second, one can prepare a large state superposition (3.2), conditionally encode some bits of information in the phase of each state and map this phase information back into the amplitude of each state to finally measure a digital answer. This mapping from amplitude to phase information is the quantum Fourier transform (QFT) [103]. The register that the

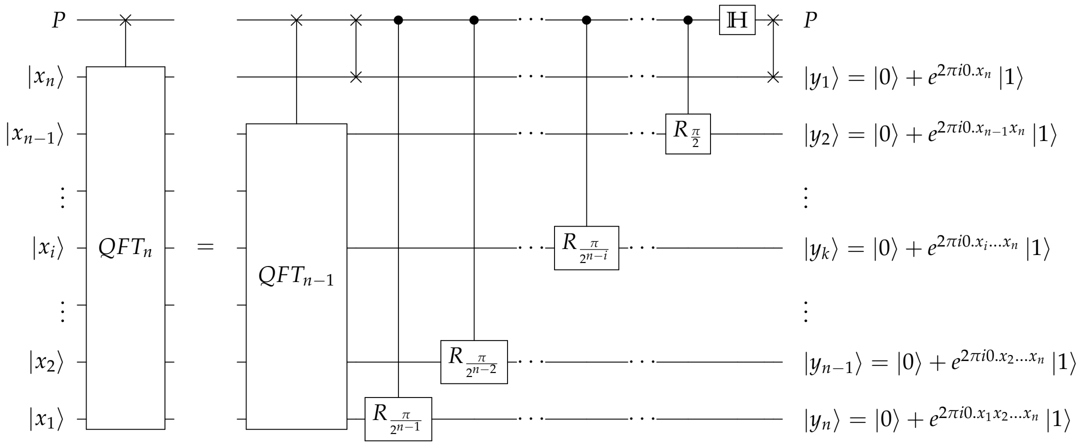
P
$|x_n\rangle$
$|x_{n-1}\rangle$
$|x_i\rangle$
$|x_2\rangle$
$|x_1\rangle$
QFT_n
=
QFT_{n-1}
$R_{\frac{\pi}{2^{n-1}}}$
$R_{\frac{\pi}{2^{n-2}}}$
$R_{\frac{\pi}{2^{n-i}}}$
$R_{\frac{\pi}{2}}$
$\mathbb{H}$
P
$|y_1\rangle = |0\rangle + e^{2\pi i 0.x_n}|1\rangle$
$|y_2\rangle = |0\rangle + e^{2\pi i 0.x_{n-1}x_n}|1\rangle$
$|y_k\rangle = |0\rangle + e^{2\pi i 0.x_i \ldots x_n}|1\rangle$
$|y_{n-1}\rangle = |0\rangle + e^{2\pi i 0.x_2 \ldots x_n}|1\rangle$
$|y_n\rangle = |0\rangle + e^{2\pi i 0.x_1 x_2 \ldots x_n}|1\rangle$

Figure 3.1: Recursive gate decomposition of the QFT. It uses $2(n-1)$ SWAPs and an ancilla qubit P. This variant can be implemented physically by having all qubits couple to the middle qubit P.

QFT operates on has n qubits and the corresponding Hilbert space has dimension $\mathcal{N} = 2^n$. The QFT can be defined as

$$QFT\,|j\rangle \equiv \frac{1}{\sqrt{\mathcal{N}}} \sum_{k=0}^{\mathcal{N}-1} e^{\frac{2\pi i jk}{\mathcal{N}}}\,|k\rangle \tag{3.6}$$

and it is a unitary operation such that

$$QFT^{\dagger} \cdot QFT = \mathbb{I}. \tag{3.7}$$

A convenient recursive gate decomposition is shown in figure 3.1. The circuit can be implemented in at most $\Theta\left(n^2\right)$ quantum gates while the classical fast Fourier transform requires $\Theta\left(n2^n\right)$ operations.

3.2.4 *Phase estimation*

Phase estimation is an important primitive for quantum simulations and factoring [103]. The gate decomposition of the phase estimation algorithm is shown in figure 3.2. The input has r qubits in the $|0\rangle$ state and an eigenstate $|\psi_k\rangle$ of some Hamiltonian $\mathcal{H}$ such that $\mathcal{H}\,|\psi_k\rangle = E_k\,|\psi_k\rangle$. Assuming one has access to a black box $U = e^{-i\mathcal{H}\tau_0}$ that can simulate the evolution of the Hamiltonian for some time step (or reference energy) $\tau_0 = E_0^{-1}$, the eigenstate remains invariant

$$U\,|\psi_k\rangle = e^{-i\varphi_k}\,|\psi_k\rangle \tag{3.8}$$

up to a phase $\varphi_k = \frac{E_k}{E_0}$. The output of the algorithm yields an approximation $\tilde{\varphi}_k$ of φ_k. In order to obtain an accuracy of n bits with a probability of success $\geq 1-\epsilon$, the number of qubits r required is

$$r \geq n + \left\lceil \log\left(2 + \frac{1}{2\epsilon}\right)\right\rceil . \tag{3.9}$$

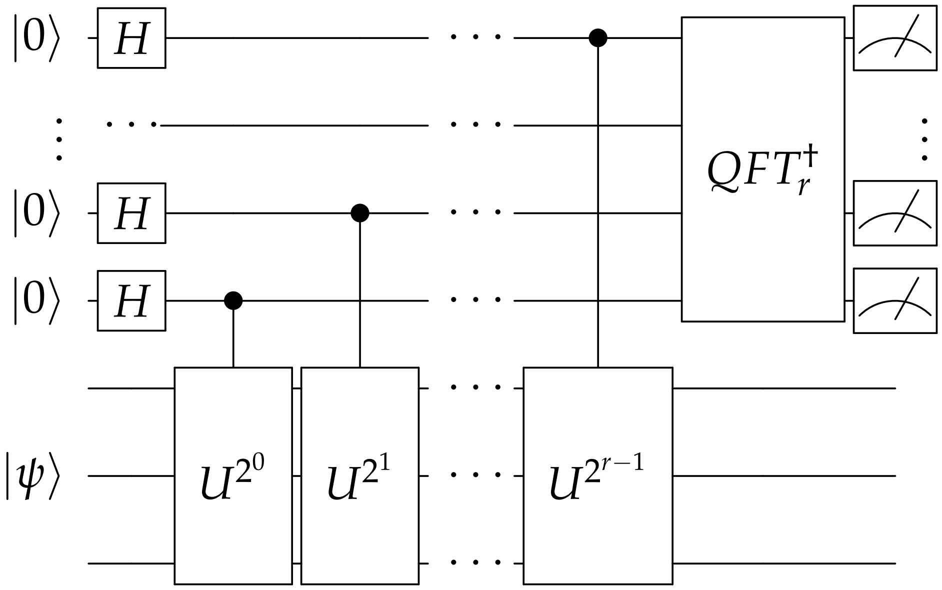

Figure 3.2: The circuit decomposition of the phase estimation algorithm.

3.2.5 *The Jordan-Wigner transformation*

Qubits in quantum computers are distinguishable objects, while electrons are not. In order to map the fermionic creation and annihilation operators of the Hamiltonian to the computational basis, a JWT [107] can be used. If there are $n = 2L_c$ electrons, then the Jordan-Wigner transformed creation operators are given by

$$\begin{aligned} c^\dagger_{i\uparrow} &= \mathbb{I}^{\otimes 2(L_c-i)+1} \otimes \sigma_+ \otimes \sigma_z^{\otimes 2(i-1)} \\ c^\dagger_{i\downarrow} &= \mathbb{I}^{\otimes 2(L_c-i)} \otimes \sigma_+ \otimes \sigma_z^{\otimes 2i-1} \end{aligned} \quad . \tag{3.10}$$

This ensures that the fermionic anticommutation relation $\left\{c_{i\sigma}, c^\dagger_{j\sigma'}\right\} = \delta_{ij}\delta_{\sigma\sigma'}$ and $\left\{c_{i\sigma}, c_{j\sigma'}\right\} = \left\{c^\dagger_{i\sigma}, c^\dagger_{j\sigma'}\right\} = 0$ are enforced. In this notation, $\sigma_+ \equiv \frac{(\sigma_x + i\sigma_y)}{2}$, $\sigma_- \equiv \sigma_+^\dagger$ and $\sigma_z \equiv 2\sigma_n - \mathbb{I}$, where $\sigma_n \equiv \sigma_+\sigma_-$. The relations $\sigma_+\sigma_z = \sigma_+ = -\sigma_z\sigma_+$ and $\sigma_z\sigma_- = \sigma_- = -\sigma_-\sigma_z$ can also be used. In this scheme, each spin orbital $i \uparrow$ is followed in tensored space by the spin orbital $i \downarrow$. This ordering is convenient to simplify the interaction terms of FHM clusters as the Coulomb interaction is confined to each site. As there is freedom in the ordering of the indices, for other models a good ordering should be chosen based on the symmetries of the simulated Hamiltonians. Note that for finite clusters the JWT is in general independent of the dimensionality of the system.

3.3 SOLVING THE EIGENVALUE PROBLEM ON A QUANTUM COMPUTER

Solving the eigenvalue problem (2.35) for a large number of electrons is exponentially costly in memory as the number of orbitals increases. This section is divided the following way. First the classical eigenvalue solver for the Green's function is described. Then the JWT is used to map the cluster Hamiltonian to a quantum register. A method to generate initial Gibbs states in a quantum computer is reviewed and finally a procedure to extract the Green's function out of the Gibbs state is explained. The full quantum procedure is shown to be efficient in quantum memory resources.

3.3.1 *The method on a quantum computer*

Computing the Green's function of the cluster $\hat{\mathbf{G}}'(\omega, \mathbf{t})$ on a quantum computer is possible in a hybrid analog-digital simulator. The first step generates a Gibbs state $\rho_{\text{Gibbs}}(T)$ with some temperature T (or $\beta = \frac{1}{T}$) measured on the digital register and the second step measures the correlation function of the cluster on an analog channel. The JWT is used to map the FHM Hamiltonian to a quantum register. The general procedure is the following:

1. *Map the cluster Hamiltonian* (2.22) *to a qubit system with the* JWT*.*

2. *Evaluate the two-point correlation functions* (2.37) *for many different times for at least a full Hamiltonian cycle (at zero temperature) or until correlations flatten out. Fourier transform to obtain the frequency-dependent correlation functions. The Hamiltonian is evolved in time using Trotter steps. Note that in the Jordan-Wigner basis, $O(L_c)$ gates are needed at each time step. The full density matrix does not need to be measured, only $O(L_c^2)$ correlation functions need to be evaluated.*

3. *Again, the grand potential functional* (2.34) *and the lattice-perturbed Green's function* (2.48) *can then be evaluated efficiently on a classical computer (simple linear algebra on small $2L_c \times 2L_c$ matrices) to respectively solve the saddle-point problem and compute observables.*

A full quantum circuit to measure $\hat{\mathbf{G}}'(\omega, \mathbf{t})$ is shown in figure 3.3. The specific algorithm [108] to create a Gibbs state was chosen mostly for aesthetic reasons. It appears to be the only Gibbs state generation method that provides bounds on all parameters of the algorithm and that can be written in a circuit model. For completeness the main results of [108] are summarized and commented in appendix A.4. There is no reason to believe that other sampling methods [109–111] would not work also. A variational eigensolver [93] or an adiabatic

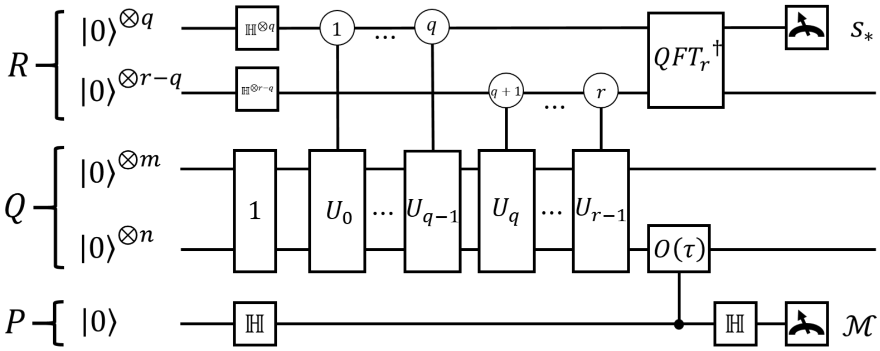
R
$|0\rangle^{\otimes q}$
$|0\rangle^{\otimes r-q}$
Q
$|0\rangle^{\otimes m}$
$|0\rangle^{\otimes n}$
P
$|0\rangle$
$\mathbb{H}^{\otimes q}$
$\mathbb{H}^{\otimes r-q}$
1
$\mathbb{H}$
1
q
q + 1
r
U_0
U_{q-1}
U_q
U_{r-1}
$QFT_r^\dagger$
$O(\tau)$
$\mathbb{H}$
s_*
$\mathcal{M}$

Figure 3.3: Circuit to simulate the time-dependent correlation function (3.24) of the cluster Hamiltonian (2.22). The first part meant to generate a Gibbs state is taken from [108]. Register R is used in the modified phase estimation scheme to prepare a rectangular state between the bath and the system contained in register Q. When the bath is traced out, the system channel is left in a Gibbs state from which the different correlation functions can be read from the one-qubit register P. The size of register Q depends on the number of orbitals in the simulated cluster (typically $n = 2L_c$) and the bath size (which can be some constant factor larger than the system register). Register R is used as a digital component and q is therefore the size required for the desired floating point accuracy on reading s_*. Note that the numbers in the controlled gates of register R denote the index of the qubit which is acting as the control.

quantum algorithm [112] could hypothetically be used to supply the initial ground state in the case of a simulation at zero temperature.

Equation (2.35) does not need to be solved explicitly on a quantum computer, only a few correlation functions of interest need to be computed, this is explained in details in subsection 3.3.2. The controlled evolution gates shown in figure 3.3 assume that the Hamiltonian of the cluster can be mapped to a Hamiltonian in the quantum computer Hilbert space. Here is the procedure to make the mapping that requires no oracle black box for $\mathcal{H}'$. The Hamiltonian (2.22) is broken into M non-commuting parts such that

$$\mathcal{H}' = \sum_{i=1}^{M} \mathcal{H}'_i. \tag{3.11}$$

Each time-step $\Delta\tau$ evolution of the cluster Hamiltonian [94] can be simulated with n_T Trotter-Suzuki steps

$$e^{-i\mathcal{H}'\Delta\tau} \simeq \left(\prod_{i=1}^{M} e^{-\frac{i\mathcal{H}'_i\Delta\tau}{n_T}}\right)^{n_T} + \sum_{i<j} \frac{\left[\mathcal{H}'_i, \mathcal{H}'_j\right]\Delta\tau^2}{2n_T} + \ldots. \tag{3.12}$$

The size of those time-steps set the upper bound in the simulated energy spectrum which scales as $\omega_{\max} \propto \frac{1}{\Delta\tau}$, while the lowest energy scales as the inverse of the total simulation time.

In the Pauli basis of the quantum computer, the terms of the cluster Hamiltonian (2.22) transform to

$$\begin{array}{rcl}
-t\sum_{\sigma}\left(c^{\dagger}_{i\sigma}c_{j\sigma} + c^{\dagger}_{j\sigma}c_{i\sigma}\right) & \longrightarrow & -t\left(\mathbb{I}^{\otimes L_c} \otimes \mathbb{T}_{L_c}(i,j) + \mathbb{T}_{L_c}(i,j) \otimes \mathbb{I}^{\otimes L_c}\right) \\
-\mu'\sum_{\sigma} n_{i\sigma} & \longrightarrow & -\mu'\left(\mathbb{I}^{\otimes L_c} \otimes \mathbb{T}_{L_c}(i) + \mathbb{T}_{L_c}(i) \otimes \mathbb{I}^{\otimes L_c}\right) \\
U n_{i\uparrow} n_{i\downarrow} & \longrightarrow & U\left(\mathbb{T}_{L_c}(i) \otimes \mathbb{T}_{L_c}(i)\right) \\
\Delta'\left(c^{\dagger}_{i\uparrow}c^{\dagger}_{i\downarrow} + c_{i\downarrow}c_{i\uparrow}\right) & \longrightarrow & \Delta'\mathbb{D}_{L_c}(i,i)\,.
\end{array} \tag{3.13}$$

The strings of Pauli matrices are defined as

$$\mathbb{T}_{L_c}(i,j) \equiv \mathbb{I}^{\otimes L_c - i} \otimes \left(\sigma_+ \otimes \sigma_z^{\otimes i-j-1} \otimes \sigma_- + \sigma_- \otimes \sigma_z^{\otimes i-j-1} \otimes \sigma_+\right) \otimes \mathbb{I}^{\otimes j-1} \tag{3.14}$$

where $i > j$ between 1 and L_c and

$$\mathbb{T}_{L_c}(i) \equiv \mathbb{I}^{\otimes L_c - i} \otimes \sigma_n \otimes \mathbb{I}^{\otimes i-1}. \tag{3.15}$$

Since $\mathbb{T}_{L_c}(i,j)$ and $\mathbb{T}_{L_c}(i)$ conserve total spin in the Pauli basis, they are also number conserving in the occupation basis. For pairing terms it is also useful to define

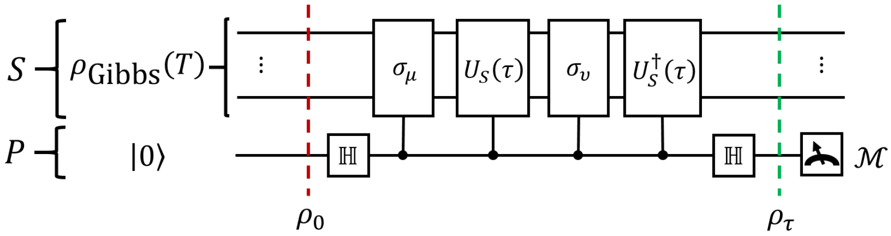

Figure 3.4: Circuit to measure the correlation function (3.24) from an input Gibbs state. Register S initially contains a given Gibbs state at inverse temperature β and register P is a single qubit initialized in the zero state. P is put in a state superposition by applying a Hadamard gate $\mathbb{H}$ and then used to apply the controlled evolution sequence $O_{\mu\nu}(\tau) \equiv U_S^\dagger(\tau)\,\sigma_\nu U_S(\tau)\,\sigma_\mu$ with $U_S(\tau) = e^{-i\mathcal{H}'\tau}$ to the system channel. Finally the state superposition is reversed by a last Hadamard gate and the measurement in repeated to obtain the probability $P(\mathcal{M})$, which returns information on the cluster Green's function (2.37).

$$\mathbb{D}_{L_c}(i,j) \equiv \mathbb{I}^{\otimes L_c - j} \otimes \left(\sigma_+ \otimes \sigma_z^{\otimes L_c - i + j - 1} \otimes \sigma_+ + \sigma_- \otimes \sigma_z^{\otimes L_c - i + j - 1} \otimes \sigma_-\right) \otimes \mathbb{I}^{\otimes i - 1}. \tag{3.16}$$

In this case, i and j can be anything between 1 and L_c. The terms of $\mathbb{D}_{L_c}(i,j)$ do not conserve total spin in the Pauli basis as they do not conserve the total number of particles in the occupation basis.

In cases where the number of electrons is conserved in the cluster Hamiltonian (with superconductivity, the anomalous pairing terms break this symmetry), it is possible to use a Bravyi-Kitaev transformation [113] for an improvement in the quantum memory usage of the algorithm ($O(\ln L_c)$). Once the mapping of $\mathcal{H}'$ to the quantum computer is known and a method to generate Gibbs state has been chosen, the correlation functions can be measured.

3.3.2 *Measuring the correlation function*

In this section an analog circuit is used to measure the correlation functions of a cluster Hamiltonian at some temperature T using a variation of the phase estimation algorithm explained in [114].. The Nambu single-particle Green's function of the cluster $\hat{\mathbf{G}}'(\omega, \mathbf{t})$ can then be recovered from the correlation function. The quantum circuit is shown in figure 3.4. It is a variation on DQC1 (deterministic quantum computation with one quantum bit) [106, 115] and phase estimation.

A thermal density matrix of the simulated system must first be prepared in register S

$$\rho_0 = \rho_{\text{Gibbs}}(\beta) \otimes |0\rangle\langle 0|, \tag{3.17}$$

where

$$\rho_{\mathrm{Gibbs}}\left(\beta\right)\equiv\frac{1}{Z}\sum_{m}e^{-\beta E_{m}}\left|\phi_{m}\right\rangle\left\langle\phi_{m}\right| \tag{3.18}$$

is a Gibbs state at some given temperature. It is to be expected that preparing a low temperature Gibbs state (large β) is hard in general [116], while high temperature Gibbs states $\beta\rightarrow 0$ are simply fully mixed states which are easier to prepare.

A sequence of controlled gates and controlled Hamiltonian evolution follows the application of a Hadamard gate on register P. The unitary evolution generated by the cluster Hamiltonian (2.22) is defined as

$$\begin{aligned} U_{S}\left(\tau\right) & \equiv e^{-i\mathcal{H}'\tau} \\ & = \textstyle\sum_{m}e^{-iE_{m}\tau}\left|\phi_{m}\right\rangle\left\langle\phi_{m}\right|. \end{aligned} \tag{3.19}$$

For convenience of notation (as seen in figure 3.3), it is useful to introduce the set of gates $O_{\mu\nu}$

$$O_{\mu\nu}\left(\tau\right)\equiv U_{S}^{\dagger}\left(\tau\right)\sigma_{\nu}U_{S}\left(\tau\right)\sigma_{\mu} \tag{3.20}$$

that define the application of a self-adjoint operator σ_{μ} on the system (detailed below), followed by forward time evolution, then the application of another σ_{ν} and finally a reverse time evolution. When applied to a Gibbs state in a phase-estimation circuit, the state of the computer at time τ is described by

$$\begin{aligned} \rho_{\tau} & \\ = & \tfrac{1}{4}\Big(\rho_{\mathrm{Gibbs}}+\rho_{\mathrm{Gibbs}}O_{\mu\nu}^{\dagger}\left(\tau\right)+O_{\mu\nu}\left(\tau\right)\rho_{\mathrm{Gibbs}}+O_{\mu\nu}\left(\tau\right)\rho_{\mathrm{Gibbs}}O_{\mu\nu}^{\dagger}\left(\tau\right)\Big) \otimes \left|0\right\rangle\left\langle 0\right| \\ + & \tfrac{1}{4}\Big(\rho_{\mathrm{Gibbs}}-\rho_{\mathrm{Gibbs}}O_{\mu\nu}^{\dagger}\left(\tau\right)+O_{\mu\nu}\left(\tau\right)\rho_{\mathrm{Gibbs}}-O_{\mu\nu}\left(\tau\right)\rho_{\mathrm{Gibbs}}O_{\mu\nu}^{\dagger}\left(\tau\right)\Big) \otimes \left|0\right\rangle\left\langle 1\right| \\ + & \tfrac{1}{4}\Big(\rho_{\mathrm{Gibbs}}+\rho_{\mathrm{Gibbs}}O_{\mu\nu}^{\dagger}\left(\tau\right)-O_{\mu\nu}\left(\tau\right)\rho_{\mathrm{Gibbs}}-O_{\mu\nu}\left(\tau\right)\rho_{\mathrm{Gibbs}}O_{\mu\nu}^{\dagger}\left(\tau\right)\Big) \otimes \left|1\right\rangle\left\langle 0\right| \\ + & \tfrac{1}{4}\Big(\rho_{\mathrm{Gibbs}}-\rho_{\mathrm{Gibbs}}O_{\mu\nu}^{\dagger}\left(\tau\right)-O_{\mu\nu}\left(\tau\right)\rho_{\mathrm{Gibbs}}+O_{\mu\nu}\left(\tau\right)\rho_{\mathrm{Gibbs}}O_{\mu\nu}^{\dagger}\left(\tau\right)\Big) \otimes \left|1\right\rangle\left\langle 1\right|. \end{aligned} \tag{3.21}$$

It can be seen that ρ_{τ} contains the information of the correlation function $\left\langle\sigma_{\nu}\left(\tau\right)\sigma_{\mu}\left(0\right)\right\rangle$, which can be measured by evaluating the probability $P_{\mu\nu}\left(\mathcal{M}=0\left(1\right),\tau\right)$ of measuring zero (one) in register P (and then Fourier transformed to obtain $\left\langle\sigma_{\nu}\sigma_{\mu}\right\rangle_{\omega}$). Formally, the interesting correlation functions that need to be extracted have the textbook form [20]

$$\begin{aligned} C_{\mu\nu}(\tau) &\equiv \left\langle \sigma_\mu(\tau)\,\sigma_\nu(0)\right\rangle \\ &= \operatorname{Tr}\left[\rho_{\text{Gibbs}} O^\dagger_{\mu\nu}(\tau) + O_{\mu\nu}(\tau)\,\rho_{\text{Gibbs}}\right] \\ &= \textstyle\sum_m \sum_n e^{-i\tau(E_m - E_n)} A^{mn}_{\mu\nu}, \end{aligned} \tag{3.22}$$

where $A^{mn}_{\mu\nu} \equiv \frac{e^{-\beta E_m} + e^{-\beta E_n}}{Z} \langle \phi_n | \sigma_\nu | \phi_m \rangle \langle \phi_m | \sigma_\mu | \phi_n \rangle$. Note that these functions always output a real number. If the controlled operation $c - O_{\mu\nu}(\tau)$ is applied for a time $\tau > 0$, the phase estimation algorithm yields the following probability for the two different outcomes $\mathcal{M} = 0$ and $\mathcal{M} = 1$

$$\begin{aligned} P_{\mu\nu}(\mathcal{M} = 0, \tau) &= \tfrac{1}{2}\left(1 + \tfrac{1}{2} C_{\mu\nu}(\tau)\right) \\ P_{\mu\nu}(\mathcal{M} = 1, \tau) &= \tfrac{1}{2}\left(1 - \tfrac{1}{2} C_{\mu\nu}(\tau)\right). \end{aligned} \tag{3.23}$$

Then from measuring the probability trajectory, the functions (3.22) can be recovered as

$$C_{\mu\nu}(\tau) = 2\left(P_{\mu\nu}(\mathcal{M} = 0, \tau) - P_{\mu\nu}(\mathcal{M} = 1, \tau)\right). \tag{3.24}$$

As in DQC1 [106], in general it is not useful to use multiple ancillary qubits and an inverse Fourier transform to extract multiple bits of the probabilities $P_{\mu\nu}$ at each measurement shot since the input ρ_{Gibbs} is a state mixture. In the case where the simulated temperature is so low that the input Gibbs state is effectively a pure (non-degenerate) ground state, it is plausible that adding qubits to register P would speed-up the measurement of the $P_{\mu\nu}$'s in the traditional sense of phase estimation [103]. The retarded Green's function can be computed numerically as

$$G^R_{\mu\nu}(\tau) \equiv -i\theta(\tau)\, C_{\mu\nu}(\tau) \tag{3.25}$$

where $\theta(\tau)$ is the Heaviside function. It can be Fourier transformed to get the Green's function in the frequency domain

$$G^R_{\mu\nu}(\omega) = \int_{-\infty}^{\infty} d\tau\, e^{-i\omega\tau} G^R_{\mu\nu}(\tau). \tag{3.26}$$

The spectral function can be obtained from the retarded Green's function as

$$\begin{aligned} A_{\mu\nu}(\omega) &= \tfrac{i}{2\pi}\left(G^R_{\mu\nu}(\omega) - G^A_{\mu\nu}(\omega)\right) \\ &= -\tfrac{1}{\pi}\operatorname{Im}\left\{G^R_{\mu\nu}(\omega)\right\}. \end{aligned} \tag{3.27}$$

Since creation and annihilation operators are not Hermitian, they cannot be used as σ_μ and σ_ν directly. A trick consists in using a linear combination of the operators. For each electron orbital, the Hermitian $X_{i\sigma}$ and $Y_{i\sigma}$ operators are defined from (3.10) such that

$$\begin{aligned} X_{i\sigma} &\equiv c_{i\sigma}+c_{i\sigma}^{\dagger} \\ Y_{i\sigma} &\equiv -i\left(c_{i\sigma}-c_{i\sigma}^{\dagger}\right). \end{aligned} \tag{3.28}$$

Note that $\left[X_{i\sigma},Y_{j\sigma'}\right]=i\delta_{ij}\delta_{\sigma\sigma'}Z_{i\sigma}$, where $Z_{i\sigma}\equiv c_{i\sigma}^{\dagger}c_{i\sigma}-\frac{1}{2}$. The elements of (2.37) can be computed from the inverse transformation

$$\begin{pmatrix} \left\langle c_{i\sigma}\left(\tau\right)c_{j\sigma'}^{\dagger}\left(0\right)\right\rangle \\ \left\langle c_{i\sigma}^{\dagger}\left(\tau\right)c_{j\sigma'}\left(0\right)\right\rangle \\ \left\langle c_{i\sigma}\left(\tau\right)c_{j\sigma'}\left(0\right)\right\rangle \\ \left\langle c_{i\sigma}^{\dagger}\left(\tau\right)c_{j\sigma'}^{\dagger}\left(0\right)\right\rangle \end{pmatrix}=\frac{1}{2}\begin{pmatrix} 1 & 1 & i & -i \\ 1 & 1 & -i & i \\ 1 & -1 & i & i \\ 1 & -1 & -i & -i \end{pmatrix}\begin{pmatrix} \left\langle X_{i\sigma}\left(\tau\right)X_{j\sigma'}\left(0\right)\right\rangle \\ \left\langle Y_{i\sigma}\left(\tau\right)Y_{j\sigma'}\left(0\right)\right\rangle \\ \left\langle Y_{i\sigma}\left(\tau\right)X_{j\sigma'}\left(0\right)\right\rangle \\ \left\langle X_{i\sigma}\left(\tau\right)Y_{j\sigma'}\left(0\right)\right\rangle \end{pmatrix} \tag{3.29}$$

Depending on the symmetries of the cluster Hamiltonian, some terms in (3.29) may be zero at all time and can be removed from the computation for speed-up or used to monitor possible errors coming from noise or other sources. A simple Fourier transform then yields the retarded Green's function $G_{\mu\nu}^{R}\left(\omega\right)$ which is used to iterate the classical algorithm until a saddle-point $\frac{\partial\Omega_t}{\partial\mathbf{t}'}=0$ of the Potthoff self-energy function is found. Depending on the symmetries of the cluster Hamiltonian, some terms in (3.29) may be zero at all time (e.g. if there is no pairing or spin-orbit interaction) and can be removed from the computation for speed-up or used to monitor possible errors coming from noise or other sources.

Let's remark that (3.24) can be expanded into a Taylor series

$$C_{\mu\nu}\left(\tau\right)=\sum_{s=0}^{\infty}\frac{\tau^{s}}{s!}C_{\mu\nu}^{(s)}. \tag{3.30}$$

The coefficients are also the moment of the Green's function in the Lehmann representation such that the coefficient which can be measured as the time derivative of (3.24) at $\tau\to 0$:

$$\begin{aligned} C_{\mu\nu}^{(s)} &= \left(-i\right)^{s}\textstyle\sum_{m}\sum_{n}A_{\mu\nu}^{mn}\left(E_m-E_n\right)^{s} \\ &= \lim_{\tau\to 0^{+}}\frac{d^{s}}{d\tau^{s}}C_{\mu\nu}\left(\tau\right) \end{aligned} \tag{3.31}$$

The retarded Green's function is then given by

$$G_{\mu\nu}^{R}\left(\omega\right)=-i\lim_{\eta\to 0^{+}}\sum_{s=0}^{\infty}\frac{C_{\mu\nu}^{(s)}}{\left(\eta+i\omega\right)^{s+1}}, \tag{3.32}$$

where η is the small parameter of the analytical continuation of the retarded function. In practice it can also be seen as an effective inverse simulated time (or "decoherence rate"). If one can measure several cycles of the correlation functions (3.30), then the extracted spectra will be sharply defined and η can be considered effectively small with respect to all simulated energies in the cluster Hamiltonian. In the other limit, if there is too much decoherence in the quantum simulator the measured correlation functions will be flat and no information can be extracted about the frequency dependence of (3.32), η is then effectively related to the decoherence rate if it limits the simulated time.

3.4 CONCLUSION

We have outlined a method to compute different observables of the FHM using a quantum computer. It synthesizes and builds mainly on the work of [56, 59, 87, 94, 108]. Provided that the lattice can be divided into clusters (with L_c spin-$\frac{1}{2}$ orbitals) which are coupled only with one-body hopping terms, section 2.3 reviewed how a variational principle for the grand canonical potential of the model can be used to approximate the self-energy of the lattice Hamiltonian and account for possible long-range ordering effects.

In chapter (2), the formalism to define a cluster was reviewed in section 2.4 through the form of an example 2D lattice divided in 2×2 clusters for which a few order parameters like anti-ferromagnetism and superconductivity can be described and observable quantities computed. Assuming no spin, spatial or electron-hole symmetries in the cluster, up to $4L_c^2$ variational terms can be defined. The nature of the saddle-point problem that needs to be solved numerically has been detailed and the bottleneck has been shown to be the diagonalization and the simulation of the cluster which have to be solved for several variational parameters. The memory scaling is known to be very bad on classical computers as the dimension of the Hilbert space of a cluster scales as 4^{L_c} in the number of orbitals. In chapter (3), the method to create a Gibbs state and measure correlation functions on a quantum computer was presented in section 3.3. It is shown that there are $4L_c^2$ time correlation functions that need to be measured each round of the saddle-point optimization problem.

This algorithm provides a novel way to simulate complex materials at the electronic level and study new questions without knowing the answer in advance. However some aspects could be improved. The Bravyi-Kitaev transformation is known to significantly improve the scaling of classical algorithm in the case where the number of electrons is conserved by the Hamiltonian [113] but a similar ansatz may also improve the method presented in this chapter (by dividing the Hilbert space in even/odd occupation blocks for example). Notably, it is not fully clear whether the transformation on the Gibbs state be conditionally reversed after a measurement in such a way that the state can be reused. The back-action of the correlation function measurement may prevent the recycling of the Gibbs state. Also, it may be possible to estimate the errors of the algorithm by simulating a known system and comparing with analytical results (for example one could simulate the well-known tight-binding model to benchmark the quantum algorithm). Finally, it is possible that the method can be extended to simulate non-equilibrium processes [117] by measuring the Keldysh matrices G^R,G^A and G^K. Since the VCA is known to work with fermions, bosons and spins, one can imagine that a large quantum computer could be used to simulate complex materials involving many of those quantum objects at the same time, such as in the Kondo lattice model or in Holstein polaron dynamics. A similar construction where a functional would also integrate an interaction across clusters [85] could also be considered.

The next chapter focussed on giving an explicit gate decomposition for the circuit of figure 3.3.

4

QUANTUM GATES AND ARCHITECTURE FOR A QUANTUM SIMULATOR

4.1 OVERVIEW

Simulating quantum phenomena with classical computers is often hard. This observation originated the idea of universal quantum simulators, or quantum computers [89]. Since then, technology has advanced to the point where small collections of interacting quantum bits (qubits) can be fabricated, characterized and controlled to find the ground state energy of simple molecules [118] in quantum chemistry. Scaling to a few tens or hundreds of highly coherent qubits will open new ways to study classes of important but classically intractable problems. The prototypical non-integrable system where long-range entanglement and short-range fluctuations makes classical simulation prohibitive is the two-dimensional FHM, where electrons can hop on a bipartite lattice with local Coulomb interaction (see chapter (2)). Despite its apparent simplicity, it has been shown that scattering particles in clusters of the FHM is sufficient to implement any quantum computation [52]. As in the simulation of quantum chemistry [93, 104, 118, 119], the simulation of strongly correlated materials can also be improved by hybrid quantum-classical solver [90–92, 94, 95, 120] even if the number of interacting particles is in principle macroscopic.

To study phase transitions occurring in condensed matter systems, single-particle correlation functions containing the information of the dynamics of the excited states have to be computed. Correlated lattices can be approximated in variational algorithms by constraining the space of possible self-energies to that of a lattice of finite clusters [57]. The solutions can be refined systematically by increasing the size of the clusters, however the classical memory required to represent state vectors in the clusters Hilbert space increases exponentially with the number of simulated electronic orbitals in a cluster. We showed in chapter 3 how to extend the range of applicability of variational classical cluster methods by leveraging small quantum computers. The quantum algorithm uses black-box time evolutions [121] without making any assumptions on the architecture of the underlying quantum computer. This chapter is meant to extend the quantum algorithm and to present a natural architecture and gate decomposition as an example to a general-purpose quantum simulator for dynamical cluster methods. Such a device could significantly improve our capabilities to investigate and simulate the macroscopic properties of correlated systems of electrons.

Here we present four main results. First, a practical physical layout of the simulator can be made with two parallel chains of qubits with nearest-neighbor interactions and a control/probe qubit connected to all elements of the chains. The layout is fabrication-friendly as it has no crossing interaction lines, yet it can simulate Gibbs states of a lattice of arbitrary dimensionality. Second, there is a limited number of three-qubit gates that need to be tuned and benchmarked prior to a simulation, these gates are called "conditional imaginary swap" ($c - \pm$iSWAP or iFredkin) with positive and negative varieties. Third, the toughest terms of a cluster Hamiltonian can be decomposed in a number of gates which is sub-quadratic in the size of the cluster. Finally, a numerical example is used to show that the Trotter-Suzuki approximations can reach arbitrary precision when non-commuting terms in the cluster Hamiltonian are propagated in time.

Specifically, the chapter is structured in the following way. In section 4.2, the FHM is briefly introduced. In subsection 3.3.1, the core elements of the quantum solver are reviewed and an architecture is proposed for a quantum simulator. In section 4.3 the gate decomposition of the time evolution of the cluster is given through the example of a 2×2 FHM cluster. The JWT used is shown in subsection 4.3.1 and subsection 3.3.2 introduces the notation used in the procedure to measure the correlation function and more notation concerning the mapping of qubits to spin orbitals. The explicit gate decomposition of important terms of the FHM are given in subsection 4.3.2. A short analysis of Trotter-Suzuki errors is done in subsection 4.3.3. Finally, the scaling properties of the quantum resources involved in scaling the algorithm are analyzed in section 4.4.

4.2 A QUANTUM SIMULATOR FOR THE FERMI-HUBBARD MODEL

In chapter 3, we showed how the important information of the clusters could be extracted from a quantum computer. In the next part, we explain how an architecture can be chosen for a quantum simulator such that the time evolution of any cluster Hamiltonian becomes very natural.

4.2.1 *The layout of qubits*

We introduced an hybrid quantum-classical solver in chapter 3 to show how some parts of quantum cluster methods can be improved by executing them on universal quantum computers. In this chapter we show that there is a simple physical layout of qubits which implements naturally the quantum circuit of figure 4.1a. The circuit is used to prepare a Gibbs state of a cluster of the FHM in register S

and output the single-particle correlation functions in register P (the operator $O(\tau)$ is detailed in section 3.3.2). In principle the same type of circuit can simulate many other physical models, the FHM is used as an example that encapsulates the essence of strongly correlated systems. Since each register performs a definite task in the algorithm, the qubit layout can also be divided into modules. A subtle but important difference to figure 3.3 consists in controlling the bath (B) + system (S) registers through qubit P. This significantly reduces the number of elements that have to be controlled on the quantum simulator chip. Since the extraction of the correlation functions is done by measuring the probability of $\mathcal{M} = 1$ and given that S is in general in a mixed state, there is no clear advantage to using more than one qubit in register P. It can therefore be used to mediate the operations between register R and $S + B$ in the Gibbs state preparation protocol (see figure 4.1b). The suggested physical layout of qubits is shown in figure 4.2, the qubits of R and $S + B$ are aligned as parallel chains with nearest-neighbor interactions and all conditional operations from R are mediated through qubit P. An important feature of the proposed physical layout is the absence of overlapping interaction lines. Compared to a general purpose quantum computer, a dedicated quantum circuit has a much smaller set of gates that have to be tuned and benchmarked to solve a class of problems. Register R needs only to support single qubits Hadamard gates and the operations required for an inverse quantum Fourier transform ($\mathrm{QFT}^{\dagger}$), only q qubits are measured to determine the effective temperature β of the Gibbs state prepared (depending on the output s_{*}, see [108] for details). The operations between P and B can all be reduced to controlled single qubits phase rotations as the bath is assumed to consists of independent spins. The operations between P and S require a more detailed analysis.

First, a one dimensional chain of qubits with local controls and nearest neighbor exchange interaction is sufficient to implement the simulation of a higher dimensional cluster of a correlated electrons system. The exchange interaction can be used to generate the iSWAP gate which can be used to implement any Pauli string arising from the Jordan-Wigner form of given fermionic cluster Hamiltonians [122]. Two dimensional clusters of the FHM can be simulated efficiently with a number of gates which scales sub-quadratically with the number of orbitals. Finally, using a Trotter-Suzuki decomposition, the time evolution can be implemented accurately and with a better scaling than typical “hard” molecules [123].

For a cluster with L_c sites, it is convenient to order the JWT basis such that up/down spins orbitals for each site are adjacent:

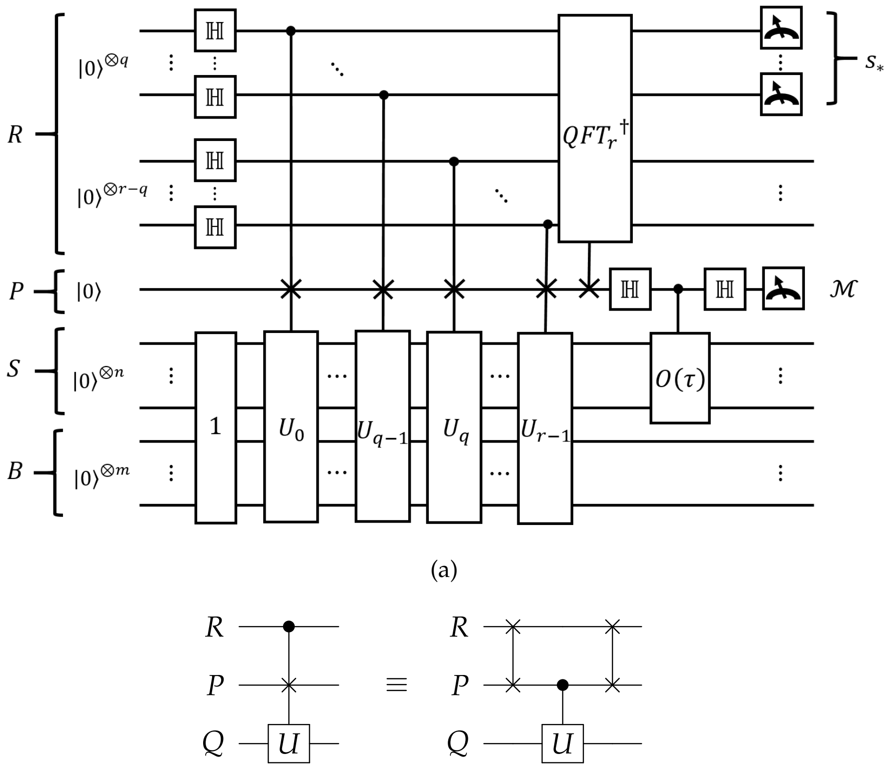

(a)

(b)

Figure 4.1: In (a), the circuit used to simulate the time-dependent correlation function of the cluster Hamiltonian (2.22) is shown. It has been rearranged from figure 3.3 to use register P as a mediator between register R and S and B. Figure (b) shows how the interaction through register P is done and the inverse QFT is the reverse sequence (and opposite angles) of the decomposition shown in figure 3.1. In total, $4q - 2$ SWAP gates are required. Alternatively, only one swap per step can be used if the initial Hadamard gates from figure 4.1a are done directly on P.

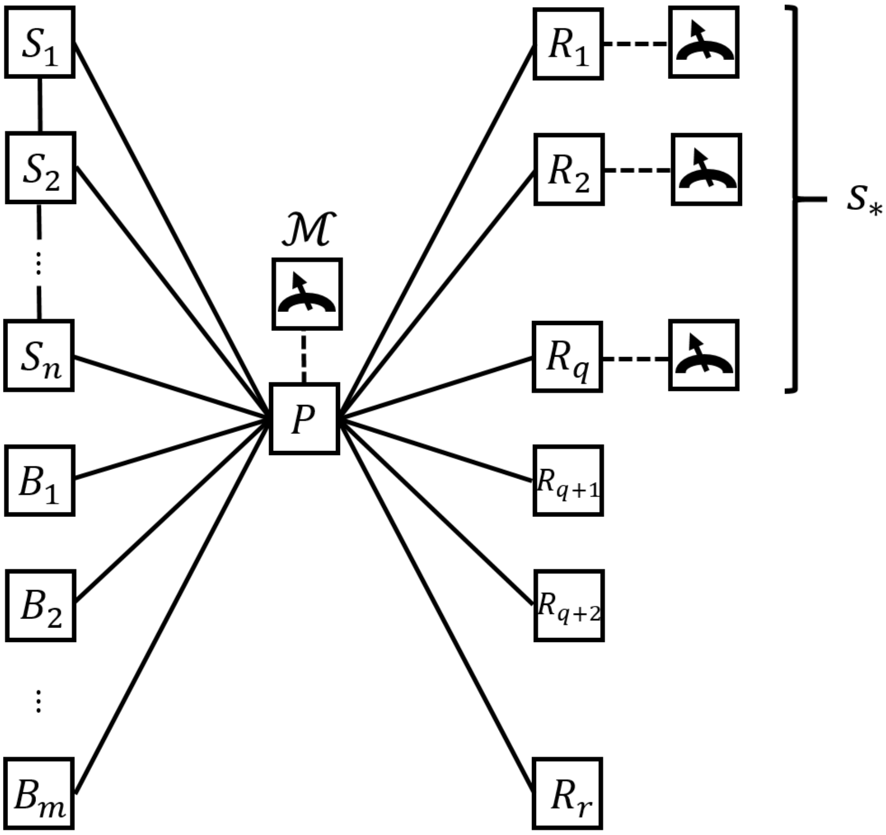

Figure 4.2: Proposed layout of physical qubits with no crossing interaction line. Boxes represent physical qubits in different labeled registers. Arbitrary single qubit gates are assumed to be implementable on every qubit. Solid lines are tunable exchange interactions ($\sigma_x \otimes \sigma_x + \sigma_y \otimes \sigma_y$). Early numerical work also suggests using tunable dispersive interactions ($\sigma_z \otimes \sigma_z$) for the $S - P$ and $B - P$ connections to implement the required conditional two-qubit gates more efficiently. The interactions between the qubits in registers S (or B) and the qubit in P are used to implement conditional ±iSWAPs and controlled single-qubit gates. The interactions between the qubits in register R and the one in register P are only used to implement SWAP gates. The interactions between the qubits in R are used to implement QFT† on this register. Dashed lines are linked to qubits that are measured in the computational basis at the end of the protocol. There are only a very limited number of gates to benchmark and tune. The size the register R depends on the desired precision and accuracy of the Gibbs state preparation (floating point accuracy should roughly correspond to the quantum supremacy crossover for this register). The size of register S should be at least as large as the number of spin orbitals in the simulated cluster Hamiltonian and the size of register B is equal to the size of register S such that it can absorb the excess entropy of the Gibbs state preparation.

$$\begin{aligned} X_{i\uparrow} &= \mathbb{I}^{\otimes 2(L_c-i)+1} \otimes \sigma_x \otimes \sigma_z^{\otimes 2(i-1)} \\ X_{i\downarrow} &= \mathbb{I}^{\otimes 2(L_c-i)} \otimes \sigma_x \otimes \sigma_z^{\otimes 2i-1} \\ Y_{i\uparrow} &= \mathbb{I}^{\otimes 2(L_c-i)+1} \otimes \sigma_y \otimes \sigma_z^{\otimes 2(i-1)} \\ Y_{i\downarrow} &= \mathbb{I}^{\otimes 2(L_c-i)} \otimes \sigma_y \otimes \sigma_z^{\otimes 2i-1}. \end{aligned} \tag{4.1}$$

These operators must be implemented as operations controlled from register P,

$$\begin{aligned} \mathrm{c}{-}X_{i\sigma} &= |0\rangle\langle 0| \otimes \mathbb{I}^{\otimes 2L_c} + |1\rangle\langle 1| \otimes X_{i\sigma} \\ \mathrm{c}{-}Y_{i\sigma} &= |0\rangle\langle 0| \otimes \mathbb{I}^{\otimes 2L_c} + |1\rangle\langle 1| \otimes Y_{i\sigma} \end{aligned} \tag{4.2}$$

for spins ↑ / ↓ and i between 1 and L_c. These operators are easy to construct using the method found in [122] and the types of sequences found in the next section. Following the first c$-\sigma_\mu$ operation, the S register is conditionally evolved with the cluster Hamiltonian $\mathcal{H}'$:

$$\mathrm{c}{-}U_S(\tau) \equiv |0\rangle\langle 0| \otimes \mathbb{I}^{\otimes 2L_c} + |1\rangle\langle 1| \otimes e^{-i\mathcal{H}'\tau}. \tag{4.3}$$

Section 4.3 is dedicated to the precise gate decomposition of (4.3) as it was treated as a black-box in chapter 3.

4.3 TIME EVOLUTION OF THE CLUSTER HAMILTONIAN

In this section we will show how a typical trial cluster Hamiltonian for the FHM in 2D can be implemented accurately using a reasonable number of gates. In order to keep the notation straightforward, this is done through the example of a 2×2 cluster with magnetic and superconducting trial terms which can be easily generalized to larger sizes and higher dimensions. After introducing the cluster Hamiltonian and some notation, the gates for the implementation of (4.3) will be shown for the example and a numerical estimate of the Trotter-Suzuki error will be provided. Along the way, “conditional imaginary swaps” or c $-$ ±iSWAPs will be introduced as three-qubit quantum gates practical for quantum simulations. Although they can be viewed as a complements to the traditional Toffoli (c $-$ c $-$ NOT) and Fredkin (c $-$ SWAP) gates [103], the positive or negative imaginary phase in the “±iFredkin” gates has no classical analog and makes them truly quantum operations.

4.3.1 *Hamiltonian of a cluster*

Each cluster includes only a small subset of the terms of the original lattice and variational terms must also be included to account for possible long-range order. For convenience, let's assume a square lattice with constant spacing a. It is broken down into N_c clusters each with L_c s-shell sites with two electrons each (spin up ↑ and spin down ↓). The Hamiltonian of each cluster is given by

$$\mathcal{H}' = \mathcal{H}_{\text{kin}} + \mathcal{H}_{\text{int}} - \mathcal{H}_{\text{s-pair}} - \mathcal{H}_{\text{d}_{\text{x}^2-\text{y}^2}} - \mathcal{H}_{\text{local}} - \mathcal{H}_{\text{AF}}, \tag{4.4}$$

where $\mathcal{H}_{\text{kin}}$ is the kinetic term, $\mathcal{H}_{\text{int}}$ is the local Coulomb interaction, $\mathcal{H}_{\text{s-pair}}$ and $\mathcal{H}_{\text{d}_{\text{x}^2-\text{y}^2}}$ are variational pairing terms, $\mathcal{H}_{\text{local}}$ is a variational chemical potential term and $\mathcal{H}_{\text{AF}}$ is a variational Néel antiferromagnetic term. The variational self-energy functional method support many different Hamiltonian terms and models as long as the two-body interaction term is "local" enough that a cluster decomposition can be made without cutting any interaction link.

Figure 4.3 show how the qubits of S register are labeled to represent the electronic structure of the cluster and requires $2L_c$ qubits (1 qubit = 1 spin-orbital). Since the qubits are effectively distinguishable spins, the JWT from section 3.2.5 must be used to model accurately the fermionic statistics of indistinguishable electrons. The sites are simply assumed to be labeled sequentially when counting the gate numbers for larger cluster sizes in section 4.4.

4.3.1.1 *Some convenient Pauli strings*

To define the Hamiltonian terms of (2.22) in the Jordan-Wigner basis, it is useful to introduce the following strings of Pauli matrices. The hopping part of the Hamiltonian usually contains terms of the form

$$\begin{aligned}
&\mathbb{T}_{L_c\uparrow}(i,j)\\
\equiv\ & \mathbb{I}^{\otimes 2(L_c-j)+1} \otimes \left(\sigma_+ \otimes \sigma_z^{\otimes 2(j-i)-1} \otimes \sigma_- + \sigma_- \otimes \sigma_z^{\otimes 2(j-i)-1} \otimes \sigma_+\right) \otimes \mathbb{I}^{\otimes 2(i-1)}\\
=\ & 2\mathbb{I}^{\otimes 2(L_c-j)+1} \otimes \left(\sigma_x \otimes \sigma_z^{\otimes 2(i-j)-1} \otimes \sigma_x + \sigma_y \otimes \sigma_z^{\otimes 2(j-i)-1} \otimes \sigma_y\right) \otimes \mathbb{I}^{\otimes 2(i-1)}\\
&\mathbb{T}_{L_c\downarrow}(i,j)\\
\equiv\ & \mathbb{I}^{\otimes 2(L_c-j)} \otimes \left(\sigma_+ \otimes \sigma_z^{\otimes 2(i-j)-1} \otimes \sigma_- + \sigma_- \otimes \sigma_z^{\otimes 2(j-i)-1} \otimes \sigma_+\right) \otimes \mathbb{I}^{\otimes 2i-1}\\
=\ & 2\mathbb{I}^{\otimes 2(L_c-j)} \otimes \left(\sigma_x \otimes \sigma_z^{\otimes 2(i-j)-1} \otimes \sigma_x + \sigma_y \otimes \sigma_z^{\otimes 2(j-i)-1} \otimes \sigma_y\right) \otimes \mathbb{I}^{\otimes 2i-1},
\end{aligned} \tag{4.5}$$

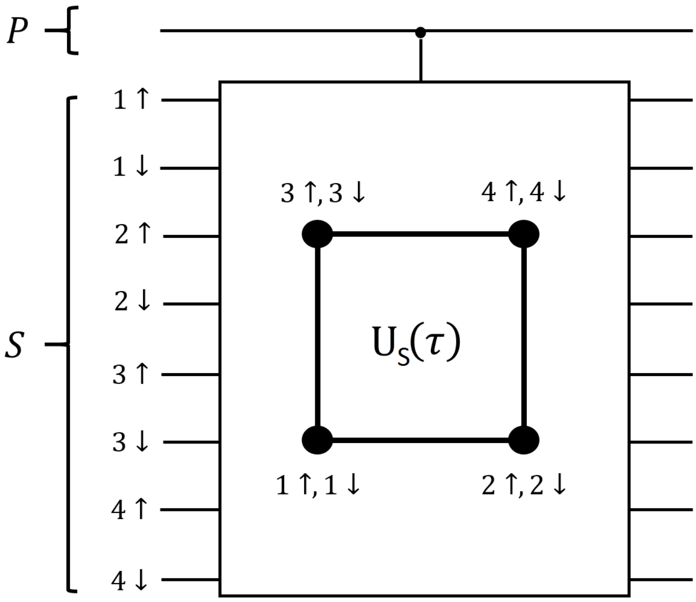

Figure 4.3: The chain of physical qubits representing the system register is easy to represent and operate on in the gate model of computation. For a $n = 2L_c$ square lattice, the sites are labeled sequentially in linear stripes, this ensures that nearest-neighbor coupling terms of the Hamiltonian in the Jordan-Wigner basis can be represented as Pauli strings of length at most $O\left(2\sqrt{L_c}\right)$.

where $j > i$ between 1 and L_c. These strings have the property $\left[\mathbb{T}_{L_c\sigma}(i,j), \mathbb{T}_{L_c\sigma'}(i',j')\right] = 0$. The chemical potential and the variational anti-ferromagnetic terms built from $n_{i\sigma}$ operators have strings of the form

$$\begin{aligned} \mathbb{T}_{L_c\uparrow}(i) &\equiv \mathbb{I}^{\otimes 2(L_c-i)+1} \otimes \sigma_n \otimes \mathbb{I}^{\otimes 2(i-1)} \\ \mathbb{T}_{L_c\downarrow}(i) &\equiv \mathbb{I}^{\otimes 2(L_c-i)} \otimes \sigma_n \otimes \mathbb{I}^{\otimes 2i-1}. \end{aligned} \tag{4.6}$$

Since $\mathbb{T}_{L_c}(i,j)$ and $\mathbb{T}_{L_c}(i)$ conserve total spin in the Pauli basis, they are also number conserving in the occupation basis.

$$\begin{aligned}
&\mathbb{D}_{L_c\uparrow}(i,j)\\
\equiv\;& \mathbb{I}^{\otimes 2(L_c-j)} \otimes \left(\sigma_+ \otimes \sigma_z^{\otimes 2(j-i)} \otimes \sigma_+ + \sigma_- \otimes \sigma_z^{\otimes 2(j-i)} \otimes \sigma_-\right) \otimes \mathbb{I}^{\otimes 2(i-1)}\\
=\;& 2\mathbb{I}^{\otimes 2(L_c-j)} \otimes \left(\sigma_x \otimes \sigma_z^{\otimes 2(j-i)} \otimes \sigma_x - \sigma_y \otimes \sigma_z^{\otimes 2(j-i)} \otimes \sigma_y\right) \otimes \mathbb{I}^{\otimes 2(i-1)}\\
&\mathbb{D}_{L_c\downarrow}(i,j)\\
\equiv\;& \mathbb{I}^{\otimes 2(L_c-j)+1} \otimes \left(\sigma_+ \otimes \sigma_z^{\otimes 2(j-i-1)} \otimes \sigma_+ + \sigma_- \otimes \sigma_z^{\otimes 2(j-i-1)} \otimes \sigma_-\right) \otimes \mathbb{I}^{\otimes 2i-1}\\
=\;& 2\mathbb{I}^{\otimes 2(L_c-j)+1} \otimes \left(\sigma_x \otimes \sigma_z^{\otimes 2(j-i-1)} \otimes \sigma_x - \sigma_y \otimes \sigma_z^{\otimes 2(j-i-1)} \otimes \sigma_y\right) \otimes \mathbb{I}^{\otimes 2i-1}
\end{aligned} \tag{4.7}$$

in this case, $j > i$ can be anything between 1 and L_c. $\mathbb{D}_{L_c}(i,j)$ does not conserve total spin in the Pauli basis and it is not conserving in the occupation basis. The $\mathbb{D}_{L_c\sigma}(i,j)$ are used to represent pairing operators between different sites in the Pauli basis.

$$\begin{aligned}
\mathbb{D}_{L_c}(i) &\equiv \mathbb{I}^{\otimes 2(L_c-i)} \otimes (\sigma_+ \otimes \sigma_+ + \sigma_- \otimes \sigma_-) \otimes \mathbb{I}^{\otimes 2(i-1)}\\
&= 2\mathbb{I}^{\otimes 2(L_c-i)} \otimes \left(\sigma_x \otimes \sigma_x - \sigma_y \otimes \sigma_y\right) \otimes \mathbb{I}^{\otimes 2(i-1)}
\end{aligned} \tag{4.8}$$

The $\mathbb{D}_{L_c}(i)$ operators are used to represent local pairing operators in the Pauli basis.

4.3.2 *Gate decomposition*

Here we proceed to decomposing the terms of the cluster Hamiltonian (2.22). This is not an exhaustive list of all possible variational terms nor of the detailed decomposition method as it is covered in [122]. The aim is to provide an estimate of the number of quantum gates required during the simulation of the FHM. It is also shown that different blocks of the cluster Hamiltonian can be implemented exactly. The time evolution of the blocks that do not commute can be approximated by a Trotter-Suzuki approximation detailed in section (4.3.3).

Let's note we are using the single-qubit gates from table 3.1. Given a tunable nearest-neighbor exchange interaction $\sigma_x \otimes \sigma_x + \sigma_y \otimes \sigma_y$ between the qubits of register S, it naturally generates the "imaginary swap" gate

$$\begin{aligned} \pm\text{iSWAP} &= e^{\pm i\frac{\pi}{4}\left(\sigma_x\otimes\sigma_x+\sigma_y\otimes\sigma_y\right)} \\ &= \begin{pmatrix} 1 & 0 & 0 & 0 \\ 0 & 0 & \pm i & 0 \\ 0 & \pm i & 0 & 0 \\ 0 & 0 & 0 & 1 \end{pmatrix}. \end{aligned} \tag{4.9}$$

It has the nice property that it can be used to manipulate Pauli strings that appear in the JWT:

$$\begin{aligned} +\text{iSWAP}\cdot\left(\mathbb{I}\otimes\sigma_x\right)\cdot -\text{iSWAP} &= \sigma_y\otimes\sigma_z \\ +\text{iSWAP}\cdot\left(\mathbb{I}\otimes\sigma_y\right)\cdot -\text{iSWAP} &= -\sigma_x\otimes\sigma_z \\ +\text{iSWAP}\cdot\left(\mathbb{I}\otimes\sigma_z\right)\cdot -\text{iSWAP} &= \sigma_z\otimes\mathbb{I}. \end{aligned} \tag{4.10}$$

To implement a conditional evolution gates of the form (4.3), we introduce $\mathrm{c}-\pm$iSWAPs as fundamental 3-qubit gates for quantum simulations. These gates come only in two varieties ($\pm$) for each triple of qubits (qubit P and two adjacent qubits in S). Since all other operations are conditional single-qubit gates, they are expected to be the most time-consuming operations and therefore they are used to benchmark the scaling properties of the algorithm. Let's note that there appears to be numerical evidence that coupling the P and the S registers with tunable $\sigma_z\otimes\sigma_z$ interactions greatly simplifies the implementation of the $\mathrm{c}-\pm$iSWAP gates [124]. This somewhat extends the tool set of three-qubit gates for reversible quantum computation, which already contains Toffoli and Fredkin gates. "Conditional single-qubit gates" is abbreviated by $\mathrm{c}-\mathrm{SQG}$.

4.3.2.1 *Local terms*

Local terms are all one-body terms composed with the $n_{i\sigma}$ operators. This includes the chemical potential

$$\begin{aligned} \mathcal{H}_{\text{local}} &= \mu'\textstyle\sum_{i,\sigma} n_{i\sigma} \\ &= \mu'\textstyle\sum_{i=1}^{L_c}\left(\mathbb{T}_{L_c\uparrow}\left(i\right)+\mathbb{T}_{L_c\downarrow}\left(i\right)\right) \end{aligned} \tag{4.11}$$

which is kept as a variational term to enforce the thermodynamic consistency of the electronic occupation value. The $\mathbb{T}_{L_c\sigma}\left(i\right)$ strings

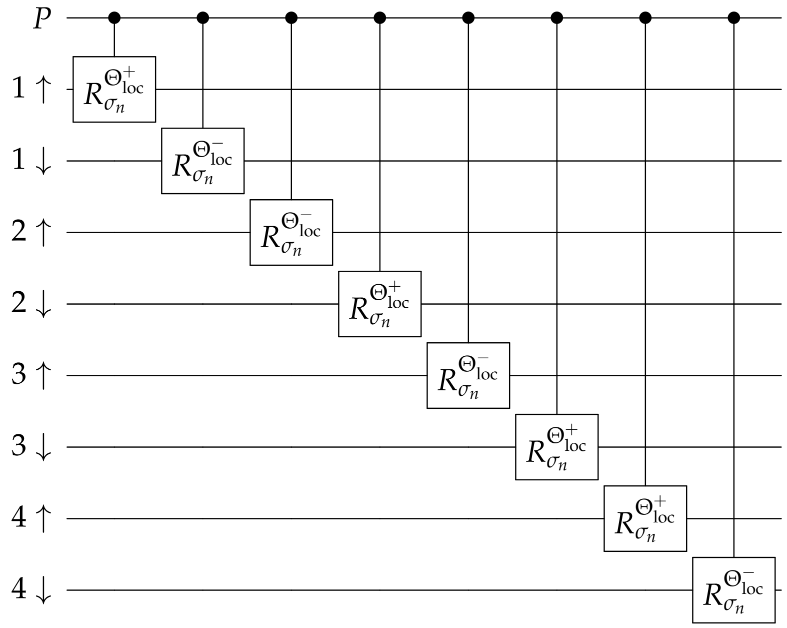
P
1 ↑
1 ↓
2 ↑
2 ↓
3 ↑
3 ↓
4 ↑
4 ↓
$R_{\sigma_n}^{\Theta_{\text{loc}}^{+}}$
$R_{\sigma_n}^{\Theta_{\text{loc}}^{-}}$
$R_{\sigma_n}^{\Theta_{\text{loc}}^{-}}$
$R_{\sigma_n}^{\Theta_{\text{loc}}^{+}}$
$R_{\sigma_n}^{\Theta_{\text{loc}}^{-}}$
$R_{\sigma_n}^{\Theta_{\text{loc}}^{+}}$
$R_{\sigma_n}^{\Theta_{\text{loc}}^{+}}$
$R_{\sigma_n}^{\Theta_{\text{loc}}^{-}}$

Figure 4.4: The local terms of the cluster Hamiltonian corresponding to the time evolution of $\mathcal{H}_{\text{local}}$ and $\mathcal{H}_{\text{AF}}$. The single qubit rotation $R^{\Theta}_{\sigma_n} \equiv e^{-i\frac{\Theta}{2}} e^{-i\frac{\Theta}{2}\sigma_z}$, the angles $\Theta^{\pm}_{\text{loc}} \equiv -\Delta\tau\left(\mu' \pm M'\right)$. There are $2L_c$ c − SQGs in a square cluster (8 c − SQGs in a 2×2 cluster).

are given by (4.6). The variational Néel anti-ferromagnetic Weiss field is also a local term which takes the form

$$\begin{aligned} \mathcal{H}_{\text{AF}} &= M' \textstyle\sum_i e^{i\mathbf{Q}\cdot\mathbf{R}_i}\left(n_{i\uparrow} - n_{i\downarrow}\right) \\ &= M' \textstyle\sum_{i=1}^{L_c} e^{i\mathbf{Q}\cdot\mathbf{R}_i}\left(\mathbb{T}_{L_c\uparrow}(i) - \mathbb{T}_{L_c\downarrow}(i)\right) \end{aligned} \tag{4.12}$$

where $\mathbf{Q} = (\pi, \pi)$ is the anti-ferromagnetic wave vector and $\mathbf{R}_i$ is the position of the site in units of a. These terms all commute between each other and do not require any c − ±iSWAP, only $2L_c$ c$-R^{\Theta}_{\sigma_n}$ are required, where

$$R^{\Theta}_{\sigma_n} \equiv e^{-i\frac{\Theta}{2}} e^{-i\frac{\Theta}{2}\sigma_z}. \tag{4.13}$$

The gate sequence is shown in figure 4.4.

4.3.2.2 *Interaction terms*

The fixed interaction terms are given by

$$\begin{aligned} \mathcal{H}_{\text{int}} &= U \textstyle\sum_i n_{i\uparrow} n_{i\downarrow} \\ &= U \textstyle\sum_{i=1}^{L_c} \mathbb{T}_{L_c\uparrow}(i) \cdot \mathbb{T}_{L_c\downarrow}(i), \end{aligned} \tag{4.14}$$

where the $\mathbb{T}_{L_c\sigma}(i)$ strings are given by 4.6. From figures 4.5a and 4.5b, it can seen that L_c c − +iSWAPs, L_c c − −iSWAPs , $2L_c$ c$-\mathbb{H}$ on spin-↓ orbitals, L_c c$-R^{\Theta}_{\sigma_U}$ on spin-↑ orbitals and $2L_c$c$-R^{\Theta}_{\sigma_n}$ on all

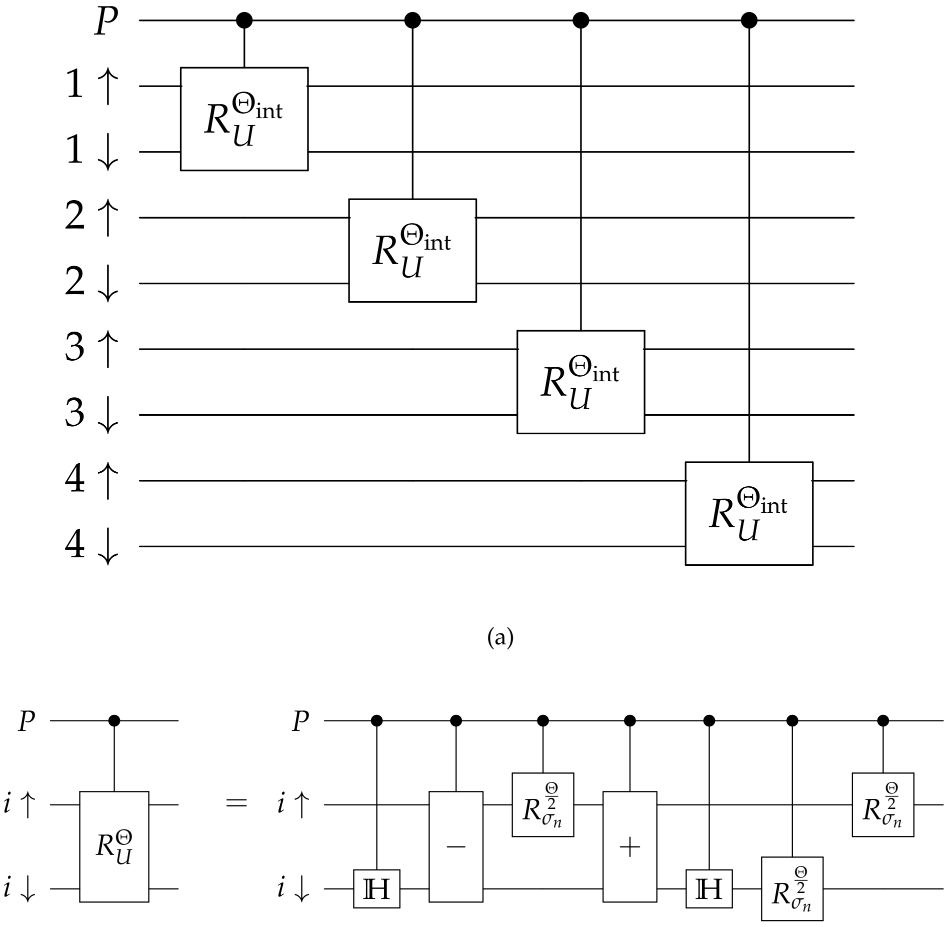
P
$1\uparrow$
$1\downarrow$
$2\uparrow$
$2\downarrow$
$3\uparrow$
$3\downarrow$
$4\uparrow$
$4\downarrow$
$R_U^{\Theta_{\text{int}}}$
$R_U^{\Theta_{\text{int}}}$
$R_U^{\Theta_{\text{int}}}$
$R_U^{\Theta_{\text{int}}}$
P
$i\uparrow$
$i\downarrow$
R_U^{Θ}
$=$
P
$i\uparrow$
$i\downarrow$
$\mathbb{H}$
$-$
$R_{\sigma_n}^{\frac{\Theta}{2}}$
$+$
$\mathbb{H}$
$R_{\sigma_n}^{\frac{\Theta}{2}}$
$R_{\sigma_n}^{\frac{\Theta}{2}}$

(a)

(b)

Figure 4.5: In (a), the interaction terms of the cluster Hamiltonian corresponding to the time evolution of $\mathcal{H}_{\text{int}}$ are decomposed into gates. The angle $\Theta_{\text{int}} \equiv +\Delta\tau U$. In (b), the decomposition of c$-R_U^{\Theta}$ in a site subspace (spin ↑/↓) is shown. There are L_c terms like these in a square cluster. The single-qubit rotation gate $R_{\sigma_U}^{\Theta} \equiv e^{+i\frac{\Theta}{2}} e^{-i\frac{\Theta}{2}\sigma_y}$. There are 5 c − SQGs and 2 c − ±iSWAPs per c$-R_U^{\Theta}$.

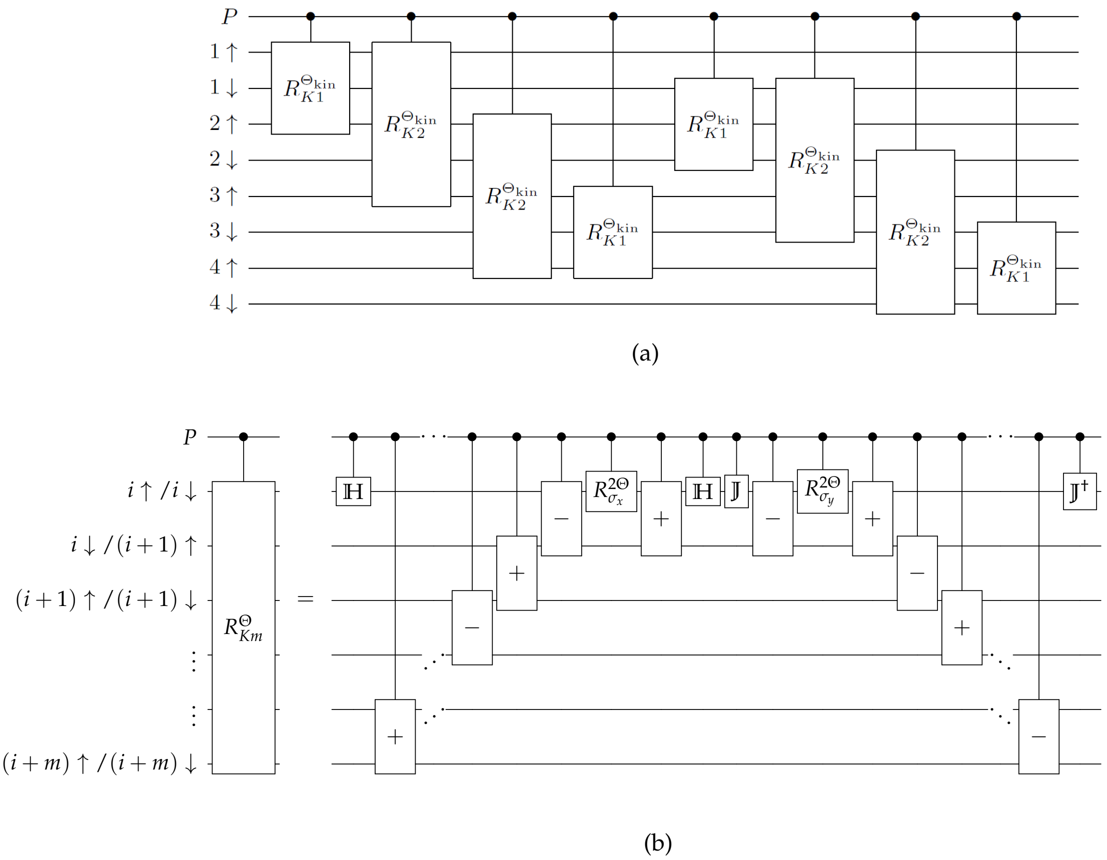

Figure 4.6: In (a), the hopping terms of the cluster Hamiltonian corresponding to the time evolution of $\mathcal{H}_{\text{kin}}$ are decomposed into gates. The angle $\Theta_{\text{int}} \equiv -\Delta\tau t$. There are $4\left(L_c - \sqrt{L_c}\right)$ terms like these in a square lattice. Half contains Pauli strings of length 3 and the other half has length $2\sqrt{L_c}+1$. In (b), the decomposition of c$-R^{\Theta}_{Km}$ in a subspace starting at $i\uparrow$ ($i\downarrow$) and ending at $i+m\uparrow$ ($i+m\downarrow$), where $m=1$ or $\sqrt{L_c}$ in a square lattice with nearest-neighbor hopping. There are 6 c − SQGs and $4m$ c − ±iSWAPs per c$-R^{\Theta}_{Km}$.

qubits (those should be done at the same time as the gates of figure 4.4, then only the resources from the interaction terms have to be counted) are required to implement the evolution of $\mathcal{H}_{\text{int}} + \mathcal{H}_{\text{local}} + \mathcal{H}_{\text{AF}}$. These terms are simple to implement and they commute with the local terms $\mathcal{H}_{\text{local}}$ and $\mathcal{H}_{\text{AF}}$, so they should be done in sequence.

4.3.2.3 *Hopping terms*

The hopping terms between nearest-neighbors is given by

$$\begin{aligned} \mathcal{H}_{\text{kin}} &= -t\sum\nolimits_{\langle i,j\rangle,\sigma} c^\dagger_{i\sigma}c_{j\sigma} + c^\dagger_{j\sigma}c_{i\sigma} \\ &= -t\sum\nolimits_{\langle i,j\rangle}\left(\mathbb{T}_{L_c\uparrow}(i,j) + \mathbb{T}_{L_c\downarrow}(i,j)\right) \end{aligned} \tag{4.15}$$

for all neighboring orbitals $\langle i,j\rangle$ such that $j>i$. The summation $\sum_{\langle i,j\rangle}$ has $2\left(L_c-\sqrt{L_c}\right)$ nearest-neighbor vertices. The $\mathbb{T}_{L_c\sigma}\left(i,j\right)$ strings are given by (3.14). From figures 4.6a and 4.6b, it can seen that $4\left(\sqrt{L_c^3}-\sqrt{L_c}\right)$ $\mathrm{c}-+\mathrm{iSWAPs}$, $4\left(\sqrt{L_c^3}-\sqrt{L_c}\right)$ $\mathrm{c}--\mathrm{iSWAPs}$, $8\left(L_c-\sqrt{L_c}\right)$ $\mathrm{c}-\mathbb{H}$, $4\left(L_c-\sqrt{L_c}\right)$ $\mathrm{c}-\mathbb{J}$, $4\left(L_c-\sqrt{L_c}\right)$ $\mathrm{c}-\mathbb{J}^{\dagger}$, $4\left(L_c-\sqrt{L_c}\right)$ $\mathrm{c}-R^{\Theta}_{\sigma_x}$ and $4\left(L_c-\sqrt{L_c}\right)$ $\mathrm{c}-R^{\Theta}_{\sigma_y}$ are required to exactly implement the evolution of $\mathcal{H}_{\mathrm{kin}}$. It may be possible to reduce these numbers by some constant factor if the whole sequence is precompiled and trivially canceling operations are removed. The alternance of the positive and negative variants of the $\mathrm{c}-\mathrm{iSWAP}$ gates enforces the anti-commutativity of the fermionic terms. The main difficulties of the FHM arise from the fact that $[H_{\mathrm{kin}},H_{\mathrm{int}}]\neq 0$, a Trotter-Suzuki approximation must be used to evolve both terms at the same time.

4.3.2.4 *S-wave pairing terms*

To verify that the $(U<0)$ FHM supports s-wave superconductivity, a variational singlet pairing term can be introduced as

$$\begin{aligned}\mathcal{H}_{\mathrm{s-pair}} &= \Delta_s'\sum_i\left(c^{\dagger}_{i\uparrow}c^{\dagger}_{i\downarrow}+c_{i\downarrow}c_{i\uparrow}\right)\\ &= \Delta_s'\sum_{i=1}^{L_c}\mathbb{D}_{L_c}\left(i\right),\end{aligned}\tag{4.16}$$

where the $\mathbb{D}_{L_c}\left(i\right)$ strings are given by 4.8. From figures 4.7a and 4.7b, it can seen that $2L_c$ $\mathrm{c}-+\mathrm{iSWAPs}$, $2L_c$ $\mathrm{c}--\mathrm{iSWAPs}$, $2L_c$ $\mathrm{c}-\mathbb{H}$, L_c $\mathrm{c}-\mathbb{J}$, L_c $\mathrm{c}-\mathbb{J}^{\dagger}$, L_c $\mathrm{c}-R^{\Theta}_{\sigma_x}$ and L_c $\mathrm{c}-R^{\Theta}_{\sigma_y}$ are required to implement the evolution of $\mathcal{H}_{\mathrm{s-pair}}$. The $\mathrm{c}-\mathrm{SQGs}$ are all operated on spin-$\uparrow$ orbitals.

4.3.2.5 *D-wave pairing terms*

A superconducting $d_{x^2-y^2}$ singlet pairing term takes the form [56]

$$\begin{aligned}\mathcal{H}_{\mathrm{d_{x^2-y^2}}} &= \Delta_d'\sum_{\langle i,j\rangle}\frac{d_{ij}}{2}\left(c^{\dagger}_{i\uparrow}c^{\dagger}_{j\downarrow}-c^{\dagger}_{i\downarrow}c^{\dagger}_{j\uparrow}+c_{j\downarrow}c_{i\uparrow}-c_{j\uparrow}c_{i\downarrow}\right)\\ &= \Delta_d'\sum_{\langle i,j\rangle}\frac{d_{ij}}{2}\left(\mathbb{D}_{L_c\uparrow}\left(i,j\right)-\mathbb{D}_{L_c\downarrow}\left(i,j\right)\right)\end{aligned}\tag{4.17}$$

between nearest-neighbor site, where $\mathbf{R}$ are the vector positions of the sites in the cluster in units of a and

$$d_{ij}=\begin{cases}1 & \text{if } \mathbf{R}_i-\mathbf{R}_j=\pm a\mathbf{e_x}\\ -1 & \text{if } \mathbf{R}_i-\mathbf{R}_j=\pm a\mathbf{e_y}\\ 0 & \text{otherwise.}\end{cases}\tag{4.18}$$

The $\mathbb{D}_{L_c\sigma}\left(i,j\right)$ strings are given by 4.7. From figures 4.8a, 4.8b and 4.8c, it can seen that $4\left(\sqrt{L_c^3}+L_c-2\sqrt{L_c}\right)$ $\mathrm{c}-+\mathrm{iSWAPs}$, $4\left(\sqrt{L_c^3}+L_c-\sqrt{L_c}\right)$

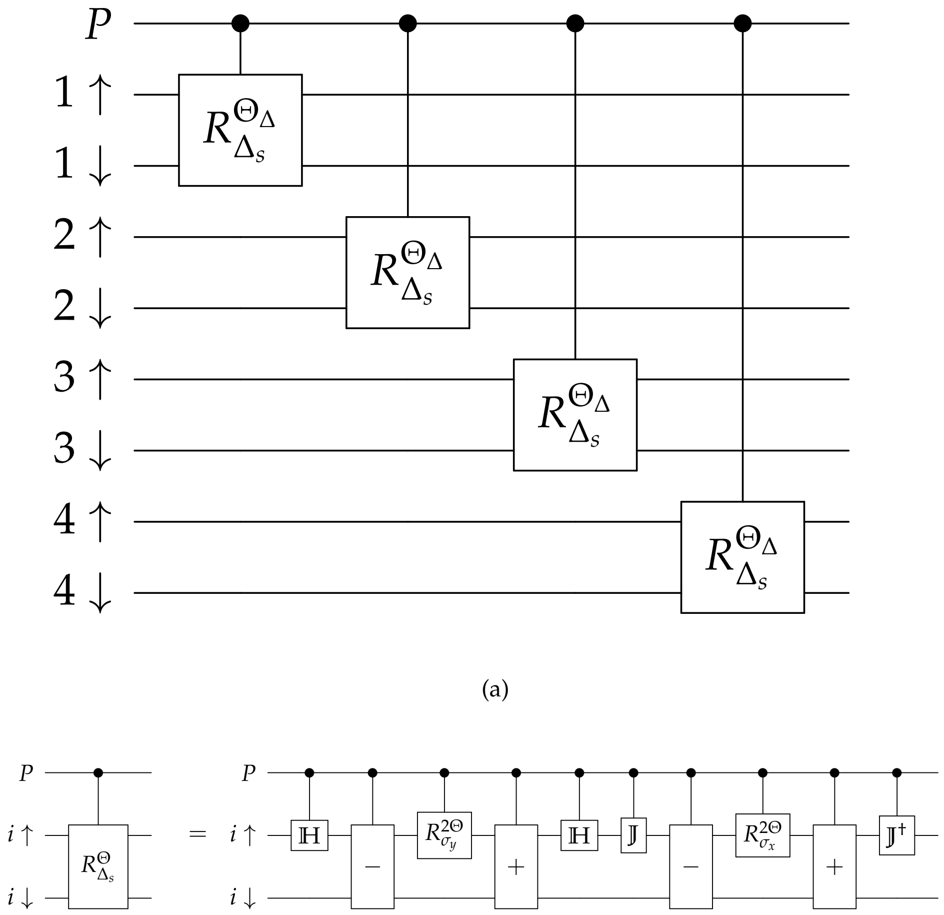
P
1 ↑
1 ↓
2 ↑
2 ↓
3 ↑
3 ↓
4 ↑
4 ↓
$R^{\Theta_\Delta}_{\Delta_s}$
i ↑
i ↓
$R^{\Theta}_{\Delta_s}$
=
ℍ
−
$R^{2\Theta}_{\sigma_y}$
+
𝕁
$R^{2\Theta}_{\sigma_x}$
$𝕁^\dagger$

(a)

(b)

Figure 4.7: In (a), the s-wave pairing terms of the cluster Hamiltonian corresponding to $\mathcal{H}_{\text{s-pair}}$ are decomposed into gates. The angle $\Theta_\Delta \equiv -\Delta\tau\Delta_s'$. There are L_c terms like these in a square lattice. In (b) , the decomposition of c$-R^{\Theta}_{\Delta_s}$ in a site subspace (spin ↑/↓). There are L_c terms like these in a square cluster. The single-qubit rotation gates $R^{\Theta}_{\sigma_x} \equiv e^{-i\Theta\sigma_x}$ and $R^{\Theta}_{\sigma_y} \equiv e^{-i\Theta\sigma_y}$. There are 6 c − SQGs and 4 c − ±iSWAPs per c$-R^{\Theta}_{\Delta_s}$.

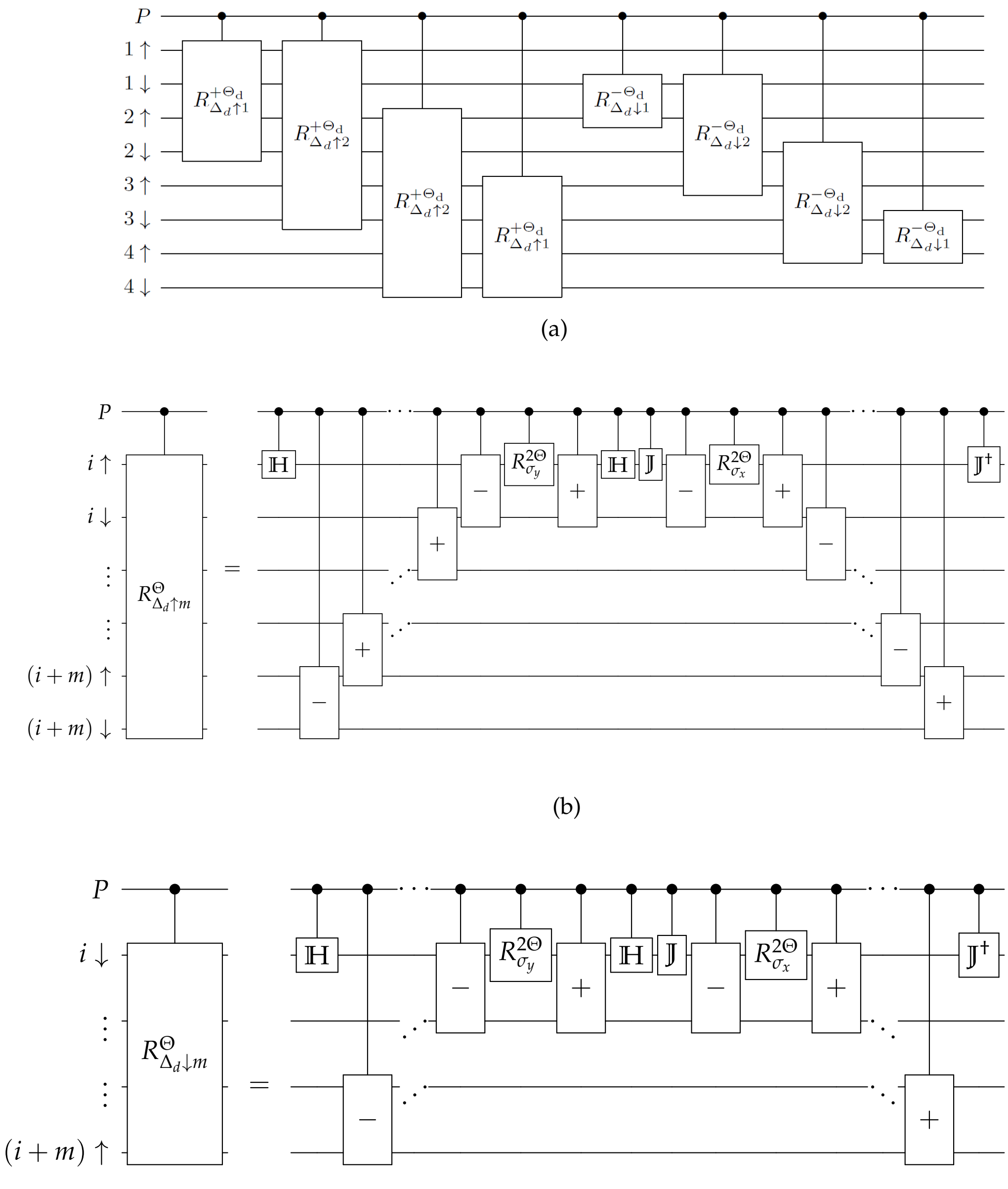
P
1 ↑
1 ↓
2 ↑
2 ↓
3 ↑
3 ↓
4 ↑
4 ↓
$R^{+\Theta_d}_{\Delta_d\uparrow1}$
$R^{+\Theta_d}_{\Delta_d\uparrow2}$
$R^{+\Theta_d}_{\Delta_d\uparrow2}$
$R^{+\Theta_d}_{\Delta_d\uparrow1}$
$R^{-\Theta_d}_{\Delta_d\downarrow1}$
$R^{-\Theta_d}_{\Delta_d\downarrow2}$
$R^{-\Theta_d}_{\Delta_d\downarrow2}$
$R^{-\Theta_d}_{\Delta_d\downarrow1}$
(a)
P
i ↑
i ↓
(i + m) ↑
(i + m) ↓
$R^{\Theta}_{\Delta_d\uparrow m}$
=
ℍ
−
+
$R^{2\Theta}_{\sigma_y}$
𝕁
$R^{2\Theta}_{\sigma_x}$
$\mathbb{J}^{\dagger}$
(b)
P
i ↓
(i + m) ↑
$R^{\Theta}_{\Delta_d\downarrow m}$
=
ℍ
−
+
$R^{2\Theta}_{\sigma_y}$
𝕁
$R^{2\Theta}_{\sigma_x}$
$\mathbb{J}^{\dagger}$

(c)

Figure 4.8: In (a), the d-wave pairing terms of the cluster Hamiltonian corresponding to the time evolution of $\mathcal{H}_{\mathrm{d}_{x^2-y^2}}$ are decomposed into gates. The angle $\Theta_{\mathrm{d}} \equiv -\Delta\tau\Delta'_d$. There are $4\left(L_c - \sqrt{L_c}\right)$ terms like these in a square lattice. One quarter of those strings have length 2, another quarter has length 4, another quarter has length $2\sqrt{L_c}$ and the last quarter has length $2\left(\sqrt{L_c}-1\right)$. In (b), the decomposition of c$-R^{\Theta}_{\Delta_d\uparrow m}$ in a subspace starting at $i\uparrow$ and ending at $i+m\downarrow$ is shown, where $m = 1$ or $\sqrt{L_c}$ in a square lattice. There are 6 c − SQGs and $4m+4$ c − ±iSWAPs per c$-R^{\Theta}_{\Delta_d\uparrow m}$. In (c), the decomposition of c$-R^{\Theta}_{\Delta_d\downarrow m}$ in a subspace starting at $i\downarrow$ and ending at $i+m\uparrow$ is shown, where $m = 1$ or $\sqrt{L_c}$ in a square lattice. There are 6 c − SQGs and $4m$ c − ±iSWAPs per c$-R^{\Theta}_{\Delta_d\downarrow m}$.

c $-$ $-$iSWAPs , $8\left(L_c-\sqrt{L_c}\right)$ c$-\mathbb{H}$, $4\left(L_c-\sqrt{L_c}\right)$ c$-\mathbb{J}$, $4\left(L_c-\sqrt{L_c}\right)$ c$-\mathbb{J}^\dagger$, $4\left(L_c-\sqrt{L_c}\right)$ c$-R^{\Theta}_{\sigma_x}$ and $4\left(L_c-\sqrt{L_c}\right)$ c$-R^{\Theta}_{\sigma_y}$ are required to implement the evolution of $\mathcal{H}_{\mathrm{d}_{\mathrm{x}^2-\mathrm{y}^2}}$. It may be possible to reduce these numbers by some constant factor if the whole sequence is precompiled and trivially canceling operations are removed. Interestingly, $\left[\mathcal{H}_{\mathrm{kin}},\mathcal{H}_{\mathrm{d}_{\mathrm{x}^2-\mathrm{y}^2}}\right]=0$ and the two terms of the cluster can be grouped together to simulate their exact evolution.

4.3.3 *The Trotter-Suzuki approximation*

Typically, the terms of the cluster Hamiltonian (2.22) do not commute and a Trotter-Suzuki approximation [94, 123, 125] must be used. Here is the procedure to make the mapping that requires no oracle black box for $\mathcal{H}'$. The Hamiltonian (2.22) is broken into M non-commuting parts such that

$$\mathcal{H}'=\sum_{i=1}^{M}\mathcal{H}'_i. \tag{4.19}$$

Each time-step $\Delta\tau$ evolution of the cluster Hamiltonian can be simulated with n_T Trotter-Suzuki steps

$$e^{-i\mathcal{H}'\Delta\tau}\simeq\left(\prod_{i=1}^{M}e^{-\frac{i\mathcal{H}'_i\Delta\tau}{n_T}}\right)^{n_T}+\sum_{i<j}\frac{\left[\mathcal{H}'_i,\mathcal{H}'_j\right]\Delta\tau^2}{2n_T}+\dots. \tag{4.20}$$

It should be noted that those time-steps set the upper bound in the simulated energy spectrum which should scale as $\omega_{\mathrm{max}}\propto\frac{1}{\Delta\tau}$, while the lowest energy should scale at the inverse of the total simulation time.

The cluster Hamiltonian $\mathcal{H}'$ has 3 non-commuting blocks: $\mathcal{H}_z\equiv\mathcal{H}_{\mathrm{local}}+\mathcal{H}_{\mathrm{int}}-\mathcal{H}_{AF}$, $\mathcal{H}_{\mathrm{kin}}+\mathcal{H}_{\mathrm{d}_{\mathrm{x}^2-\mathrm{y}^2}}$ and $\mathcal{H}_{\mathrm{s-pair}}$, the commutation relations are given in table (4.1). The time evolution of each time block can be done exactly. The blocks containing nearest-neighbor operators ($\mathcal{H}_{\mathrm{kin}}$ and $\mathcal{H}_{\mathrm{d}_{\mathrm{x}^2-\mathrm{y}^2}}$) are the most expensive in terms of gates. If D is the dimension of the lattice, then these blocks require the application of $O\left(L_c^{\frac{2D-1}{D}}\right)$ c $-$ ±iSWAPs, so it is advisable to minimize the use of these blocks in the Trotter-Suzuki decomposition. The number of gates to implement the local interaction terms ($\mathcal{H}_z$ and $\mathcal{H}_{\mathrm{s-pair}}$) scales as $O\left(L_c\right)$.

The worst-case Trotter-Suzuki decomposition arises when all variational parameters have a non-zero value at some point during the

$[\bullet,\bullet]$	$\mathcal{H}_{\text{local}}$	$\mathcal{H}_{\text{int}}$	$\mathcal{H}_{AF}$	$\mathcal{H}_{\text{kin}}$	$\mathcal{H}_{\text{s-pair}}$	$\mathcal{H}_{\text{d}_{\text{x}^2-\text{y}^2}}$
$\mathcal{H}_{\text{local}}$	0	0	0	0	$-2\mathcal{H}_D$	$-2\mathcal{H}_F$
$\mathcal{H}_{\text{int}}$	0	0	0	$-2\mathcal{H}_A$	$-\mathcal{H}_E$	$-2\mathcal{H}_G$
$\mathcal{H}_{AF}$	0	0	0	$-2\mathcal{H}_B$	0	$-2\mathcal{H}_H$
$\mathcal{H}_{\text{kin}}$	0	$2\mathcal{H}_A$	$2\mathcal{H}_B$	0	$\mathcal{H}_C$	0
$\mathcal{H}_{\text{s-pair}}$	$2\mathcal{H}_D$	$\mathcal{H}_E$	0	$-\mathcal{H}_C$	0	0
$\mathcal{H}_{\text{d}_{\text{x}^2-\text{y}^2}}$	$2\mathcal{H}_F$	$2\mathcal{H}_G$	$2\mathcal{H}_H$	0	0	0

Table 4.1: Commutation relations of the different Hamiltonian terms (2×2 cluster). $\mathcal{H}_A$ to $\mathcal{H}_H$ represent different non-zero commutators.

saddle-point search. In this case a single Trotter-Suzuki step could be decomposed as

$$\begin{aligned} & e^{-i\mathcal{H}'\Delta\tau} \\ \approx\ & e^{-i\mathcal{H}_z\frac{\Delta\tau}{4}} \cdot e^{+i\mathcal{H}_{\text{s-pair}}\frac{\Delta\tau}{2}} \cdot e^{-i\mathcal{H}_z\frac{\Delta\tau}{4}} \cdot e^{+i\mathcal{H}_{\text{d}_{\text{x}^2-\text{y}^2}}\Delta\tau} \cdot e^{-i\mathcal{H}_{\text{kin}}\Delta\tau} \dots \\ & \dots \cdot e^{-i\mathcal{H}_z\frac{\Delta\tau}{4}} \cdot e^{+i\mathcal{H}_{\text{s-pair}}\frac{\Delta\tau}{2}} \cdot e^{-i\mathcal{H}_z\frac{\Delta\tau}{4}} \end{aligned} \tag{4.21}$$

Ruth's formula [125, 126] can also be used recursively

$$\begin{aligned} & e^{-i\Delta\tau(A+B)+O\left(\Delta\tau^4\right)} \\ =\ & e^{-i\frac{7}{24}\Delta\tau A} e^{-i\frac{2}{3}\Delta\tau B} e^{-i\frac{3}{4}\Delta\tau A} e^{+i\frac{2}{3}\Delta\tau B} e^{+i\frac{1}{24}\Delta\tau A} e^{-i\Delta\tau B} \end{aligned} \tag{4.22}$$

by replacing A and B by the correct cluster Hamiltonian terms. Ruth's formula is more precise but has a larger overhead in terms of gate count. In a Trotter-Suzuki step, the hopping term $e^{-i\mathcal{H}_{\text{kin}}\Delta\tau}$ and $e^{+i\mathcal{H}_{\text{d}_{\text{x}^2-\text{y}^2}}\frac{\Delta\tau}{2}}$ appear once, the s-wave pairing term $e^{+i\mathcal{H}_{\text{s-pair}}\frac{\Delta\tau}{4}}$ has two instances and the simple local $e^{-i\mathcal{H}_z\frac{\Delta\tau}{8}}$ appears four times. Figure 4.9 provides a practical effective bound on the error by looking at an extreme case of non-commuting variational parameters all applied at the same time. The error is given for a fixed evolution time by a varying step size. A step size $\Delta\tau < 10^{-2}$ achieve an error $\sim 10^{-5}$ using a recursive Trotter-Suzuki formula and an error $\sim 10^{-10}$ using a recursive Ruth formula. Not considering all variational parameters at the same time significantly reduces the length of the decomposition.

4.4 SCALING TO LARGER CLUSTERS

The resource requirements of the algorithm are given in table 4.2 by giving examples for the 1D, 2D and 3D FHM. The 1D model can be solved analytically and can be used as a benchmark. The 3D model is meant to show that the method scales to higher dimensions. All resources only include the P and S registers, the scaling of registers R and B are analyzed in details in [108]. While the size of the Hilbert

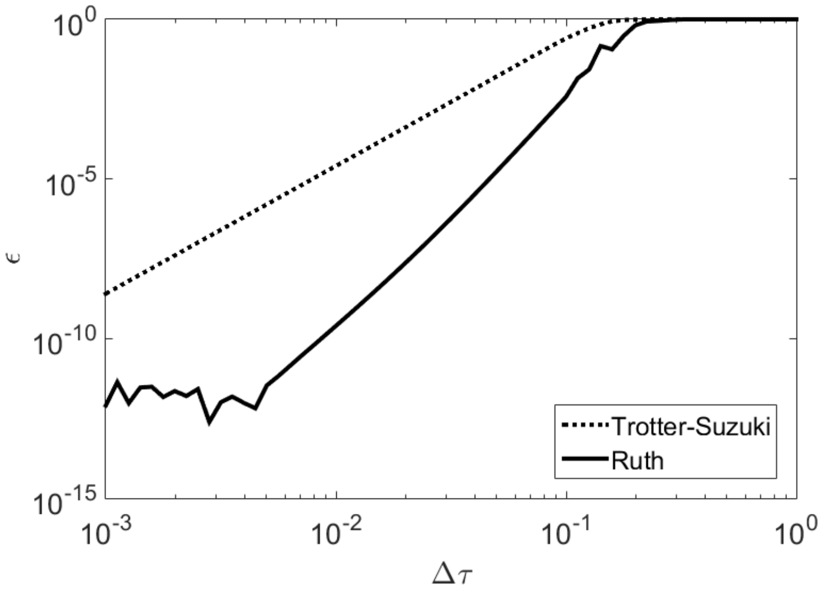

Figure 4.9: Numerical worst case error $\epsilon(\Delta\tau) = 1 - \frac{1}{16^{L_c}}\left|\mathrm{Tr}\left[U_{\mathrm{TS}}(N\Delta\tau)\, U^{\dagger}(N\Delta\tau)\right]\right|^2$for the Trotter-Suzuki (dotted line, order $O\left(\Delta\tau^3\right)$) and the Ruth (plain line, order $O\left(\Delta\tau^4\right)$) decompositions for a constant simulation time such that $\tau = N\Delta\tau = 3$. To emulate a typical worst-case error, all variational parameters $\mu' = M' = \Delta_s' = \Delta_d' = 3$. The interaction $U = 8$ and all energy and time units are made unitless by referencing them to the hopping energy $t = 1$.

Dimension(s)	Size	Orbitals (singlets) [n]	Dim. of Hilbert space [2^n]	Qubits required [$n+1$]	Measured correl. functions [$< 4n^2$]	$c -$ SQGs to tune [$7n$]	$c - \pm$iSWAPs to tune [$2n-2$]	Gates / Trotter-Suzuki step (hopping terms)
1D	2	4	16	5	64	28	6	24
1D	3	6	64	7	144	42	10	48
1D	4	8	256	9	256	56	14	72
2D	2×2	8	256	9	256	56	14	96
2D	3×3	18	$262,144$	19	$1,296$	126	34	336
2D	4×4	32	$4,294,967,296$	33	$4,096$	224	62	768
3D	$2 \times 2 \times 2$	16	$65,536$	17	$1,024$	112	30	416
3D	$3 \times 3 \times 3$	54	1.8×10^{16}	55	$11,664$	378	106	$2,736$
3D	$4 \times 4 \times 4$	128	3.4×10^{38}	129	$65,536$	896	254	$10,368$

Table 4.2: Quantum resources required to solve a cluster of the FHM once the Gibbs state is prepared. The information processed by the classical computer is proportional to the number of measured correlation functions which scales quadratically with the number of orbitals in the cluster.

space required to store the density matrix scales exponentially with the number of spin orbitals, the number of qubits required in register S scales linearly. The number of correlation functions to measure, which corresponds to the amount of classical information to extract from the quantum simulator, scales quadratically with the size of the cluster.The number of conditional single-qubits gates and the number of $\mathrm{c}-\pm$iSWAPs that have to be benchmarked and tuned also scales linearly with the size of the system, which is a significant technical advantage. Finally, the number of $\mathrm{c}-\pm$iSWAPs in terms with nearest-neighbor couplings (like hopping or d-wave superconductivity) scales sub-quadratically as $O\left(L_c^{\frac{2D-1}{D}}\right)$, where D is the dimension of the system.

4.5 CONCLUSION

The FHM contains the essential features of many strongly correlated electronic systems. We recently proposed a method to compute the properties of the FHM using a hybrid quantum-classical approach. In this chapter we looked more closely at the scaling properties of the quantum part of the algorithm by giving an explicit gate decomposition of the time evolution of the cluster Hamiltonian and bounding expected Trotter-Suzuki errors. The main results are the following:

1. It scales linearly in memory: 1 spin orbital corresponds to 1 qubit.
2. It scales favorably in number of measurements which are proportional to L_c^2 at worst.
3. The number of time measurements determines precision in frequency space (same as classical, decoherence means less information, “good enough” is possible).
4. The most difficult terms require $O\left(L_c^{\frac{2D-1}{D}}\right)$ $\mathrm{c}-\pm$iSWAPs (the longest gate).
5. Trotter-Suzuki errors can be made as small as desired.
6. The proposed architecture has no crossing interaction lines whose number scales as $O\left(L_c\right)$ with no long range interaction required.
7. The number of gates that need to be tuned scales as $O\left(L_c\right)$.

To fully benchmark the algorithm, a full simulation will have to be implemented to analyze the gate count in the Gibbs state preparation. A more careful analysis of errors also has to be done as the effect of errors may not be the same depending if they appear in the R, P or $S+B$ registers. Finally, an adiabatic or annealing scheme could be used to replace the Gibbs state preparation if only zero-temperature states are studied [112]. In this case, the correlation function measurements would still stay the same as the rest of the classical method.

CONCLUSION

In chapter 1, it was shown how the Nambu notation is used to integrate the phenomenological description of macroscopic quantum coherence in the microscopic theory of superconductivity as off-diagonal long-range order. The different nature of high temperature cuprate superconductors was contrasted with standard BCS superconductors to introduce the FHM. In chapter 2, the FHM was explained in more detail. The SFT and VCA methods were introduced with examples of numerical calculations at finite temperature. The scaling in classical memory usage was shown to be analoguous to the classical simulation of quantum computers. In chapter 3, I described how a VCA cluster can be mapped to a quantum register. Single-particle correlation functions can be extracted in a scalable manner from a general quantum processor and used in the classical SFT loop to compute observables of the FHM and other correlated models. In chapter 4, I introduced a practical planar architecture for quantum simulators. The gate count and decomposition is used to show that the algorithm scales and can be used to solve other strongly correlated problems.

Many avenues remain to be explored. First, quantum control schemes to implement the ±iFredkin gates are expected to be very helpful in the next step, which is to specify a superconducting circuit implementation of the quantum simulator architecture. From the SFT litterature, one can expect that similar schemes for non-equilibrium many-body physics and gauge theories can be found. The connection, if any, to the quantum simulation of quantum chemistry can also be investigated. Bayesian methods can probably be used to significantly reduce the classical overhead involved in searching the saddle-point of the SFT. On the algorithmic side, there may be a straightforward generalization of the correlation function measurement procedure to n-point correlation functions. The Gibbs state preparation procedure needs to be benchmarked against decoherence in a simulated quantum computing environment.

As a last and more conceptual note, it seems that giving away the complete wavefunction picture for the description of materials (or large proteins) can be advantageous as a complete prescription involves too much classical information. Sampling correlation functions seems to be the key to large scale quantum simulations as they yield most of the useful practical information. As quantum simulations were the reason Feynman thought about quantum computers, they may also yield the first experimental demonstration of quantum supremacy even if building a logical qubit with infinite coherence time happens to be an impossible task.

APPENDIX

A

NUMERICAL EXAMPLE ON THE 1D CHAIN

The simplest experimental implementation of the variational procedure on a quantum computer would correspond to solving a simple 1D tight-binding chain. With a minimum cluster of $L_c = 2$ sites (labeled "1" and "2") each with 2 electrons (spin-up and spin-down), a 5-qubit quantum computer would be sufficient to extract the correlations functions (3.22). This section shows in detail how the formalism of subsection 3.3.2 can be used to compute the band structure and its occupation for the 1D chain at arbitrary μ and T. The simulation was restricted only to a chemical variational potential μ' and a simple pairing potential Δ' which is expected to be zero in the case of one dimension.

A.1 FINDING THE SADDLE-POINT OF THE SELF-ENERGY FUNCTIONAL

First, the saddle point $\begin{pmatrix} \mu'_* \\ \Delta'_* \end{pmatrix}$ of equation (2.33) must be found. This is done through the following sequence:

1. *Choose a point* $\begin{pmatrix} \mu'_1 \\ \Delta'_1 \end{pmatrix}$ *and its neighbors* $\begin{pmatrix} \mu'_1 \pm h \\ \Delta'_1 \end{pmatrix}$ *and* $\begin{pmatrix} \mu'_1 \\ \Delta'_1 \pm h \end{pmatrix}$ *(with h a small parameter).*
2. *On a quantum computer, measure the retarded Nambu Green's function* $\hat{\mathbf{G}}'^R(\tau, \mu', \Delta')$ *of the cluster for the points of step 1 (as described in section 3.3).*
3. *Numerically compute the square of the gradient* (2.33)*. If the modulus of the gradient is smaller than some threshold* ϵ_Ω*, stop and assign* $\begin{pmatrix} \mu'_* \\ \Delta'_* \end{pmatrix} = \begin{pmatrix} \mu'_i \\ \Delta'_i \end{pmatrix}$.
4. *Using a numerical Newton-Raphson method [127], pick the next point* $\begin{pmatrix} \mu'_{i+1} \\ \Delta'_{i+1} \end{pmatrix}$ *and loop over to step 1.*

Once the saddle-point is known, $\hat{\mathbf{G}}'^R(\tau, \mu'_*, \Delta'_*)$ is measured and properties like the spectral density of the lattice can be approximated.

A.2 MEASURING AND CALCULATING THE RETARDED GREEN'S FUNCTION OF THE CLUSTER

The retarded Nambu Green's function is measured on a discrete time domain $\tau_n = n\Delta\tau$ where n is an integer between 0 and n_{max} and $\Delta\tau$ is a small time interval ($n_{\text{max}} = 2000$ and $\Delta\tau = 0.05$ in this example) such that $\tau_{\text{max}} = n_{\text{max}}\Delta\tau$. The matrix form of $\hat{\mathbf{G}}'^R$ clearly shows that the number of correlation functions $\left\langle c_\nu\left(\tau\right) c^\dagger_\mu\left(0\right)\right\rangle$ scales as $4L_c^2$:

$$
\begin{aligned}
&\hat{\mathbf{G}}'^R\left(\tau_n\right)\\
&= \quad -i\theta(\tau_n)\begin{pmatrix}
\left\langle c_{1\uparrow}\left(\tau_n\right) c^\dagger_{1\uparrow}\left(0\right)\right\rangle & \left\langle c_{1\uparrow}\left(\tau_n\right) c^\dagger_{2\uparrow}\left(0\right)\right\rangle & \left\langle c_{1\uparrow}\left(\tau_n\right) c_{1\downarrow}\left(0\right)\right\rangle & \left\langle c_{1\uparrow}\left(\tau_n\right) c_{2\downarrow}\left(0\right)\right\rangle \\
\left\langle c_{2\uparrow}\left(\tau_n\right) c^\dagger_{1\uparrow}\left(0\right)\right\rangle & \left\langle c_{2\uparrow}\left(\tau_n\right) c^\dagger_{2\uparrow}\left(0\right)\right\rangle & \left\langle c_{2\uparrow}\left(\tau_n\right) c_{1\downarrow}\left(0\right)\right\rangle & \left\langle c_{2\uparrow}\left(\tau_n\right) c_{2\downarrow}\left(0\right)\right\rangle \\
\left\langle c^\dagger_{1\downarrow}\left(\tau_n\right) c^\dagger_{1\uparrow}\left(0\right)\right\rangle & \left\langle c^\dagger_{1\downarrow}\left(\tau_n\right) c^\dagger_{2\uparrow}\left(0\right)\right\rangle & \left\langle c^\dagger_{1\downarrow}\left(\tau_n\right) c_{1\downarrow}\left(0\right)\right\rangle & \left\langle c^\dagger_{1\downarrow}\left(\tau_n\right) c_{2\downarrow}\left(0\right)\right\rangle \\
\left\langle c^\dagger_{2\downarrow}\left(\tau_n\right) c^\dagger_{1\uparrow}\left(0\right)\right\rangle & \left\langle c^\dagger_{2\downarrow}\left(\tau_n\right) c^\dagger_{2\uparrow}\left(0\right)\right\rangle & \left\langle c^\dagger_{2\downarrow}\left(\tau_n\right) c_{1\downarrow}\left(0\right)\right\rangle & \left\langle c^\dagger_{2\downarrow}\left(\tau_n\right) c_{2\downarrow}\left(0\right)\right\rangle
\end{pmatrix}.
\end{aligned}
\tag{A.1}
$$

It is then Fourier transformed on a discrete frequency domain $\omega_m = m\Delta\omega$ between $-\omega_{\text{max}}$ and ω_{max} chosen such that $\omega_{\text{max}} = \frac{1}{2\Delta\tau}$ and $\Delta\omega = \frac{1}{2\tau_{\text{max}}}$:

$$
\hat{\mathbf{G}}'^R\left(\omega_m\right) = \frac{\Delta\tau}{2\pi}\sum_{n=0}^{n_{\text{max}}} e^{-i\omega_m\tau_n}\hat{\mathbf{G}}'^R\left(\tau_n\right). \tag{A.2}
$$

The numerical $\hat{\mathbf{G}}'^R\left(\omega\right)$ can then be used to compute the lattice-perturbed Green's function $\hat{\mathcal{G}}\left(\tilde{\mathbf{k}},\omega\right)$ (see equation (2.48)) and various properties of the lattice as detailed in subsection 2.4.3. The exact mapping of (A.1) on the quantum computer is done through the JWT

$$
\begin{aligned}
c^\dagger_{1\uparrow} &= \mathbb{I}\otimes\mathbb{I}\otimes\mathbb{I}\otimes\sigma_+\\
c^\dagger_{2\uparrow} &= \mathbb{I}\otimes\mathbb{I}\otimes\sigma_+\otimes\sigma_z\\
c^\dagger_{1\downarrow} &= \mathbb{I}\otimes\sigma_+\otimes\sigma_z\otimes\sigma_z\\
c^\dagger_{2\downarrow} &= \sigma_+\otimes\sigma_z\otimes\sigma_z\otimes\sigma_z.
\end{aligned}
\tag{A.3}
$$

Using this transformation, all component of the Hamiltonian $\mathcal{H}'$ of the cluster (4.4) are mapped to a 4-qubit Hilbert space:

$$\begin{aligned}
&\mathcal{H}_{\mathrm{FH}} \\
=\ & -t\left(c^{\dagger}_{1\uparrow}c_{2\uparrow}+c^{\dagger}_{2\uparrow}c_{1\uparrow}+c^{\dagger}_{1\downarrow}c_{2\downarrow}+c^{\dagger}_{2\downarrow}c_{\downarrow\uparrow}\right)-U\left(n_{1\uparrow}n_{1\downarrow}+n_{2\uparrow}n_{2\downarrow}\right) \\
=\ & -t\left(\mathbb{I}\otimes\mathbb{I}\otimes\left(\sigma_{-}\otimes\sigma_{+}+\sigma_{+}\otimes\sigma_{-}\right)+\left(\sigma_{-}\otimes\sigma_{+}+\sigma_{+}\otimes\sigma_{-}\right)\otimes\mathbb{I}\otimes\mathbb{I}\right) \\
& -U\left(\mathbb{I}\otimes\sigma_{n}\otimes\mathbb{I}\otimes\sigma_{n}+\sigma_{n}\otimes\mathbb{I}\otimes\sigma_{n}\otimes\mathbb{I}\right),
\end{aligned} \tag{A.4}$$

$$\begin{aligned}
&\mathcal{H}_{\mathrm{pair}} \\
=\ & \Delta'\left(c^{\dagger}_{1\uparrow}c^{\dagger}_{1\downarrow}+c_{1\downarrow}c_{1\uparrow}+c^{\dagger}_{2\uparrow}c^{\dagger}_{2\downarrow}+c_{2\downarrow}c_{2\uparrow}\right) \\
=\ & \Delta'\left(\mathbb{I}\otimes\left(\sigma_{+}\otimes\sigma_{z}\otimes\sigma_{+}+\sigma_{-}\otimes\sigma_{z}\otimes\sigma_{-}\right)+\left(\sigma_{+}\otimes\sigma_{z}\otimes\sigma_{+}+\sigma_{-}\otimes\sigma_{z}\otimes\sigma_{-}\right)\otimes\mathbb{I}\right),
\end{aligned} \tag{A.5}$$

$$\begin{aligned}
&\mathcal{H}_{\mathrm{local}} \\
=\ & \mu'\left(n_{1\uparrow}+n_{2\uparrow}+n_{1\downarrow}+n_{2\downarrow}\right) \\
=\ & \mu'\left(\mathbb{I}\otimes\mathbb{I}\otimes\mathbb{I}\otimes\sigma_{n}+\mathbb{I}\otimes\mathbb{I}\otimes\sigma_{n}\otimes\mathbb{I}+\mathbb{I}\otimes\sigma_{n}\otimes\mathbb{I}\otimes\mathbb{I}+\sigma_{n}\otimes\mathbb{I}\otimes\mathbb{I}\otimes\mathbb{I}\right).
\end{aligned} \tag{A.6}$$

It can be noticed that the standard FHM term requires gates between two qubits, the variational chemical potential can be implemented with single qubit gates but the pairing terms need operations over several qubits to maintain the statistics of the fermions. The perturbation matrix (2.40) is given explicitly by

$$\hat{\mathbf{V}}\left(\tilde{\mathbf{k}}\right)=\begin{pmatrix} -\mu+\mu' & \epsilon\left(\tilde{k}\right)+t & -\Delta' & 0 \\ \epsilon^{*}\left(\tilde{k}\right)+t & -\mu+\mu' & 0 & -\Delta' \\ -\Delta' & 0 & \mu-\mu' & -\epsilon\left(\tilde{k}\right)-t \\ 0 & -\Delta' & -\epsilon^{*}\left(\tilde{k}\right)-t & \mu-\mu' \end{pmatrix}. \tag{A.7}$$

Finally the operators that are applied in the phase estimation part of the algorithm and are required in the reconstruction of (A.1) are given by the following transformations:

$$
\begin{aligned}
X_{1\uparrow} &= c_{1\uparrow} + c_{1\uparrow}^{\dagger} & Y_{1\uparrow} &= -i\left(c_{1\uparrow} - c_{1\uparrow}^{\dagger}\right) \\
&= \tfrac{1}{2}\mathbb{I}\otimes\mathbb{I}\otimes\mathbb{I}\otimes\sigma_x & &= \tfrac{1}{2}\mathbb{I}\otimes\mathbb{I}\otimes\mathbb{I}\otimes\sigma_y \\
X_{2\uparrow} &= c_{2\uparrow} + c_{2\uparrow}^{\dagger} & Y_{2\uparrow} &= -i\left(c_{2\uparrow} - c_{2\uparrow}^{\dagger}\right) \\
&= \tfrac{1}{2}\mathbb{I}\otimes\mathbb{I}\otimes\sigma_x\otimes\sigma_z & &= \tfrac{1}{2}\mathbb{I}\otimes\mathbb{I}\otimes\sigma_y\otimes\sigma_z \\
X_{1\downarrow} &= c_{1\downarrow} + c_{1\downarrow}^{\dagger} & Y_{1\downarrow} &= -i\left(c_{1\downarrow} - c_{1\downarrow}^{\dagger}\right) \\
&= \tfrac{1}{2}\mathbb{I}\otimes\sigma_x\otimes\sigma_z\otimes\sigma_z & &= \tfrac{1}{2}\mathbb{I}\otimes\sigma_y\otimes\sigma_z\otimes\sigma_z \\
X_{2\downarrow} &= c_{2\downarrow} + c_{2\downarrow}^{\dagger} & Y_{2\downarrow} &= -i\left(c_{2\downarrow} - c_{2\downarrow}^{\dagger}\right) \\
&= \tfrac{1}{2}\sigma_x\otimes\sigma_z\otimes\sigma_z\otimes\sigma_z & &= \tfrac{1}{2}\sigma_y\otimes\sigma_z\otimes\sigma_z\otimes\sigma_z
\end{aligned}
\tag{A.8}
$$

The procedure highlighted in subsection 2.4.2 is then followed to compute the CPT Green's function and the desired properties of the system.

A.3 SIMPLE TIGHT-BINDING MODEL

The tight-binding model $U = 0$ is investigated using the methods of this paper. The goal is to show that the method can accurately simulate well known simple models through the intermediate results it produces.

In figure A.1, the measured value of $P_{\mu\nu}\left(\mathcal{M} = 1, \tau\right)$ is shown for the simplest case of a 2-site tight-binding cluster. In this case the model generates simple oscillations as no decoherence is included.

In figure A.2, the Green's functions ${G'_{\mu\nu}}^{R}\left(\tau\right)$ computed from equation (3.29) are shown. Notice that the time-dependent Green's functions were regularized with an decaying exponential $e^{-\eta\tau}$ in order to remove the fast oscillations coming from the convolution of the frequency-dependent Green's function with the sinc $\left(\frac{\omega\tau_{\max}}{2\pi}\right)$ term involved in finite time measurements. This regularizing term is not decoherence, but it could model a uniform depolarizing rate η in the quantum processor. This rate would actually contribute to the width of the frequency-dependent Green's function.

In figure A.3, the Fourier transformed ${G'_{\mu\nu}}^{R}\left(\omega\right)$ are shown for the simple tight-binding cluster. Only two peaks are present and their width is determined by η and the time domain used to measure the correlation functions.

Figure A.4 shows an example of the Potthoff functional $\Omega\left(\mu', \Delta'\right)$ and its saddle point for a small 1D cluster. As expected for this simple model, the saddle point is almost at the origin, the small deviation comes from the low finite temperature. At the saddle point, the av-

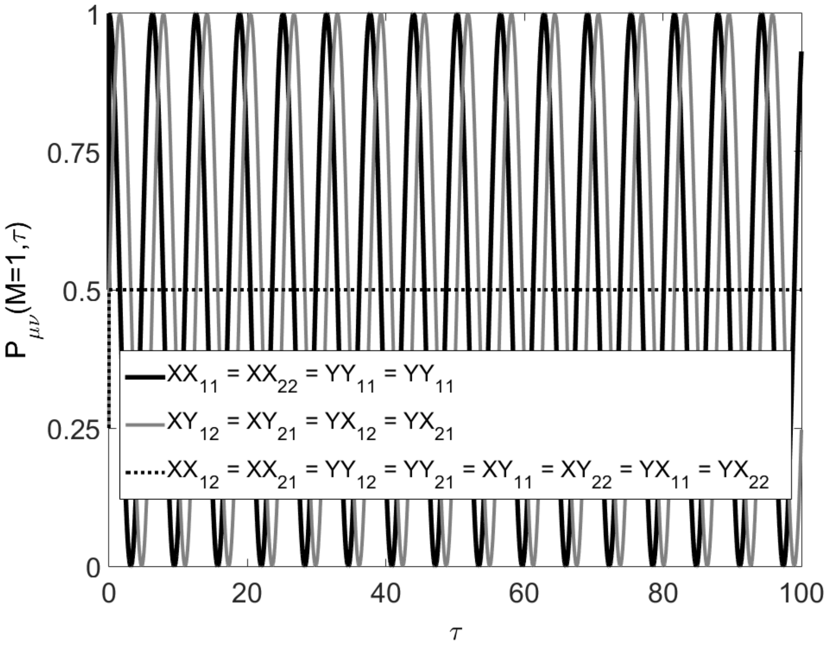

Figure A.1: Measured probabilities for different X_μ and Y_μ at different times. The time axis τ is in units t^{-1} of the hopping energy. In this case the cluster parameters are $L_c = 2$, $t = 1$, $U = \Delta' = \mu' = 0$ and $T = 0.1$.

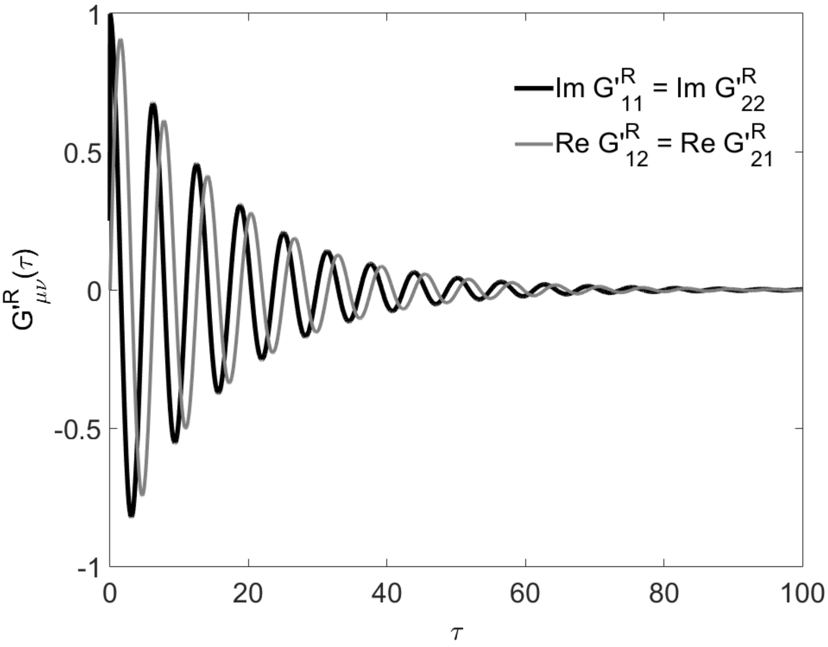

Figure A.2: Non-zero correlation functions computed from the results of figure A.1 with the time in units of t^{-1}. The function was regularized with a $e^{-\eta\tau}$ term to remove the fast oscillations of the Fourier transform arising from the finiteness of the time domain, $\eta = \frac{\pi}{50}$ was used in this case.

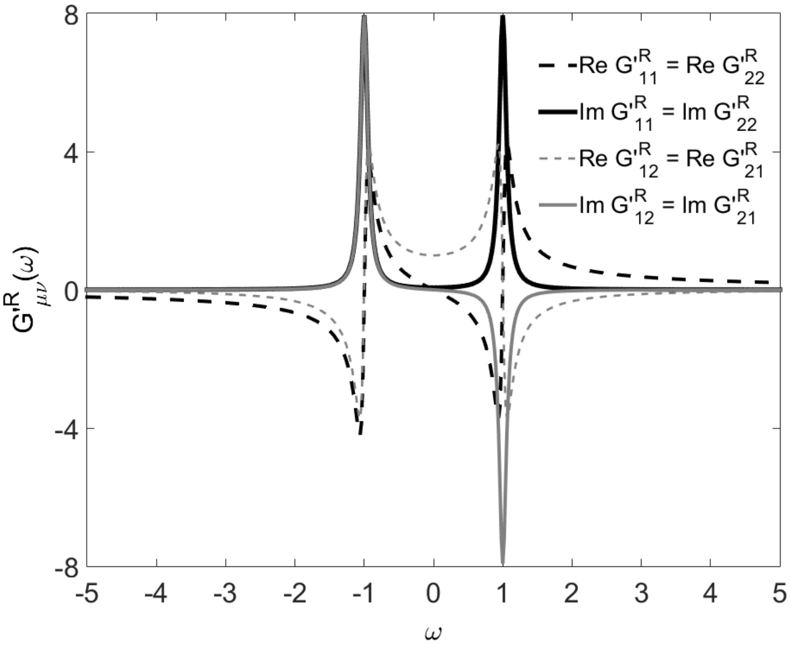

Figure A.3: Real and imaginary parts of the frequency-dependent Green's functions arising from the correlation functions measured in figure A.2. The frequency axis ω is in units of the hopping energy t.

erage occupation of each state is $\langle n \rangle = 0.5$ as is expected. At the saddle-point the spectral density of the full lattice can be computed.

Figure A.5 shows the spectral density $A(k, \omega)$ computed from equation (2.52) for 50 clusters of size $L_c = 2$ in a simple tight binding model at relatively high temperature $T = 1$. The cosine band is filled above the Fermi level because of the high temperature.

Figure A.6 shows that the simulation yields the expected physics of the tight-binding model at finite temperature. The ground state is indeed a 1D Fermi sea in the electronic momentum distribution (2.54) whose width is increased with the chemical potential and broadened by increased temperature. The loss of accuracy in the simulation is attributed to the sampling method and the accuracy of the Fermi distribution on the discrete frequency domain computed from the measured time series.

Finally figure A.7 shows the spectral density $A(k, \omega)$ computed from equation 2.52 for a cluster of size $L_c = 2$ in an attractive Hubbard chain $U = 4$ at low temperature $T = 0.1$. The band is highly distorted by the interaction and the ground state is no longer a $k = 0$ state.

Extending these calculations for more complicated model is an easy task. A simple 2D model with a superconducting phase transition would require 4 sites and 8 electrons, so a 9-qubit quantum computer would be required to measure $\hat{\mathbf{G}}'^{R}(\tau)$ in this case. It appears that

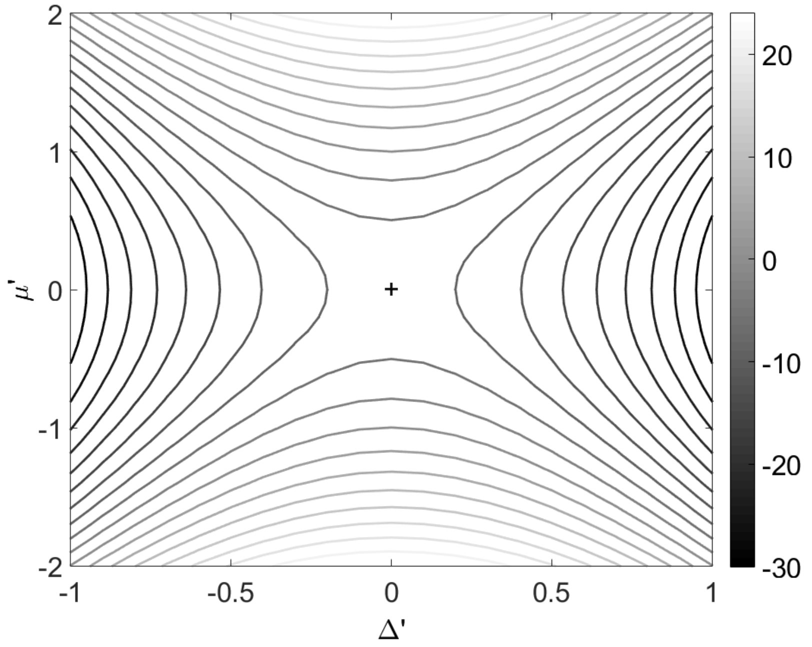

Figure A.4: Potthoff functional Ω for different variational parameters μ' and Δ' of a cluster of size $L_c = 2$ with parameters $t = 1$, $U = 0$, $\mu = 0$ and $T = 1$. The cross marks the saddle point at $\begin{pmatrix} \mu'_* \\ \Delta'_* \end{pmatrix} = \begin{pmatrix} 0.0046 \\ 0 \end{pmatrix}$. All the variational parameters are in units of the hopping energy t.

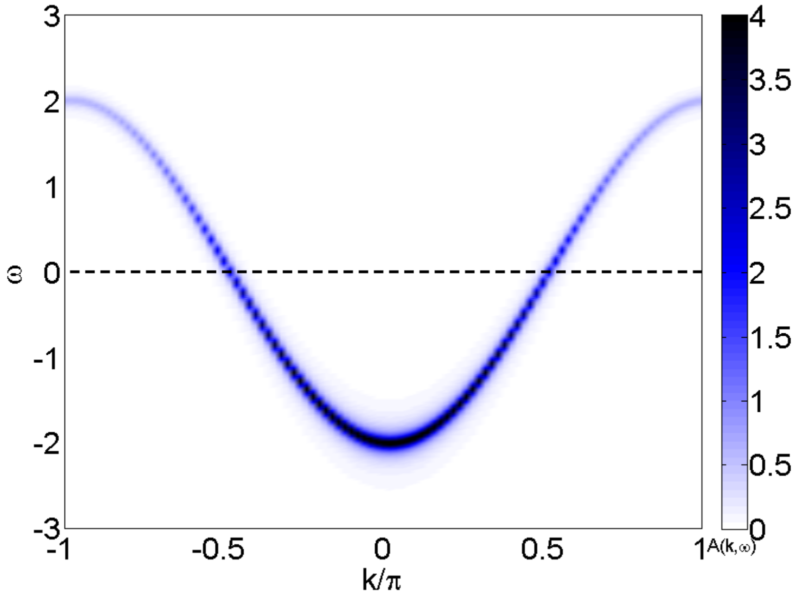

Figure A.5: Electron momentum-frequency distribution $A(k, \omega)$ for a lattice with parameters $t = 1$, $U = 0$, $\mu = 0$ and $T = 1$. The cluster used had $L_c = 2$ site and the saddle-point is the same as in figure A.4. The dashed line is at the chemical potential and frequencies are in units of the hopping energy t.

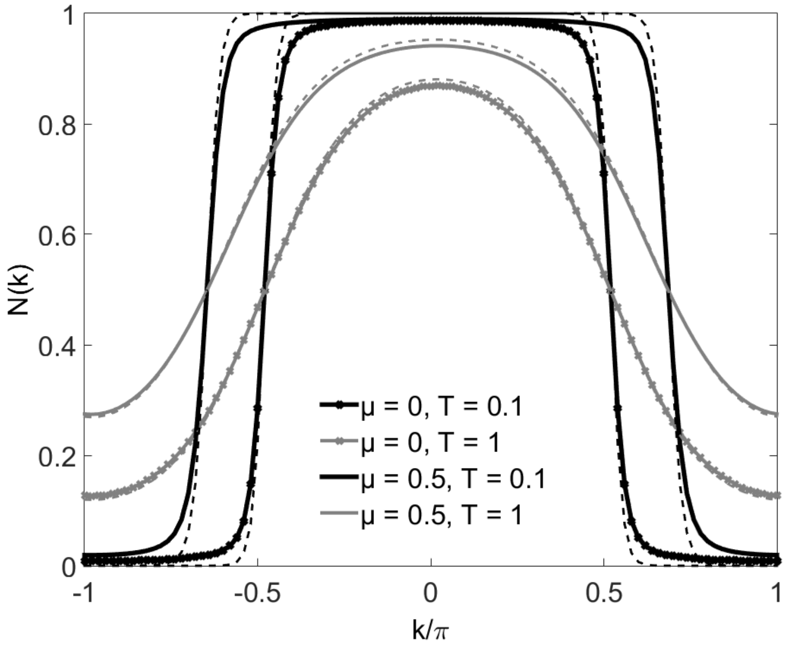

Figure A.6: Electron momentum distribution $N(k)$ for different chemical potentials μ and temperatures T with $U = 0$. The solid lines are the results from the numerical simulation of the quantum algorithm using time steps of size $d\tau = 0.02$ up to $\tau_{\max} = 200$ while the dashed lines come from an imaginary frequency summation. The parameters T and μ are in units of the hopping energy t.

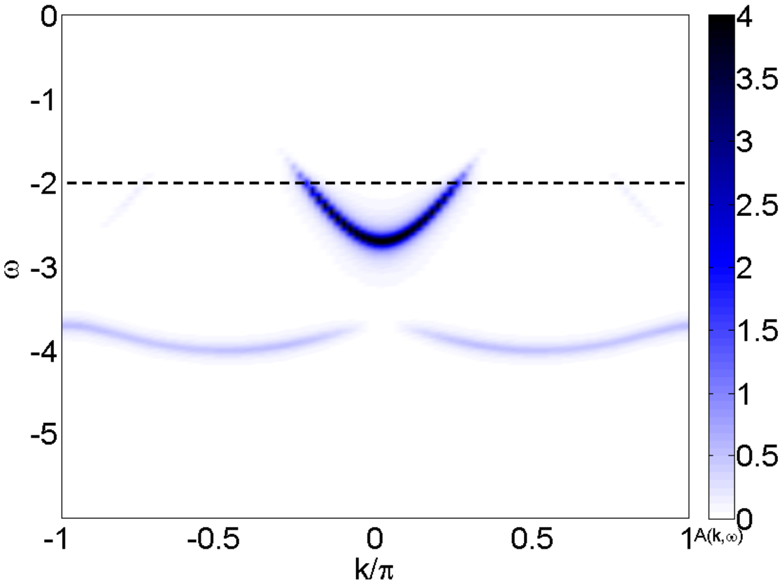

Figure A.7: Electron momentum-frequency distribution $A\left(k,\omega\right)$ for a lattice with parameters $t = 1$, $U = -4$, $\mu = -2$ and $T = 0.1$. The cluster used had $L_c = 2$ site and the saddle-point is at $\begin{pmatrix} \mu'_* \\ \Delta'_* \end{pmatrix} = \begin{pmatrix} -2 \\ 0 \end{pmatrix}$. The dashed line is at the chemical potential. The frequency axis is in units of t.

the number of time points that need to be measured may become an issue as the systems become more complex. It would be interesting to know if there exist sampling methods as efficient as imaginary frequency summation methods [86] where only ≈ 100 points need to be measured in order to achieve a high numerical accuracy in the computation of the Fermi function even for complicated electronic structures. For example, a cost function over several models could be used to extract the Green's function using fewer measurements.

A.4 PREPARATION OF A GIBBS STATE

A digital method to prepare Gibbs states in a quantum computer is reviewed and shown adequate for a variational solver. The goal is the make this document self-contained in the sense that action of the quantum computer can be fully defined.

Here is the summary of Eisert's method, as given in [108], to prepare the Gibbs state required to simulate the correlation function of the cluster. In addition to the simulated system Hamiltonian $\mathcal{H}'$, a bath Hamiltonian $\mathcal{H}_B$ is required such that the total uncoupled system is

$$\mathcal{H}_0 = \mathcal{H}' + \mathcal{H}_B \tag{A.9}$$

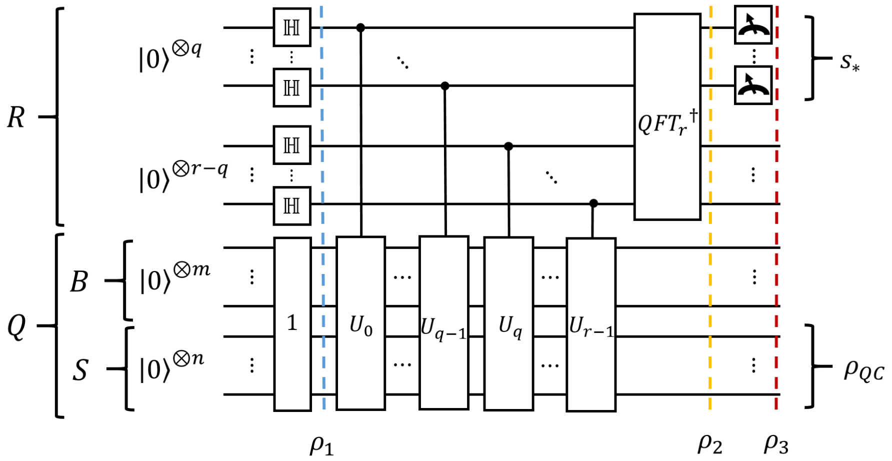
R
Q
B
S
$|0\rangle^{\otimes q}$
$|0\rangle^{\otimes r-q}$
$|0\rangle^{\otimes m}$
$|0\rangle^{\otimes n}$
$\mathbb{H}$
1
U_0
U_{q-1}
U_q
U_{r-1}
$QFT_r^\dagger$
s_*
ρ_{QC}
ρ_1
ρ_2
ρ_3

Figure A.8: Detailed circuit to prepare an approximate Gibbs state $\rho_{QC} \approx \rho_{\text{Gibbs}}$ following [108]. The simulated inverse temperature β is related to the measurement of s_* by equation (A.18). The initial state of R and Q is taken to be the zero state $|0\rangle^{\otimes(q+m+n)}$, then the Hadamard gate $\mathbb{H}^{\otimes q}$ is applied on R and Q is transformed (non-unitarily) to the fully mixed state $\frac{1}{2^{m+n}}\mathbb{I}^{\otimes(m+n)}$. Then q controlled-U operations are applied, where the notation $U_\tau = U^{2^\tau}$ and $U = e^{-i\frac{\mathcal{H}_0}{\|\mathcal{H}_0\|_\infty}}$ with $\mathcal{H}_0 = \mathcal{H}' + \mathcal{H}_B$. An inverse quantum Fourier transform is applied on register R and the string s_* is read from the first q qubits. Register S is then left in a simulated Gibbs state ρ_{QC}^S.

with eigenvalues $\left\{E_k^{(0)}\right\}$ and energy eigenvectors $\left\{\left|E_k^{(0)}\right\rangle\right\}$. The bath (first part of the register Q in figure 3.3) is assumed to be a collection of m uncoupled spin-$\frac{1}{2}$ with energy splitting η:

$$\mathcal{H}_B = \frac{\eta}{2}\sum_{j=1}^{m}\left(\mathbb{I}_j + \sigma_{zj}\right). \tag{A.10}$$

A small interaction $\mathcal{V}$ is allowed such that the total coupled system Hamiltonian is

$$\mathcal{H}_{tot} = \mathcal{H}_0 + \mathcal{V} \tag{A.11}$$

with eigenvalues $\{E_k\}$ and energy eigenvectors $\{|E_k\rangle\}$. The procedure is the following (see figure A.8)

1. *Initialization. r Hadamard gates $\mathbb{H}$ are applied on the qubits of register R and the register Q is in the fully mixed state of* (A.11) *through a state purification protocol such that*

   $$\rho_1 = \frac{1}{d}\sum_{s,s'=0}^{2^r-1}|s\rangle\langle s'|\otimes\sum_{k=1}^{d}|E_k\rangle\langle E_k| \tag{A.12}$$

   where $d = 2^{m+2L_c}$ is the total dimension of the system plus bath. This is equivalent to preparing the coupled system + bath at infinite temperature.

2. *Partial quantum phase estimation. r controlled-U operation are followed by an inverse Fourier transform on R. Note that $U = e^{-i\frac{\mathcal{H}_0}{\|\mathcal{H}_0\|_\infty}}$, where $\mathcal{H}_0$ is the uncoupled Hamiltonian* (A.9)*. After this phase estimation part, the state in the computer is*

   $$\rho_2 = \frac{1}{d}\sum_{s,s'=0}^{2^r-1}\sum_{k=1}^{d}\alpha_s(\varphi_k)\,\alpha_{s'}^*(\varphi_k)\,|s\rangle\langle s'|\otimes|E_k\rangle\langle E_k| \tag{A.13}$$

   where $\varphi_k \equiv \frac{E_k}{\|\mathcal{H}_{tot}\|_\infty}$ and

   $$\alpha_s(\varphi) \equiv \frac{1}{2^r}\frac{1-e^{2\pi i(2^r\varphi - s)}}{1-e^{2\pi i(\varphi - 2^{-r}s)}} \tag{A.14}$$

   The controlled evolution of the full system dephases different distributions of eigenvalues contained in the fully mixed state.

3. *Measurement. The first q qubits of R are measured. A binary string s_* (length q) is obtained*

   $$\rho_3 \propto \sum_{s,s'=s_*\Delta_{\text{rect}*}}^{(s_*+1)\Delta_{\text{rect}*}}\sum_{k=1}^{d}\alpha_s(\varphi_k)\,\alpha_{s'}^*(\varphi_k)\,|s\rangle\langle s'|\otimes|E_k\rangle\langle E_k| \tag{A.15}$$

   where $\Delta_{\text{rect}*} \equiv 2^{r-q}$ is the number of states of the ancillary register R compatible with the measurement. The width of the rectangular state

> *that is prepared is determined by* $\Delta_{\text{rect}} = \|\mathcal{H}_{tot}\|_\infty 2^{-r}\Delta_{\text{rect}*}$*. The energy of the rectangular state is* $E = \|\mathcal{H}_{tot}\|_\infty 2^{-q} s_*$*. The inverse temperature* β *is determined by* E *and* Δ_{rect}*. The final state in the register* Q *is now*
>
> $$\begin{aligned} \rho_{QC} &\equiv Tr_R \rho_3 \\ &\propto \textstyle\sum_{k=1}^{d} \left(\sum_{s=s_*\Delta_{\text{rect}}}^{(s_*+1)\Delta_{\text{rect}}} \left|\alpha_s\left(\varphi_k\right)\right|^2 \right) \left|E_k\right\rangle \left\langle E_k\right| . \end{aligned} \tag{A.16}$$
>
> *One of the rectangular states contained in the initial fully mixed state is selected upon measurement. For appropriately chosen parameters, the state in register* S *is approximately a Gibbs state of the cluster Hamiltonian.*

The algorithm outputs a reduced state $\rho^S_{\text{QC}} = \text{Tr}_B \rho_{QC} \approx \rho^S_{\text{Gibbs}} = \frac{e^{-\beta\mathcal{H}'}}{\text{Tr}e^{-\beta\mathcal{H}'}}$ in the channel S, where $\beta = \frac{1}{T}$ is the inverse temperature. Assuming a bath of the form (A.10) with energy scale $\eta = \sqrt{\frac{\lambda}{m}} \|\mathcal{H}'\|_\infty$, the "≈" really implies the following condition

$$\begin{aligned} \mathcal{D}\left(\rho^S_{\text{QC}}, \rho^S_{\text{Gibbs}}\right) &\leq \left(1 + \tfrac{\ln(2^{r-q})}{\pi^2}\right) \frac{e^{\frac{2}{\lambda} + \beta\|\mathcal{H}'\|_\infty + \frac{\lambda\|\mathcal{H}'\|^2_\infty \beta^2}{8}}}{2^{r-q-2}} \\ &\quad + \tfrac{1}{2}\left(e^{\frac{2}{\lambda}} - 1\right) + C \end{aligned} \tag{A.17}$$

where $\mathcal{D}(\cdot,\cdot)$ is the trace distance and C is a constant exponentially small in m. The effective inverse temperature is in the interval $[\beta - \delta\beta, \beta + \delta\beta]$ with

$$\beta = \frac{4}{\eta}\left(\frac{1}{2} - 2^{-q} s_* \left(1 + \frac{\|\mathcal{H}'\|_\infty}{\|\mathcal{H}_B\|_\infty}\right)\right). \tag{A.18}$$

Since $s_* \in [0, 2^q - 1]$, the inverse temperature of the generated Gibbs state can reach negative values in principle (physically corresponding to a state with an inverted population). The uncertainty on the temperature of the Gibbs state is bounded by

$$\begin{aligned} \delta\beta &\leq \tfrac{2^{2-q}}{\eta}\left(1 + \tfrac{\|\mathcal{H}'\|_\infty}{\|\mathcal{H}_B\|_\infty}\right) \\ &= 2^{2-q}\sqrt{\tfrac{\lambda}{m}}\tfrac{1}{\|\mathcal{H}'\|_\infty}\left(1 + \tfrac{1}{\sqrt{m\lambda}}\right). \end{aligned} \tag{A.19}$$

At least q qubits are needed according to the rule

$$q \geq \left\lceil -\log_2\left(\frac{\delta\beta\eta}{1 + \frac{\|\mathcal{H}'\|_\infty}{\|\mathcal{H}_B\|_\infty}}\right) + 2\right\rceil \tag{A.20}$$

and the average number of runs required to achieve some inverse temperature is

$$\overline{\sharp\text{runs}} \leq 2^{q} \sqrt{\frac{\pi}{2m}} e^{\frac{2}{\lambda}+\beta\|\mathcal{H}'\|_{\infty}+\frac{\lambda\|\mathcal{H}'\|_{\infty}^{2}\beta^{2}}{8}}. \tag{A.21}$$

This last bound is a worst-case scenario as finding the ground state of the FHM is in general a QMA − hard problem.

BIBLIOGRAPHY

[1] David Deutsch. “Concepts of Quantum Information.” In: *The Physics of Quantum Information*. Ed. by Dirk Bouwmeester, Artur Ekert, and Anton Zeilinger. Springer Science Business Media, 2000. Chap. 4. DOI: `10.1007/978-3-662-04209-0` (cit. on p. v).

[2] Alexandre Grothendieck. *Récoltes et semailles. Réflexions et témoignage sur un passé de mathématicien*. 1986. URL: `http://lipn.univ-paris13.fr/~duchamp/Books&more/Grothendieck/RS/pdf/RetS.pdf` (cit. on p. xi).

[3] E. Schrödinger. “Die gegenwärtige Situation in der Quantenmechanik.” In: *Die Naturwissenschaften* 23.48 (Nov. 1935), pp. 807–812. DOI: `10.1007/BF01491891` (cit. on p. 1).

[4] A. Einstein, B. Podolsky, and N. Rosen. “Can Quantum-Mechanical Description of Physical Reality Be Considered Complete?” In: *Phys. Rev.* 47.10 (May 1935), pp. 777–780. DOI: `10.1103/PhysRev.47.777` (cit. on p. 1).

[5] J.S. Bell. “On the Einstein Podolsky Rosen paradox.” In: *Physics* 1.3 (1964), p. 195 (cit. on p. 1).

[6] B. Hensen et al. “Loophole-free Bell inequality violation using electron spins separated by 1.3 kilometres.” In: *Nature* 526.7575 (Oct. 2015), pp. 682–686. DOI: `10.1038/nature15759` (cit. on p. 1).

[7] Freeman Dyson. “"Freeman Dyson: Mathematician, Physicist, and Writer". Interview with Donald J. Albers.” In: *The College Mathematics Journal* 25.1 (1994) (cit. on p. 3).

[8] H. K. Onnes. “The resistance of pure mercury at helium temperatures.” In: *Commun. Phys. Lab. Univ. Leiden* 12 (1911), p. 120 (cit. on p. 5).

[9] P. G. de Gennes. *Superconductivity of Metals and Alloys*. Ed. by David Pines. Boulder, Colorado: Westview Press, 1989 (cit. on pp. 5, 7).

[10] Carsten Timm. *Theory of Superconductivity*. 2012. URL: `http://www.physik.tu-dresden.de/~timm/personal/teaching/thsup_w11/Theory_of_Superconductivity.pdf` (cit. on p. 6).

[11] W. Meissner and R. Ochsenfeld. “Ein neuer Effekt bei Eintritt der Supraleitfähigkeit.” In: *Naturwissenschaften* 21.44 (Nov. 1933), pp. 787–788. DOI: `10.1007/bf01504252` (cit. on p. 7).

[12] F. London and H. London. "The Electromagnetic Equations of the Supraconductor." In: *Proceedings of the Royal Society A: Mathematical, Physical and Engineering Sciences* 149.866 (Mar. 1935), pp. 71–88. DOI: `10.1098/rspa.1935.0048` (cit. on p. 7).

[13] Piotr Jaworski. *Diagram of the Meissner Effect*. CC-BY-SA-3.0 http://creativecommons.org/licenses/by-sa/3.0/. 2005. URL: `https://commons.wikimedia.org/wiki/File:EfektMeisnera.svg` (cit. on p. 7).

[14] J. Bardeen, L. N. Cooper, and J. R. Schrieffer. "Microscopic Theory of Superconductivity." In: *Phys. Rev.* 106.1 (Apr. 1957), pp. 162–164. DOI: `10.1103/physrev.106.162` (cit. on p. 8).

[15] J. Bardeen, L. N. Cooper, and J. R. Schrieffer. "Theory of Superconductivity." In: *Phys. Rev.* 108.5 (Dec. 1957), pp. 1175–1204. DOI: `10.1103/physrev.108.1175` (cit. on p. 8).

[16] Anthony James Leggett. *Quantum Liquids*. Oxford University Press (OUP), Sept. 2006. DOI: `10.1093/acprof:oso/9780198526438.001.0001` (cit. on pp. 8, 9, 19, 21, 22, 26, 30).

[17] B. D. Josephson. "Possible new effects in superconductive tunnelling." In: *Physics Letters* 1.7 (July 1962), pp. 251–253. DOI: `10.1016/0031-9163(62)91369-0` (cit. on p. 9).

[18] John Clarke and Frank K. Wilhelm. "Superconducting quantum bits." In: *Nature* 453.7198 (June 2008), pp. 1031–1042. DOI: `10.1038/nature07128` (cit. on p. 9).

[19] J. Q. You and Franco Nori. "Atomic physics and quantum optics using superconducting circuits." In: *Nature* 474.7353 (June 2011), pp. 589–597. DOI: `10.1038/nature10122` (cit. on p. 9).

[20] G. Rickayzen. *Green's Functions and Condensend Matter*. Academic Press, 1991 (cit. on pp. 13, 26, 44, 46, 68).

[21] L. P. Gor'kov. "Microscopic derivation of the Ginzburg-Landau equations in the theory of superconductivity." In: *Soviet Physics JETP* 36(9).6 (1959), p. 1364 (cit. on p. 18).

[22] J. G. Bednorz and K. A. Müller. "Possible high Tc superconductivity in the Ba-La-Cu-O system." In: *Zeitschrift für Physik B Condensed Matter* 64.2 (June 1986), pp. 189–193. DOI: `http://dx.doi.org/10.1007/BF01303701` (cit. on p. 19).

[23] M. K. Wu, J. R. Ashburn, C. J. Torng, P. H. Hor, R. L. Meng, L. Gao, Z. J. Huang, Y. Q. Wang, and C. W. Chu. "Superconductivity at 93 K in a new mixed-phase Y-Ba-Cu-O compound system at ambient pressure." In: *Phys. Rev. Lett.* 58.9 (Mar. 1987), pp. 908–910. DOI: `10.1103/physrevlett.58.908` (cit. on p. 19).

[24] Pia Jensen Ray. "Structural investigation of La(2-x)Sr(x)CuO(4+y) - Following staging as a function of temperature." MA thesis. Niels Bohr Institute, Faculty of Science, University of Copenhagen, 2015. DOI: `10.6084/m9.figshare.2075680.v2` (cit. on p. 20).

[25] User:Haj33. *Unit Cell Structure of YBa2Cu3O7 compound*. CC-BY-SA-3.0 http://creativecommons.org/licenses/by-sa/3.0/. 2009. URL: `https://commons.wikimedia.org/wiki/File:Ybco.jpg` (cit. on p. 21).

[26] P. W. Anderson. "The Resonating Valence Bond State in La2CuO4 and Superconductivity." In: *Science* 235.4793 (Mar. 1987), pp. 1196–1198. DOI: `10.1126/science.235.4793.1196` (cit. on pp. 22, 25).

[27] J. Hubbard. "Electron Correlations in Narrow Energy Bands." In: *Proceedings of the Royal Society A: Mathematical, Physical and Engineering Sciences* 276.1365 (Nov. 1963), pp. 238–257. DOI: `10.1098/rspa.1963.0204` (cit. on pp. 22, 25).

[28] Toby S. Cubitt, David Perez-Garcia, and Michael M. Wolf. "Undecidability of the spectral gap." In: *Nature* 528.7581 (Dec. 2015), pp. 207–211. DOI: `10.1038/nature16059` (cit. on pp. 23, 31).

[29] D. N. Basov and T. Timusk. "Electrodynamics of high- T c superconductors." In: *Rev. Mod. Phys.* 77.2 (Aug. 2005), pp. 721–779. DOI: `http://dx.doi.org/10.1103/RevModPhys.77.721` (cit. on pp. 23, 31).

[30] D. J. Egger and F. K. Wilhelm. "Multimode Circuit Quantum Electrodynamics with Hybrid Metamaterial Transmission Lines." In: *Phys. Rev. Lett.* 111.16 (Oct. 2013), p. 163601. DOI: `10.1103/physrevlett.111.163601` (cit. on p. 23).

[31] Vera N. Smolyaninova, Bradley Yost, Kathryn Zander, M. S. Osofsky, Heungsoo Kim, Shanta Saha, R. L. Greene, and Igor I. Smolyaninov. "Experimental demonstration of superconducting critical temperature increase in electromagnetic metamaterials." In: *Sci. Rep.* 4 (Dec. 2014), p. 7321. DOI: `10.1038/srep07321`. arXiv: `physics.optics/1408.0704v2` (cit. on p. 23).

[32] A.-M.S. Tremblay, B. Kyung, and D. Sénéchal. "Pseudogap and high-temperature superconductivity from weak to strong coupling. Towards quantitative theory." In: *Low Temperature Physics* 32.4 (2006), pp. 424–451. DOI: `http://dx.doi.org/10.1063/1.2199446` (cit. on pp. 25, 27, 47, 48).

[33] Subir Sachdev. "The Landscape of the Hubbard Model." In: *String Theory and Its Applications*. World Scientific Pub Co Pte Lt, Nov. 2011, pp. 559–620. DOI: `10.1142/9789814350525_0009`. arXiv: `hep-th/1012.0299v5 [hep-th]` (cit. on p. 25).

[34] Junjiro Kanamori. “Electron Correlation and Ferromagnetism of Transition Metals.” In: *Prog. Theor. Phys.* 30.3 (Sept. 1963), pp. 275–289. DOI: `10.1143/PTP.30.275` (cit. on p. 25).

[35] Martin C. Gutzwiller. “Effect of Correlation on the Ferromagnetism of Transition Metals.” In: *Phys. Rev. Lett.* 10.5 (Mar. 1963), pp. 159–162. DOI: `10.1103/physrevlett.10.159` (cit. on p. 25).

[36] A. J. Leggett. “A "midinfrared" scenario for cuprate superconductivity.” In: *Proc. Natl. Acad. Sci. USA* 96.15 (July 1999), pp. 8365–8372. DOI: `10.1073/pnas.96.15.8365` (cit. on p. 25).

[37] Mathieu Guillot. “Competition entre l’antiferromagnetisme et la supraconductivite dans le model de Hubbard applique aux cuprates.” MA thesis. Universite de Sherbrooke, 2007 (cit. on p. 25).

[38] J. Kaczmarczyk, J. Spalek, T. Schickling, and J. Buenemann. “Superconductivity in the two-dimensional Hubbard model: Gutzwiller wave function solution.” In: *Phys. Rev. B* 88.11 (Sept. 2013), p. 115127. DOI: `10.1103/physrevb.88.115127` (cit. on p. 25).

[39] Keisuke Masuda and Daisuke Yamamoto. “Variational cluster approach to s -wave pairing in heavy-fermion superconductors.” In: *Phys. Rev. B* 91.10 (Mar. 2015), p. 104508. DOI: `http://dx.doi.org/10.1103/PhysRevB.91.104508` (cit. on pp. 25, 38).

[40] Tilman Esslinger. “Fermi-Hubbard Physics with Atoms in an Optical Lattice.” In: *Annu. Rev. Condens. Matter Phys.* 1.1 (Aug. 2010), pp. 129–152. DOI: `10.1146/annurev-conmatphys-070909-104059` (cit. on p. 25).

[41] David C. McKay. “Quantum simulation in strongly correlated optical lattices.” PhD thesis. University of Illinois at Urbana-Champaign, 2012 (cit. on p. 25).

[42] Rudolph Pariser and Robert G. Parr. “A Semi-Empirical Theory of the Electronic Spectra and Electronic Structure of Complex Unsaturated Molecules. I.” In: *The Journal of Chemical Physics* 21.3 (1953), p. 466. DOI: `http://dx.doi.org/10.1063/1.1698929` (cit. on p. 25).

[43] Rudolph Pariser and Robert G. Parr. “A Semi-Empirical Theory of the Electronic Spectra and Electronic Structure of Complex Unsaturated Molecules. II.” In: *The Journal of Chemical Physics* 21.5 (1953), p. 767. DOI: `http://dx.doi.org/10.1063/1.1699030` (cit. on p. 25).

[44] J. A. Pople. “Electron interaction in unsaturated hydrocarbons.” In: *Trans. Faraday Soc.* 49 (1953), p. 1375. DOI: `10.1039/TF9534901375` (cit. on p. 25).

[45] Johannes Voit. “One-dimensional Fermi liquids.” In: *Rep. Prog. Phys.* 58.9 (Sept. 1995), pp. 977–1116. DOI: `10.1088/0034-4885/58/9/002` (cit. on p. 25).

[46] Elliott H. Lieb and F.Y. Wu. “The one-dimensional Hubbard model: a reminiscence.” In: *Physica A* 321.1-2 (Apr. 2003), pp. 1–27. DOI: `10.1016/s0378-4371(02)01785-5` (cit. on pp. 25–27).

[47] Fabian H. L. Essler, Holger Frahm, Frank Göhmann, Andreas Klümper, and Vladimir E. Korepin. *The One-Dimensional Hubbard Model*. Cambridge University Press (CUP), 2005. DOI: `10.1017/cbo9780511534843` (cit. on pp. 25–27).

[48] D.B. Uglov and V.E. Korepin. “The Yangian symmetry of the Hubbard model.” In: *Physics Letters A* 190.3-4 (July 1994), pp. 238–242. DOI: `10.1016/0375-9601(94)90748-x` (cit. on p. 25).

[49] Hal Tasaki. “The Hubbard model - an introduction and selected rigorous results.” In: *Journal of Physics: Condensed Matter* 10.20 (May 1998), pp. 4353–4378. DOI: `10.1088/0953-8984/10/20/004` (cit. on p. 25).

[50] David Sénéchal, André-Marie Tremblay, and Claude Bourbonnais, eds. *Theoretical Methods for Strongly Correlated Electrons*. CRM Series in Mathematical Physics. Springer-Verlag, 2004. DOI: `10.1007/b97552` (cit. on p. 25).

[51] Jan Kurzyk, Josef Spalek, and Wlodzimierz Wojcik. “Lieb-Wu Solution, Gutzwiller-Wave-Function, and Gutzwiller-Ansatz Approximations with Adjustable Single-Particle Wave Function for the Hubbard Chain.” In: *Acta Phys. Pol. A* 111.4 (Apr. 2007), pp. 603–618. DOI: `10.12693/aphyspola.111.603` (cit. on p. 25).

[52] Ning Bao, Patrick Hayden, Grant Salton, and Nathaniel Thomas. “Universal quantum computation by scattering in the Fermi–Hubbard model.” In: *New Journal of Physics* 17.9 (Sept. 2015), p. 093028. DOI: `10.1088/1367-2630/17/9/093028` (cit. on pp. 25, 31, 73).

[53] Walter Metzner, Manfred Salmhofer, Carsten Honerkamp, Volker Meden, and Kurt Schönhammer. “Functional renormalization group approach to correlated fermion systems.” In: *Reviews of Modern Physics* 84.1 (Mar. 2012), pp. 299–352. DOI: `10.1103/RevModPhys.84.299` (cit. on pp. 25, 30).

[54] Andreas Mielke. “The Hubbard Model and its Properties. Modeling and Simulation.” In: *Many-Body Physics: From Kondo to Hubbard*. Ed. by Eva Pavarini, Erik Koch, and Piers Coleman. Vol. 5. Verlag des Forschungszentrum Jülich, 2015 (cit. on pp. 25, 27, 30).

[55] D. Sénéchal, D. Perez, and M. Pioro-Ladrière. “Spectral Weight of the Hubbard Model through Cluster Perturbation Theory.” In: *Phys. Rev. Lett.* 84.3 (Jan. 2000), pp. 522–525. DOI: `10.1103/physrevlett.84.522` (cit. on p. 25).

[56] David Senechal. *An introduction to quantum cluster methods*. May 2008. arXiv: `cond-mat.str-el/0806.2690v2 [cond-mat.str-el]`. URL: `http://arxiv.org/abs/0806.2690` (cit. on pp. 25, 27, 36, 39, 40, 42, 46, 71, 86).

[57] M. Potthoff, M. Aichhorn, and C. Dahnken. "Variational Cluster Approach to Correlated Electron Systems in Low Dimensions." In: *Phys. Rev. Lett.* 91.20 (Nov. 2003), p. 206402. DOI: `10.1103/physrevlett.91.206402` (cit. on pp. 25, 27, 34, 73).

[58] M. Potthoff. "Dynamical Variational Principles for Strongly Correlated Electron Systems." In: *Adv. Solid State Phys.* 45 (2005), pp. 135–147. DOI: `10.1007/11423256_11` (cit. on pp. 25, 33).

[59] Michael Potthoff. "Non-perturbative construction of the Luttinger-Ward functional." In: *Condensed Matter Physics* 9.3 (2006), p. 557. DOI: `10.5488/cmp.9.3.557` (cit. on pp. 25, 32, 71).

[60] David P. DiVincenzo. "The Physical Implementation of Quantum Computation." In: *Fortschr. Phys.* 48.9-11 (Sept. 2000), pp. 771–783. DOI: `10.1002/1521-3978(200009)48:9/11<771::aid-prop771>3.0.co;2-e` (cit. on pp. 25, 58).

[61] Elliott H. Lieb and F. Y. Wu. "Absence of Mott Transition in an Exact Solution of the Short-Range, One-Band Model in One Dimension." In: *Phys. Rev. Lett.* 20.25 (June 1968), pp. 1445–1448. DOI: `10.1103/PhysRevLett.20.1445` (cit. on pp. 26, 27).

[62] Matthias Troyer and Uwe-Jens Wiese. "Computational Complexity and Fundamental Limitations to Fermionic Quantum Monte Carlo Simulations." In: *Phys. Rev. Lett.* 94.17 (May 2005). DOI: `10.1103/PhysRevLett.94.170201` (cit. on p. 27).

[63] A. Moreo and D. J. Scalapino. "Correlations in the two-dimensional Hubbard model." In: *Phys. Rev. B* 43.10 (Apr. 1991), pp. 8211–8216. DOI: `10.1103/PhysRevB.43.8211` (cit. on p. 27).

[64] Richard T. Scalettar, Rajiv R. P. Singh, and Shoucheng Zhang. "Odd-parity singlet pairing in the positive- U Hubbard model." In: *Phys. Rev. Lett.* 67.3 (July 1991), pp. 370–373. DOI: `10.1103/PhysRevLett.67.370` (cit. on p. 27).

[65] David Sénéchal, P.-L. Lavertu, M.-A. Marois, and A.-M. S. Tremblay. "Competition between Antiferromagnetism and Superconductivity in High- T c Cuprates." In: *Phys. Rev. Lett.* 94.15 (Apr. 2005), p. 156404. DOI: `http://dx.doi.org/10.1103/PhysRevLett.94.156404` (cit. on pp. 27, 48).

[66] Walter Metzner and Dieter Vollhardt. "Correlated Lattice Fermions in $d = \infty$ Dimensions." In: *Phys. Rev. Lett.* 62.3 (Jan. 1989), pp. 324–327. DOI: `10.1103/PhysRevLett.62.324` (cit. on p. 27).

[67] Th. Pruschke, D. L. Cox, and M. Jarrell. “Hubbard model at infinite dimensions: Thermodynamic and transport properties.” In: *Phys. Rev. B* 47.7 (Feb. 1993), pp. 3553–3565. DOI: `10.1103/PhysRevB.47.3553` (cit. on p. 27).

[68] Antoine Georges, Gabriel Kotliar, Werner Krauth, and Marcelo J. Rozenberg. “Dynamical mean-field theory of strongly correlated fermion systems and the limit of infinite dimensions.” In: *Reviews of Modern Physics* 68.1 (Jan. 1996), pp. 13–125. DOI: `10.1103/revmodphys.68.13` (cit. on p. 27).

[69] Michael Potthoff. “Self-energy-functional theory.” In: *Theoretical Methods for Strongly Correlated Systems*. Ed. by Adolfo Avella and Ferdinando Mancini. Springer Berlin Heidelberg, 2012. DOI: `10.1007/978-3-642-21831-6` (cit. on pp. 27, 28, 35).

[70] A. I. Lichtenstein and M. I. Katsnelson. “Antiferromagnetism and d -wave superconductivity in cuprates: A cluster dynamical mean-field theory.” In: *Phys. Rev. B* 62.14 (Oct. 2000), R9283–R9286. DOI: `10.1103/PhysRevB.62.R9283` (cit. on p. 27).

[71] Gabriel Kotliar, Sergej Y. Savrasov, Gunnar Pálsson, and Giulio Biroli. “Cellular Dynamical Mean Field Approach to Strongly Correlated Systems.” In: *Phys. Rev. Lett.* 87.18 (Oct. 2001). DOI: `10.1103/PhysRevLett.87.186401` (cit. on p. 27).

[72] B. Sriram Shastry. “Exact Integrability of the One-Dimensional Hubbard Model.” In: *Phys. Rev. Lett.* 56.23 (June 1986), pp. 2453–2455. DOI: `10.1103/PhysRevLett.56.2453` (cit. on p. 27).

[73] Elliott H. Lieb. “Two theorems on the Hubbard model.” In: *Phys. Rev. Lett.* 62.10 (Mar. 1989), pp. 1201–1204. DOI: `10.1103/PhysRevLett.62.1201` (cit. on p. 29).

[74] N. D. Mermin and H. Wagner. “Absence of Ferromagnetism or Antiferromagnetism in One- or Two-Dimensional Isotropic Heisenberg Models.” In: *Phys. Rev. Lett.* 17.22 (Nov. 1966), pp. 1133–1136. DOI: `10.1103/PhysRevLett.17.1133` (cit. on p. 30).

[75] P. C. Hohenberg. “Existence of Long-Range Order in One and Two Dimensions.” In: *Phys. Rev.* 158.2 (June 1967), pp. 383–386. DOI: `10.1103/PhysRev.158.383` (cit. on p. 30).

[76] A. K. Geim and K. S. Novoselov. “The rise of graphene.” In: *Nature Materials* 6.3 (Mar. 2007), pp. 183–191. DOI: `10.1038/nmat1849` (cit. on p. 30).

[77] Tohru Koma and Hal Tasaki. “Decay of superconducting and magnetic correlations in one- and two-dimensional Hubbard models.” In: *Phys. Rev. Lett.* 68.21 (May 1992), pp. 3248–3251. DOI: `10.1103/physrevlett.68.3248` (cit. on p. 30).

[78] A. Fasolino, J. H. Los, and M. I. Katsnelson. “Intrinsic ripples in graphene.” In: *Nature Materials* 6.11 (Sept. 2007), pp. 858–861. DOI: `10.1038/nmat2011` (cit. on p. 31).

[79] Andrea Damascelli, Zahid Hussain, and Zhi-Xun Shen. "Angle-resolved photoemission studies of the cuprate superconductors." In: *Reviews of Modern Physics* 75.2 (Apr. 2003), pp. 473–541. DOI: `10.1103/RevModPhys.75.473` (cit. on p. 31).

[80] Andrea Damascelli. "Probing the Electronic Structure of Complex Systems by ARPES." In: *Physica Scripta* T109 (2004), p. 61. DOI: `10.1238/Physica.Topical.109a00061` (cit. on p. 31).

[81] Robert Eder. "The Variational Cluster Approximation." In: *Emergent Phenomena in Correlated Matter*. Ed. by Eva Pavarini, Erik Koch, and Ulrich Schollwöck. Vol. 3. Modeling and Simulation. Verlag des Forschungszentrum Jülich, 2013 (cit. on p. 33).

[82] Arnau Rios Huguet. "Thermodynamical Properties of Nuclear Matter from a Self-Consistent Green's Function Approach." PhD thesis. Universitat de Barcelona, 2007. URL: `http://personal.ph.surrey.ac.uk/~m01088/files/thesis.pdf` (cit. on p. 32).

[83] M. Aichhorn, E. Arrigoni, M. Potthoff, and W. Hanke. "Variational cluster approach to the Hubbard model: Phase-separation tendency and finite-size effects." In: *Phys. Rev. B* 74.23 (Dec. 2006), p. 235117. DOI: `10.1103/physrevb.74.235117` (cit. on p. 36).

[84] Thomas Maier, Mark Jarrell, Thomas Pruschke, and Matthias H. Hettler. "Quantum cluster theories." In: *Reviews of Modern Physics* 77.3 (Oct. 2005), pp. 1027–1080. DOI: `10.1103/revmodphys.77.1027` (cit. on pp. 36, 40).

[85] Ning-Hua Tong. "Extended variational cluster approximation for correlated systems." In: *Phys. Rev. B* 72.11 (Sept. 2005), p. 115104. DOI: `10.1103/physrevb.72.115104` (cit. on pp. 37, 57, 72).

[86] Taisuke Ozaki. "Continued fraction representation of the Fermi-Dirac function for large-scale electronic structure calculations." In: *Phys. Rev. B* 75.3 (Jan. 2007), p. 035123. DOI: `10.1103/physrevb.75.035123` (cit. on pp. 41, 46, 107).

[87] Tatsuya Kaneko and Yukinori Ohta. "BCS-BEC Crossover in the Two-Dimensional Attractive Hubbard Model: Variational Cluster Approach." In: *Journal of the Physical Society of Japan* 83.2 (Feb. 2014), p. 024711. DOI: `10.7566/jpsj.83.024711` (cit. on pp. 44, 71).

[88] C. Dahnken, M. Aichhorn, W. Hanke, E. Arrigoni, and M. Potthoff. "Variational cluster approach to spontaneous symmetry breaking: The itinerant antiferromagnet in two dimensions." In: *Phys. Rev. B* 70.24 (Dec. 2004), p. 245110. DOI: `10.1103/physrevb.70.245110` (cit. on pp. 47, 48).

[89] Richard P. Feynman. “Simulating physics with computers.” In: *International Journal of Theoretical Physics* 21.6-7 (June 1982), pp. 467–488. DOI: `10.1007/bf02650179` (cit. on pp. 55, 57, 58, 73).

[90] U. Las Heras, A. Mezzacapo, L. Lamata, S. Filipp, A. Wallraff, and E. Solano. “Digital Quantum Simulation of Spin Systems in Superconducting Circuits.” In: *Phys. Rev. Lett.* 112.20 (May 2014), p. 200501. DOI: `10.1103/physrevlett.112.200501` (cit. on pp. 57, 73).

[91] Y. Salathe et al. “Digital Quantum Simulation of Spin Models with Circuit Quantum Electrodynamics.” In: *Phys. Rev. X* 5.2 (June 2015), p. 021027. DOI: `10.1103/physrevx.5.021027` (cit. on pp. 57, 73).

[92] Lucas Lamata, Antonio Mezzacapo, Jorge Casanova, and Enrique Solano. “Efficient quantum simulation of fermionic and bosonic models in trapped ions.” In: *EPJ Quantum Technology* 1.1 (June 2014), p. 9. DOI: `10.1140/epjqt9` (cit. on pp. 57, 73).

[93] Alberto Peruzzo, Jarrod McClean, Peter Shadbolt, Man-Hong Yung, Xiao-Qi Zhou, Peter J. Love, Alán Aspuru-Guzik, and Jeremy L. O’Brien. “A variational eigenvalue solver on a photonic quantum processor.” In: *Nature Communications* 5 (July 2014), p. 4213. DOI: `10.1038/ncomms5213` (cit. on pp. 57, 64, 73).

[94] Urtzi Las Heras, Laura Garcıa-Álvarez, Antonio Mezzacapo, Enrique Solano, and Lucas Lamata. “Fermionic models with superconducting circuits.” In: *EPJ Quantum Technology* 2.1 (Mar. 2015), p. 8. DOI: `10.1140/epjqt/s40507-015-0021-5` (cit. on pp. 57, 66, 71, 73, 89).

[95] R. Barends et al. “Digital quantum simulation of fermionic models with a superconducting circuit.” In: *Nature Communications* 6 (July 2015), p. 7654. DOI: `10.1038/ncomms8654` (cit. on pp. 57, 73).

[96] Joonsuk Huh, Gian Giacomo Guerreschi, Borja Peropadre, Jarrod R. McClean, and Alán Aspuru-Guzik. “Boson sampling for molecular vibronic spectra.” In: *Nature Photonics* 9.9 (Aug. 2015), pp. 615–620. DOI: `10.1038/nphoton.2015.153` (cit. on p. 57).

[97] Michael Potthoff and Matthias Balzer. “Self-energy-functional theory for systems of interacting electrons with disorder.” In: *Phys. Rev. B* 75.12 (Mar. 2007). DOI: `10.1103/PhysRevB.75.125112` (cit. on p. 57).

[98] Felix Hofmann, Martin Eckstein, Enrico Arrigoni, and Michael Potthoff. "Nonequilibrium self-energy functional theory." In: *Phys. Rev. B* 88.16 (Oct. 2013), p. 165124. DOI: `10.1103/physrevb.88.165124` (cit. on p. 57).

[99] S. Filor and T. Pruschke. "Variational cluster approximation to the thermodynamics of quantum spin systems." In: *New Journal of Physics* 16.6 (June 2014), p. 063059. DOI: `10.1088/1367-2630/16/6/063059` (cit. on p. 57).

[100] Michael Knap, Enrico Arrigoni, and Wolfgang von der Linden. "Variational cluster approach for strongly correlated lattice bosons in the superfluid phase." In: *Phys. Rev. B* 83.13 (Apr. 2011), p. 134507. DOI: `10.1103/physrevb.83.134507` (cit. on p. 57).

[101] Erez Zohar and Michele Burrello. "Formulation of lattice gauge theories for quantum simulations." In: *Physical Review D* 91.5 (Mar. 2015), p. 054506. DOI: `10.1103/physrevd.91.054506` (cit. on p. 57).

[102] Erez Zohar, J Ignacio Cirac, and Benni Reznik. "Quantum simulations of lattice gauge theories using ultracold atoms in optical lattices." In: *Rep. Prog. Phys.* 79.1 (Dec. 2015), p. 014401. DOI: `10.1088/0034-4885/79/1/014401` (cit. on p. 57).

[103] Michael A. Nielsen and Isaac L. Chuang. *Quantum Computation and Quantum Information*. Cambridge University Press (CUP), 2009. DOI: `10.1017/cbo9780511976667` (cit. on pp. 58, 61, 62, 69, 78).

[104] Ivan Kassal, James D. Whitfield, Alejandro Perdomo-Ortiz, Man-Hong Yung, and Alán Aspuru-Guzik. "Simulating Chemistry Using Quantum Computers." In: *Annual Review of Physical Chemistry* 62.1 (May 2011), pp. 185–207. DOI: `10.1146/annurev-physchem-032210-103512` (cit. on pp. 58, 73).

[105] Peter W. Shor. "Polynomial-Time Algorithms for Prime Factorization and Discrete Logarithms on a Quantum Computer." In: *SIAM Rev.* 41.2 (Jan. 1999), pp. 303–332. DOI: `10.1137/s0036144598347011` (cit. on p. 58).

[106] E. Knill and R. Laflamme. "Power of One Bit of Quantum Information." In: *Phys. Rev. Lett.* 81.25 (Dec. 1998), pp. 5672–5675. DOI: `http://dx.doi.org/10.1103/PhysRevLett.81.5672` (cit. on pp. 61, 67, 69).

[107] P. Jordan and E. Wigner. "Über das Paulische Äquivalenzverbot." In: *Z. Phys.* 47 (1928), p. 631. DOI: `10.1007/978-3-662-02781-3_9` (cit. on p. 63).

[108] Arnau Riera, Christian Gogolin, and Jens Eisert. "Thermalization in Nature and on a Quantum Computer." In: *Phys. Rev. Lett.* 108.8 (Feb. 2012), p. 080402. DOI: `10.1103/physrevlett.108.080402` (cit. on pp. 64, 65, 71, 75, 90, 107, 108).

[109] David Poulin and Pawel Wocjan. "Sampling from the Thermal Quantum Gibbs State and Evaluating Partition Functions with a Quantum Computer." In: *Phys. Rev. Lett.* 103.22 (Nov. 2009), p. 220502. DOI: `10.1103/physrevlett.103.220502` (cit. on p. 64).

[110] Ersen Bilgin and Sergio Boixo. "Preparing Thermal States of Quantum Systems by Dimension Reduction." In: *Phys. Rev. Lett.* 105.17 (Oct. 2010), p. 170405. DOI: `10.1103/physrevlett.105.170405` (cit. on p. 64).

[111] K. Temme, T. J. Osborne, K. G. Vollbrecht, D. Poulin, and F. Verstraete. "Quantum Metropolis sampling." In: *Nature* 471.7336 (Mar. 2011), pp. 87–90. DOI: `10.1038/nature09770` (cit. on p. 64).

[112] Dave Wecker, Matthew B. Hastings, Nathan Wiebe, Bryan K. Clark, Chetan Nayak, and Matthias Troyer. "Solving strongly correlated electron models on a quantum computer." In: *Phys. Rev. A* 92.6 (Dec. 2015), p. 062318. DOI: `10.1103/physreva.92.062318`. URL: `http` (cit. on pp. 66, 94).

[113] Jacob T. Seeley, Martin J. Richard, and Peter J. Love. "The Bravyi-Kitaev transformation for quantum computation of electronic structure." In: *J. Chem. Phys.* 137.22 (2012), p. 224109. DOI: `10.1063/1.4768229` (cit. on pp. 67, 71).

[114] Daniel S. Abrams and Seth Lloyd. "Simulation of Many-Body Fermi Systems on a Universal Quantum Computer." In: *Phys. Rev. Lett.* 79.13 (Sept. 1997), pp. 2586–2589. DOI: `10.1103/physrevlett.79.2586` (cit. on p. 67).

[115] Animesh Datta, Anil Shaji, and Carlton M. Caves. "Quantum Discord and the Power of One Qubit." In: *Phys. Rev. Lett.* 100.5 (Feb. 2008), p. 050502. DOI: `10.1103/physrevlett.100.050502` (cit. on p. 67).

[116] Andrew M. Childs, David Gosset, and Zak Webb. "The Bose-Hubbard Model is QMA-complete." In: *Proceedings of the 41s International Colloquium on Automata, Languages, and Programming* 8572 (2014), pp. 308–319. DOI: `10.1007/978-3-662-43948-7_26` (cit. on p. 68).

[117] Yuli V. Nazarov and Yaroslav M. Blanter. *Quantum Transport*. Cambridge University Press (CUP), 2009. DOI: `10.1017/cbo9780511626906` (cit. on p. 72).

[118] P. J. J. O'Malley et al. *Scalable Quantum Simulation of Molecular Energies*. 2015. URL: `http://arxiv.org/abs/1512.06860` (cit. on p. 73).

[119] Ryan Babbush, Dominic W Berry, Ian D Kivlichan, Annie Y Wei, Peter J Love, and Alán Aspuru-Guzik. "Exponentially more precise quantum simulation of fermions in second quantization." In: *New Journal of Physics* 18.3 (Mar. 2016), p. 033032. DOI: `10.1088/1367-2630/18/3/033032` (cit. on p. 73).

[120] Bela Bauer, Dave Wecker, Andrew J. Millis, Matthew B. Hastings, and M. Troyer. *Hybrid quantum-classical approach to correlated materials*. 2015. URL: `https://arxiv.org/abs/1510.03859` (cit. on p. 73).

[121] Jayne Thompson, Mile Gu, Kavan Modi, and Vlatko Vedral. *Quantum Computing with black-box Subroutines*. 2013. URL: `http://arxiv.org/abs/1310.2927` (cit. on p. 73).

[122] Michael Kaicher, Felix Motzoi, and Frank K. Wilhelm. "Pauli strings with the exchange interaction." 2016 (cit. on pp. 75, 78, 81).

[123] David Poulin, M. B. Hastings, Dave Wecker, Nathan Wiebe, Andrew C. Doherty, and Matthias Troyer. "The Trotter Step Size Required for Accurate Quantum Simulation of Quantum Chemistry." In: *QIC* 15 (2015), p. 361. URL: `http://arxiv.org/abs/1406.4920` (cit. on pp. 75, 89).

[124] Per Liebermann, Pierre-Luc Dallaire-Demers, Elie Assémat, and Frank K. Wilhelm. "Conditional imaginary swap gates for quantum simulation of fermions." 2016 (cit. on p. 82).

[125] Naomichi Hatano and Masuo Suzuki. "Finding Exponential Product Formulas of Higher Orders." In: *Quantum Annealing and Other Optimization Methods*. Vol. 679. Lecture Notes in Physics. Springer Science Business Media, Nov. 2005, pp. 37–68. DOI: `10.1007/11526216_2` (cit. on pp. 89, 90).

[126] R. D. Ruth. "A canonical integration technique." In: *IEEE Transactions on Nuclear Science* 30 (1983), p. 2669 (cit. on p. 90).

[127] Michele Benzi, Gene H. Golub, and Jörg Liesen. "Numerical solution of saddle point problems." In: *Acta Numerica* 14 (May 2005), pp. 1–137. DOI: `10.1017/s0962492904000212` (cit. on p. 99).

COLOPHON

This document was typeset using the typographical look-and-feel `classicthesis` developed by André Miede. The style was inspired by Robert Bringhurst's seminal book on typography *"The Elements of Typographic Style"*. `classicthesis` is available for both LaTeX and LyX:

`http://code.google.com/p/classicthesis/`

Final Version as of October 10, 2016 (`classicthesis` version 4.0).

DECLARATION OF ORIGINAL AUTHORSHIP

I hereby declare that this dissertation is my own original work except where otherwise indicated. All data or concepts drawn directly or indirectly from other sources have been correctly acknowledged. This dissertation has not been submitted in its present or similar form to any other academic institution either in Germany or abroad for the award of any other degree.

Saarbrücken, 2016

Pierre-Luc Dallaire-Demers